

Dudley

NASA CR-166136

(NASA-CR-16-136) AN INVESTIGATION OF ENGINE
INFLUENCE ON INLET PERFORMANCE (Boeing
Commercial Airplane Co., Seattle) 88 p
HC A05/ME 001 3502 01a

881-30984

Unclass
3-208

63/02

An Investigation of Engine Influence On Inlet Performance

B. K. Hodder

**Boeing Commercial Airplane Company
Seattle, Washington 98124**

**Prepared for
NASA-Ames Research Center
under Cooperative Agreement**

NASA

National Aeronautics and
Space Administration

1981

CONTENTS

	Page
SUMMARY	1
INTRODUCTION	3
APPROACH	5
SYMBOLS	7
MODELS AND APPARATUS.....	9
INSTRUMENTATION AND TEST PROCEDURES	10
RESULTS AND DISCUSSION	13
CONCLUSIONS	22
REFERENCES	23

FIGURES

No.	Page
1. Definition of Inlet/Engine Flow Field Interaction (Using Windmill Analogy)	25
2. Redistribution of Distorted Inlet Flow Velocity Caused by a Rotor (2-D Calculation From Ref. 2)	25
3. Inlet Coordinates	26
4. Front View of Inlet Configuration For the Close-Coupled Inlet Installation	28
5. Conceptual Inlet System With and Without Inlet/Engine Interaction	29
6. Aft View of Inlet Configuration For the Remote-Coupled Inlet Installation Showing the Spinner Afterbody Fairing	30
7. Close-Coupled Engine/Inlet Installation Mounted in the NASA-Ames 40-by-80-Foot Wind Tunnel	31
8. Remote-Coupled Engine/Inlet Installation Mounted in the NASA-Ames 40-by-80-Foot Wind Tunnel	33
9. Fan Face Instrumentation	35
10. Fan Face Boundary Layer Rake	36
11. Inlet Internal Surface Instrumentation	37
12. Compressor Inlet Instrumentation	38
13. Fan Nozzle Exit Instrumentation	39
14. TF-34 Operating Line Characteristics	40
15. Inlet Airflow Versus Fan Nozzle Pressure Ratio; Ames TF-34	40
16. Variation of Inlet Boundary Layer Total Pressure Profile With Inlet Angle-of-Attack; Without Engine Interaction $V_T = 171.7(318.0)$, $\theta = 175^\circ$, WKIA = 36.10(176.23)	41
17. Variation of Inlet Internal Mach Number Distribution With Inlet Angle-of-Attack; Without Engine Interaction, $V_T = 171.7(318.0)$, $\theta = 180^\circ$, WKIA = 36.10(176.23)	41
18. Comparison of Inlet Total Pressure Profiles Measured by the Boundary Layer Rake and the Recovery Rake With the Inlet Separated; Without Engine Interaction, $V_T = 171.7(318.0)$, WKIA = 36.10(176.23), $\alpha = 28^\circ$	42
19. Variation of Steady-State Inlet Boundary Total Pressure Profiles and RMS Total Pressure Levels With Angle-of-Attack; Without Engine Interaction $V_T = 171.7(318.0)$, WKIA = 36.10(176.23)	43
20. Variation of Inlet Boundary Layer Total Pressure Profile With Inlet Angle-of-Attack; Without Engine Interaction, $V_T = 147.7(273.5)$, $\theta = 175^\circ$, WKIA = 32.06(156.5)	44
21. Variation of Inlet Internal Mach Number Distribution With Inlet Angle-of-Attack; Without Engine Interaction, $V_T = 147.7(273.5)$, $\theta = 180^\circ$, WKIA = 32.06(156.50)	44
22. Comparison of Inlet Total Pressure Profiles Measured by the Boundary Layer Rake and the Recovery Rake With the Inlet Separated; Without Engine Interaction, $V_T = 147.7(273.5)$, WKIA = 32.06(156.50), $\alpha = 32^\circ$	45

FIGURES (CONTINUED)

No.	Page
23	Variation of Steady-State Inlet Boundary Layer Total Pressure Profiles and RMS Total Pressure Levels With Angle-of-Attack; Without Engine Interaction, $V_T = 147.7(273.5)$, $WKIA = 32.06(156.50)$ 46
24	Variation of Inlet Boundary Layer Total Pressure Profiles With Inlet Angle-of-Attack; With Engine Interaction, $V_T = 171.4(317.4)$, $\theta = 175^\circ$, $WKIA = 36.05(175.98)$ 47
25	Variation of Steady-State Inlet Boundary Layer Total Pressure Profiles and RMS Total Pressure Levels With Angle-of-Attack; With Engine Interaction, $V_T = 171.4(317.4)$, $WKIA = 36.05(175.98)$ 48
26	Comparison of Dynamic Total Pressure Time Histories Measured by the Recovery Rake With and Without Engine Interaction, $\theta = 185^\circ$, Probe Radius = 19.16 in. (48.67 cm) 49
27	Variation of Inlet Internal Mach Number Distribution With Inlet Angle-of-Attack; With Engine Interaction, $V_T = 171.4(317.4)$, $\theta = 180^\circ$, $WKIA = 36.05(175.98)$ 50
28	Variation of Inlet Internal Mach Number Distribution With Inlet Angle-of-Attack; With Engine Interaction, $V_T = 171.7(317.4)$, $\theta = 180^\circ$, $WKIA = 36.05(175.98)$ 50
29	Comparison of Dynamic Total and Static Pressure Time Histories From the Inlet Recovery Rake and the Inlet Internal Wall ($\theta = 180^\circ$); With Engine Interaction, $V_T = 171.4(317.4)$, $WKIA = 36.05(175.98)$, $\alpha = 32^\circ$ 51
30	Comparison of Inlet Total Pressure Profiles Measured by the Boundary Layer Rake and the Recovery Rake With the Inlet Separated; With Engine Interaction, $V_T = 171.4(317.4)$, $WKIA = 36.05(175.98)$ 52
31	Variation of Inlet Boundary Layer Total Pressure Profile With Inlet Angle-of-Attack; With Engine Interaction, $V_T = 147.4(273.5)$, $\theta = 175^\circ$, $WKIA = 36.05(175.98)$ 53
32	Comparison of Dynamic Total and Static Pressure Time Histories From the Inlet Recovery Rake and the Inlet Internal Wall ($\theta = 180^\circ$); With Engine Interaction, $V_T = 174.4(273.5)$, $WKIA = 36.05(175.98)$, $\alpha = 35^\circ$ 54
33	Variation of Inlet Internal Mach Number Distribution With Inlet Angle-of-Attack; With Engine Interaction, $V_T = 174.4(273.5)$, $\theta = 180^\circ$, $WKIA = 36.05(175.98)$ 55
34	Variation of Inlet Boundary Layer Total Pressure Profile With Inlet Angle-of-Attack; With Engine Interaction, $V_T = 147.2(273.5)$, $\theta = 175^\circ$, $WKIA = 32.11(156.75)$ 55
35	Variation of Inlet Internal Mach Number Distribution With Inlet Angle-of-Attack; With Engine Interaction, $V_T = 147.2(273.5)$, $\theta = 180^\circ$, $WKIA = 32.11(156.75)$ 56
36	Variation of Inlet Boundary Layer Total Pressure Profile With Inlet Angle-of-Attack; With Engine Interaction, $V_T = 186.0(344.5)$, $\theta = 175^\circ$, $WKIA = 32.15(156.94)$ 56

FIGURES (CONTINUED)

No.	Page
37	Variation of Inlet Internal Mach Number Distribution With Inlet Angle-of-Attack; With Engine Interaction $V_T = 186.0(344.5)$, $\theta = 180^\circ$, WKIA = 32.15(156.94) 57
38	Comparison of Dynamic Total and Static Pressure Time Histories From the Inlet Recovery Rake and the Inlet Internal Wall ($\theta = 180^\circ$); With Engine Interaction, $V_T = 186.2(344.8)$, WKIA = 32.04(156.41), $\alpha = 27.5^\circ$ 58
39	Variation of Internal Mach Number Distribution With Inlet Angle-of-Attack; With Engine Interaction, $V_T = 186.2(344.8)$, $\theta = 180^\circ$, WKIA = 32.04(156.41) 59
40	Comparison of Inlet Total Pressure Profiles Measured by the Boundary Layer Rake and the Recovery Rake With the Inlet Separated; With Engine Interaction, $V_T = 186.2(344.8)$, WKIA = 32.04(156.41), $\alpha = 27.5^\circ$ 59
41	Comparison of Dynamic Total and Static Pressure Time Histories From the Inlet Recovery Rake and the Inlet Internal Wall ($\theta = 180^\circ$); With Engine Interaction, $V_T = 171.5(317.6)$, WKIA = 22.26(108.66), $\alpha = 27^\circ$ 60
42	Variation of Internal Mach Number Distribution With Inlet Angle-of-Attack With Engine Interaction, $V_T = 171.5(317.6)$, $\theta = 180^\circ$, WKIA = 22.26(108.66) 61
43	Comparison of Inlet Total Pressure Profiles Measured by the Boundary Layer Rake and the Recovery Rake With the Inlet Separated; With Engine Interaction, $V_T = 171.5(317.6)$, WKIA = 22.26(108.66), $\alpha = 27^\circ$ 61
44	Comparison of the Axial Location of Boundary Layer Separation With and Without Engine Interaction Determined From Cowl Mach Number Distributions, $\theta = 180^\circ$ 62
45	Comparison of the Axial Location of Boundary Layer Separation With and Without Engine Interaction Determined From Cowl Mach Number Distribution, $\theta = 180^\circ$ 63
46	Comparison of Inlet Separation Boundaries With and Without Engine Interaction 64
47	Comparison of Inlet Internal Static Pressure Distribution With and Without Engine Interaction, $\alpha = 25^\circ$ 65
48	Comparison of Fan Face Total Pressure Recovery Maps With and Without Engine Interaction 66
49	Comparison of Fan Face Total Pressure Recovery Maps With and Without Engine Interaction 67
50	Comparison of Fan Face Total Pressure Recovery Maps With and Without Engine Interaction 68
51	Comparison of Fan Face Total Pressure Recovery Maps With and Without Engine Interaction 69
52	Comparison of Fan Face Total Pressure Recovery Maps With and Without Engine Interaction 70

FIGURES (CONCLUDED)

No.		Page
53	Comparison of Fan Face Total Pressure Recovery Maps With and Without Engine Interaction	71
54	Variation of Inlet Distortion With Inlet Angle-of-Attack; With and Without Engine Interaction, $V_T = 171.6(317.8)$, $WKIA = 36.07(176.06)$	72
55	Variation of Inlet Distortion With Inlet Angle-of-Attack; With and Without Engine Interaction, $V_T = 147.6(273.4)$, $WKIA = 36.06(176.05)$	74
56	Variation of Inlet Distortion With Inlet Angle-of-Attack; With and Without Engine Interaction, $V_T = 186.8(346.0)$, $WKIA = 36.04(175.93)$	76
57	Variation of Inlet Distortion With Inlet Angle-of-Attack; With and Without Engine Interaction, $V_T = 186.2(344.9)$, $WKIA = 32.16(156.99)$	78
58	Variation of Inlet Distortion With Inlet Angle-of-Attack; With and Without Engine Interaction, $V_T = 171.5(317.6)$, $WKIA = 22.25(108.59)$	80

SUMMARY

Accurately predicting engine inlet steady-state distortion levels at conditions that produce separated inlet flows (crosswinds and high angles-of-attack) is a continuing problem associated with the use of conventional small-scale inlet test techniques. Based on existing evidence, part of the problem may be that small-scale test techniques generally do not simulate the influence of the engine on the inlet flow field. It has long been recognized that an axial flow compressor can attenuate artificially induced upstream flow distortion. But not enough fundamental understanding of this interaction exists for the case of an inlet/engine system where the source of the upstream distortion results from lack of inlet flow uniformity which in turn reacts to the favorable influence of the engine. An investigation was conducted to better understand the significance of engine/inlet interaction on inlet distortion levels resulting from separated inlet flows.

The results from a large-scale inlet test in the NASA-Ames 40- by 80-foot low-speed Wind Tunnel are discussed. Inlet performance at angle-of-attack was measured with the inlet coupled to the engine in the normal manner, as well as, in a remote-coupled configuration which decoupled the influence of the engine on the inlet flow field. The latter configuration simulated current small-scale test techniques in which inlet airflow is provided by a vacuum system or remote-coupled engine. Measured data from both inlet configurations provide comparisons of inlet boundary-layer profiles, fan-face total-pressure recovery maps, inlet surface Mach number distributions, and inlet distortion levels. Test results indicated that engine interaction allows the inlet to operate with lower distortion levels at and beyond the separation angle-of-attack experienced without engine interaction.

INTRODUCTION

The use of viscous analytical codes to design subsonic engine inlets has gained reasonable maturity and established itself as a valuable engineering tool. However, verification of inlet flow separation boundaries and accompanying pressure recovery and distortion levels still must be obtained from experimental tests. Historically, the high cost of providing and operating test facilities has forced the majority of experimental inlet tests to be conducted with small-scale inlet models (1/6 scale or smaller) which provide no simulation of flow effects caused by the presence of the engine in the actual full-scale inlet.

Experience with separated inlet flows has shown that small-scale inlets without engine simulation have poorer performance than installed full-scale inlets. Factors thought to contribute to improved installed inlet performance have been both a higher inlet Reynolds number and engine/inlet flow field interaction. But the relative contribution of each has remained unclear.

Because the conservatism of small-scale performance has been generally accepted, arguments for improving small-scale prediction methods are much less persuasive than if the situation were reversed and installed performance was below small-scale prediction. The potential fallacy of remaining with the status quo is that the conservatism of current small-scale inlet test techniques may be unnecessarily penalizing the inlet design in terms of weight and drag.

The resolution of this dilemma is linked to expanding the data base detailing engine/inlet flow field interaction and Reynolds number effects. It was the intent of the present investigation to develop a better understanding of engine/inlet flow field interaction.

PRECEDING PAGE BLANK NOT FILMED

APPROACH

It may be helpful in describing the approach developed for this investigation to review first some background information relative to engine influence on the inlet flow field. Technical reports dealing with the fundamentals of how an engine generates an influence on the inlet flow field are somewhat deceptive in that they are invariably entitled and written to focus on the response of an engine stage or stages to an inlet distortion. Although it is implied that the distortion resulted from poor inlet performance, little if any discussion occurs as to whether inlet performance would be different if the engine were not present and the inlet flow instead was induced by a remote source (vacuum pump or remote-coupled engine).

Discussion of how an axial flow compressor stage alters an upstream non-uniform velocity profile seems to have its beginnings in literature published in the late 1950's (ref. 1, 2) and is often referred to as parallel compressor theory. In these analyses, it was found that an axial flow device will, in effect, attenuate the incoming distortion by redistributing the inlet flow. It is this redistribution of the inlet flow field ahead of the initial compressor stage that is important to inlet performance.

It seems helpful to explain why the compressor rotor creates this redistribution of flow by making an analogy with a rotor which does no work (i.e., a windmill). Consider initially a freely rotating rotor placed in a duct in which there is a uniform flow with velocity V_A (figure 1). Since the rotor can produce no net thrust or torque, the inlet velocity triangle composed of the axial inflow velocity V_A and the rotor tangential velocity V_t must combine to create a blade angle-of-attack of zero lift. Now, suppose that a steady-state disturbance is placed in the flow upstream of the rotor which creates a local total pressure deficit. If we assume initially that the total pressure deficit is reflected in a reduced axial inflow velocity V'_A , the local rotor inlet velocity triangle will change (figure 1) and result in a local blade angle-of-attack not equal to the blade angle-of-attack of zero lift. Accordingly, a thrust and torque will occur on the rotor locally in the region affected by the velocity deficit. However, since the windmill can produce no net thrust or torque in a steady-state sense, this response to the velocity deficit must be transitory and simply means that the rotor must create a new operating condition. To accomplish this, the rotor causes the duct velocity vectors to readjust in both magnitude and orientation around the entire rotor disc (both inside and outside the velocity deficit region) so that again no net thrust or torque on the rotor is produced. In effect, the higher energy regions are forced to give up energy to the lower energy regions. An example of such an interchange in terms of duct axial velocity is shown in figure 2 taken from reference 2. Accompanying variations in duct static pressure also occur. By contrast, should the fan rotor not be present in the duct, the high and low total pressure regions would pass down the duct unchanged with velocity proportional to the total pressure distribution and uniform static pressure distribution.

The windmill is analogous to a thrust producing rotor in that both strive to maintain their operating characteristics when confronted with a non-uniform inlet flow. The thrust producing rotor causes a redistribution of the approaching flow to maintain a constant discharge static pressure. The rotor can generate this flow redistribution as long as the flow non-uniformity is not severe enough to cause the rotor blade to stall.

Analyses which predict the influence of the rotor on a non-uniform upstream flow field can also provide information for designing an inlet/engine combination which will allow examination of inlet performance with and without engine interaction. The resultant configurations can be termed a close-coupled engine/inlet and a remote-coupled engine/inlet. The close-coupled engine inlet is a conventional engine/inlet installation in which engine interaction is present. In the remote-coupled case, engine interaction with the inlet flow field is decoupled by connecting the inlet to the engine with a long intervening duct. The same engine used in the close-coupled inlet now becomes, in the remote-coupled inlet, simply a means to provide airflow through the inlet. Analysis in reference 3 indicated that rotor interaction was negligible beyond three rotor tip radii upstream of the rotor thus this dimension provides the minimum length for a spacer duct between the engine and inlet in a remote-coupled configuration.

The preferred test program would have used a full-scale configuration so that the significance of engine influence on inlet performance could be isolated (i.e., no simultaneous inlet or rotor Reynolds number effects mixed into the results). In pursuit of a test engine and test facility to conduct the test, difficulties were encountered in locating an adequate test facility to test full-scale turbofan engines of the JT9D, CF6, and RB-211 class. A compromise position was determined which utilized a test engine approximately one-half scale relative to JT9D, CF6, RB211 engines but of similar aerodynamic design. The appropriate test facility was the NASA-Ames 40 ft x 80 ft low-speed Wind Tunnel. It was assumed that a one-half scale inlet test represented a sufficient scaling step from conventional small-scale models to allow measured engine interaction effects to be interpreted as representative of full-scale results.

SYMBOLS

α or alpha	Inlet angle-of-attack referenced to the inlet axis, deg.
CKN2	Corrected fan rotor speed, $\frac{\text{rev}}{\text{min}}$
CP	Static pressure coefficient
FNPR	Fan nozzle total pressure ratio
IDCHUB	Hub circumferential distortion index; IDCHUB = Max. of $(IDC_1 + IDC_2)/2$ or $(IDC_2 + IDC_3)/2$
IDCTIP	Tip circumferential distortion index; IDCTIP = Max. of $(IDC_3 + IDC_4)/2$ or $(IDC_4 + IDC_5)/2$
IDC_j	$K1 \left[(PTR_{AVG})_j - (PTR_{MIN})_j \right] / (PTR_{AVG})_{FACE}$
IDRTIP	Tip radial distortion index; IDRTIP = $IDR_5 + K2 IDR_4$
IDR_j	$\left[(PTR_{AVG})_{FACE} - (PTR_{AVG})_j \right] / (PTR_{AVG})_{FACE}$
K1	Weighting coefficient - function of the size of the annular region which is below the ring average and the number of low pressure regions per ring
K2	Weighting coefficient - function of the radial extent of the low pressure region
PSBL	Boundary-layer static pressure at wall, $\frac{\text{lb}}{\text{in}^2} (\text{Kg/cm}^2)$
PSBL/PTREF	Boundary-layer wall static to freestream total-pressure ratio
PTBL	Boundary-layer total pressure, $\frac{\text{lb}}{\text{in}^2} (\text{Kg/cm}^2)$
PTBL/PTREF	Boundary-layer total pressure ratio
PTR	Recovery rake total pressure, $\frac{\text{lb}}{\text{in}^2} (\text{Kg/cm}^2)$
PTREF	Freestream total pressure, $\frac{\text{lb}}{\text{in}^2} (\text{Kg/cm}^2)$

(SYMBOLS (CONTINUED))

PTTRAV	Traversing wedge probe total pressure, $\frac{1b}{in} 2(Kg/cm^2)$
R	Radius, in (cm)
θ or theta	Inlet circumferential position, deg
WKI	Corrected inlet airflow, $\frac{1b}{sec} \left(\frac{Kg}{sec} \right)$
WKIA	Corrected inlet airflow divided by the fan annulus area at the fan rotor blade leading edge plane $\frac{1b}{sec-ft^2} \left(\frac{Kg}{sec-m^2} \right)$
X	Axial distance, in (cm)
Y	Vertical distance, in (cm)
V	Velocity, knots $\left(\frac{km}{h} \right)$

SUBSCRIPTS

AVG	Average
EXT	External
FACE	Fan face; includes all "j" rings
i	Inlet
INT	Internal
j	Index for each of 5 equal area annular rings located in the plane of the total pressure recovery rake measurements
SEP	Separation
T	Wind Tunnel
t	Tangential

MODEL AND APPARATUS

A government-supplied General Electric WTF-34-F5 turbofan engine was used as the test engine for this investigation. The TF-34 incorporates a single-stage fan with a design pressure ratio of 1.5:1 and a bypass ratio of 6.23. The fan diameter is 44 inches (1.118 m). The engine was operated with the manufacturer's reference calibration nozzles on both the fan and primary exhausts.

The inlet design is typical of designs used in current subsonic commercial transports. The inlet had an L/D of .57 and an asymmetric lip section with a contraction ratio of 1.24 on the crown ($\theta = 0^\circ$) varying to 1.28 on the keel ($\theta = 180^\circ$). The inlet centerline was canted 5° down (droop) relative to the engine centerline. The scale of the inlet, determined by the engine attach-flange diameter, was .47 relative to a full-scale inlet of a JT9D, CF6 or RB211 class engine. A table of coordinates for the inlet is presented in figure 3.

Construction of the inlet provided for integral mounting of a fan-face total pressure recovery rake to the inlet outer wall. The opposite end of each rake arm was joined by a common structural ring which supported a dummy non-rotating engine spinner built to the same lines as the actual engine spinner. In the close-coupled inlet configuration (figure 4), the actual engine spinner was removed and the non-rotating spinner, attached to the fan-face total pressure recovery rake, was substituted.

Final design of the remote-coupled inlet configuration used an engine/inlet spacer duct 4.8 rotor tip radii long to assure that the inlet flow field was sufficiently decoupled from engine influence (figure 5). The spacer duct had a constant internal diameter of 44 inches (1.118 m) which matched the internal diameter of the fan case at the engine/inlet attach flange. In the remote-coupled configuration, the normal engine spinner was reinstalled on the engine and a 3:1 elliptical fairing (figure 6) was added to the aft end of the spinner/fan face total pressure recovery rake assembly to fair out the body. The upstream end of the 3:1 elliptical fairing also contained a short section whose contour was designed as a transition section to turn the local flow from the spinner contour to the elliptical afterbody contour without excessive peak mach numbers.

The inlet configuration forward of the engine/inlet attach flange remained identical regardless of which inlet configuration (close-coupled or remote-coupled) was installed, i.e., same instrumentation, fan face total pressure recovery rake, and engine spinner.

Both inlet models were supported from overhead and slung between the wind tunnel main support struts on a cross beam assembly (figures 7, 8). Variation of inlet angle-of-attack was accomplished by extending or retracting the wind tunnel tail strut which was linked to the model cross beam assembly. Mechanical limits of the wind tunnel pitch system allowed a maximum inlet angle-of-attack of $+35^\circ$.

INSTRUMENTATION AND TEST PROCEDURES

The test instrumentation consisted of 242 steady-state measurements, comprised of 208 pressures, 34 total temperatures, and wind tunnel and engine operating parameters. Thirteen dynamic pressures were also measured. Instrumentation for each measurement task is described in the following paragraphs.

The inlet contained an eight-arm total pressure recovery rake (figure 9) with each rake arm containing ten equal area-weighted elements and an associated spinner and cowl wall static pressure. As discussed in the Model and Apparatus section, the recovery rake assembly remained in the same position relative to the inlet in both the close-coupled and remote-coupled configurations. The actual total pressure measurement plane of the recovery rake assembly was approximately 6 in. (15.24 cm) forward of the fan rotor to allow for the structural components of the rake. While this measurement distance is quite representative of engine/pressure rake installations it caused some concern in relation to the objectives of this investigation in that separated flows with engine interaction might reattach aft of the recovery rake. This would cause the rake measurement to be unrepresentative of the flow presented to the fan. Also, this more forward position might eliminate the ability to detect inlet diffuser boundary layer separation which tends to start near the fan face and progress forward. To help compensate for these potential measurement problems, two total pressure boundary layer rakes were added, both of which are shown schematically in figure 9. At $\theta = 175^\circ$, a 3 in. (7.62 cm) boundary layer rake (see figure 10) was mounted with the measurement plane approximately 2 in. (5.08 cm) forward of the rotor plane. Measurements with this rake would help identify boundary layer separation much closer to the fan rotor plane and were monitored with on-line data plotting. To provide boundary layer information for the more extreme case where engine interaction might cause separated flow reattachment very close to the fan rotor, a 3/16-inch diameter wedge probe was installed at $\theta = 180^\circ$ and could be traversed radially .5 in. (1.27 cm) in front of the rotor plane. The wedge probe provided measurement of total pressure and flow yaw angle. The eight-arm total-pressure recovery rake was also equipped with three radially distributed dynamic total pressure probes at both $\theta = 185^\circ$ and 135° . The dynamic total pressure measurements near the outer duct wall were purposely positioned to be outside the boundary layer of attached inlet flows determined from analysis. Finally, three radially distributed total temperature probes were also mounted on the recovery rake at $\theta = 5^\circ$ and $\theta = 225^\circ$.

Inlet steady-state surface static pressure measurements were made at various circumferential and axial positions in the inlet as detailed in figure 11. Dynamic surface static pressure measurements were also made along the inlet keel ($\theta = 180^\circ$) from just forward of the inlet throat to near the engine attach flange.

Inlet total airflow was measured using a calibrated inlet technique developed in reference 4. The technique relies on the prior calibration of a smaller but geometrically similar inlet model in a wind tunnel where inlet airflow can be accurately measured with a venturi. Measured airflow is converted to an airflow coefficient and plotted versus a corresponding average inlet static pressure ratio measured near the inlet throat. This airflow calibration can be used to determine airflow in other geometrically similar inlets of different scale provided the appropriate static pressure ratio is measured in the inlet in question. In the present test,

four static pressures at inlet station $X_1 = 6.10$ in (15.49 cm) and $\theta = 0^\circ, 90^\circ, 180^\circ$ and 270° were used to form the above static pressure ratio and values were computed on-line and displayed to allow the engine operator to maintain the desired engine corrected airflow. Possible corrections to the small-scale (1/6 scale) inlet calibration for use with the .47 scale test inlet were examined analytically and found to be negligible.

Although this airflow calibration method tends to correlate data obtained at different angles of attack on a single curve, there is some influence of angle-of-attack remaining. To improve the calibration accuracy, two calibration curves were used; one curve for angles-of-attack less than $+20^\circ$ and a second curve for angles-of-attack equal to or greater than $+20^\circ$. Airflow measurement accuracy was estimated to be $\pm 2\%$.

The compressor inlet, figure 12, contained three total temperature rakes and three total pressure rakes. Each total temperature rake contained two equal area-weighted thermocouples and each total pressure rake contained four equal area-weighted total pressure probes with a Prandtl-type static probe on the innermost radius. There were also three wall statics on the duct outer wall near each total pressure rake.

The fan nozzle exit was instrumented with four total pressure and four total temperature rakes (figure 13). Each rake had five equal area-weighted elements. Each total pressure rake also had an associated inner and outer wall static pressure orifice.

Three engine parameters, the fan (N2) and compressor (N1), rotational speed, and turbine total temperature (TT5), were recorded on the data system. To protect the engine from excessive stress levels that might be encountered during inlet flow separation, stress levels were monitored (in the fan outlet guide vane assembly) at twelve different locations recommended by the engine manufacturer.

All instrumentation sensors associated with engine performance were mounted on the test model. Measured data were recorded, calibrated and calculated by a Hewlett-Packard 3052/9825 data system with output available on a line printer. Dynamic data were FM-tape recorded with a frequency response of 1.5Hz to 5 KHz.

The engine operating points for this investigation were somewhat below the maximum obtainable due to the higher than anticipated wind tunnel freestream temperatures and the "engine-on condition" time limits specified by the engine manufacturer. Wind tunnel freestream temperatures are somewhat difficult to maintain at desirable levels because the 40 by 80-foot Wind Tunnel is a closed circuit design which causes engine hot exhaust gases to be recirculated. The "on condition" time limits for the engine at some of the higher operating points, were too short compared to the time required to pitch the model through a meaningful angle-of-attack range. It was finally determined that $WKIA = 36$ (175.5) was the highest inlet airflow/unit area that could be run and be compatible with the previous limitations. For comparison, the engine design point corresponds to $WKIA = 40.2$ (196).

A calibration of the test engine was made prior to the actual wind tunnel test to retrim the engine which had been inactive for some time. This calibration was made with the manufacturer's recommended inlet bellmouth and reference nozzle hardware. The Ames test engine operating line performance, in terms of inlet airflow versus fan speed, compared to that of a

standard TF-34, figure 14, showed good agreement.

Disagreements on the order of 2% in measured inlet airflow for a given fan speed were found between the manufacturers' method and the method used in this report. The error was within the error band indicated for each method and is not uncommon when different techniques involving different inlets are involved. Inlet airflow measured by the method of this report is plotted versus measured fan nozzle total pressure in figure 15 for reference.

RESULTS AND DISCUSSION

OVERVIEW

Based on the principles of parallel compressor theory one would anticipate the major influence of the engine to occur just prior to or during flow separation. Angle-of-attack polars with inlet airflow and airspeed held constant were run to induce inlet boundary-layer separation for both inlet configurations. The method of determining inlet boundary-layer separation was based on measurements from the 3 in. (7.62 cm) boundary-layer rake and application of criteria for classical two-dimensional boundary-layer separation. Separation was assumed to have occurred if the boundary-layer total-pressure profile approached the duct wall with essentially zero slope and the total pressure in this region was near or below the neighboring wall static pressure; thus indicating very little local flow velocity or reverse flow respectively.

Test program results are discussed in the following sequence. First, the characteristics of inlet boundary-layer separation with and without engine interaction are reviewed in detail for some representative test conditions and then compared in general. Next, the impact that the respective separation characteristics have on the fan-face total-pressure recovery map and inlet distortion indices are reviewed. Finally, some conclusions are reached regarding the influence of engine interaction on inlet performance.

INLET SEPARATION CHARACTERISTICS WITHOUT ENGINE INTERACTION

Measured results can be presented more clearly by beginning the discussion with a review of the data obtained without engine interaction. Figure 16 presents a representative progression of inlet boundary-layer total-pressure profiles measured during an angle-of-attack polar. As angle-of-attack was increased the boundary-layer thickness increased and the profile incurred an inflexion point characteristic of instability in the boundary layer. Abruptly, at $\alpha = 28^\circ$ the total pressure profile shows a drastic change and one which satisfies the criteria for boundary-layer separation. At $\alpha = 28^\circ$ the total boundary-layer thickness exceeds the height of the boundary rake and the higher total-pressure recoveries near the edge of the boundary layer are not measurable with boundary-layer rake as will be shown in later figures.

The axial location of inlet flow separation was interpreted from plots of cowl surface Mach number versus inlet cowl station. Cowl surface Mach number was computed from cowl surface static pressures measured on the inlet keel (windward side). Figure 17 presents Mach number distributions from the same α polar that the boundary-layer data of figure 16 was obtained. A corresponding loss in inlet diffuser static pressure recovery (no decrease in diffuser Mach number) is seen to occur at the same angle-of-attack that boundary-layer separation was indicated. The axial location of boundary-layer separation is interpreted to be where the loss in diffuser recovery first appeared, or in this example, at about the 12% cowl station.

Based on the approximate location of inlet boundary-layer separation from figure 17, the total-pressure recovery rake is well downstream (at about the 76% cowl station) of the sepa-

ration point and should see approximately the same total-pressure recovery as the boundary-layer rake over the same radial distance. Total-pressure measurements from both the boundary-layer rake and the recovery rake, figure 18, show this to be true. Further, the recovery rake measurement confirms that inlet total pressure did recover to the freestream level at a radial position exceeding the height of the boundary-layer rake.

An additional correlation is made in figure 19 between the steady-state boundary-layer profiles of figure 16 and the corresponding rms dynamic total-pressure levels measured on recovery rake at $\theta = 185^\circ$. Notice, that when boundary-layer profile indicated flow separation, there was a large corresponding increase in the rms level of dynamic total pressure. Although this correlation is not unexpected, it will be useful to remember when reviewing results with engine interaction.

In figure 20 through 23, a similar series of plots, like those just discussed, are presented for a lower inlet airflow and airspeed. The results are similar; only the angle-of-attack and location of boundary-layer separation have changed as a result of the change in operating conditions.

In general, boundary-layer separation characteristics measured for all the test conditions run without engine interaction are well represented by the examples shown in the previous figures. Boundary-layer separation tended to be abrupt and occurred well forward in the inlet at positions between the 18% cowl station and the hilite for all conditions discussed in this report. A forewarning of this rather extensive separation was not detected in the form of a prior inlet diffuser separation. The only warning that separation was imminent occurred at an inlet airflow/unit area of $WKIA = 36$ (175.5) where large intermittent changes in dynamic pressure amplitude preceded lip separation by about $.5^\circ$. Because analytical calculations for this inlet repeatedly predicted an initial diffuser separation at the test conditions investigated, it is surmised that diffuser separation probably does occur but more as a time-dependent condition rather than a steady-state one preceding lip separation. Either that, or the separated region in the diffuser is confined to such a small region near the duct wall and a small angle-of-attack increment prior to lip separation that it could not be measured with the instrumentation and test procedures used here.

INLET SEPARATION CHARACTERISTICS WITH ENGINE INTERACTION

The measurement of inlet separation characteristics with engine interaction was attempted with the same approach used without engine interaction. However, inlet boundary-layer separation with engine interaction added another dimension to the measurement task caused by an intermittent or non-stationary characteristic. The likelihood of encountering a non-stationary flow separation was not unexpected; such behavior is often found in inlet tests without engine interaction but usually occurs briefly, and a stationary separation can be attained by increasing angle-of-attack about a $.5^\circ$ to 1° . In the present investigation, what was unexpected was the large angle-of-attack range over which non-stationarity persisted and the inability to pass through this region in numerous test runs before reaching mechanical stress limits in the fan outlet guide vane. Unfortunately, the test engine contained a hollow prototype fan outlet guide vane with lower stress limits than the production version which uses a solid vane design. The majority of the steady-state pressure measuring instrumentation provided for the test was not adequate to effectively measure some of the flow

conditions encountered. Accordingly, not every inlet separation condition can be properly presented. However, a number of test conditions can be reasonably analyzed using both the steady-state and dynamic measurements provided.

Figure 24 presents the progression of inlet boundary-layer total-pressure profiles measured during an angle-of-attack polar with engine interaction. The test condition, in terms of inlet airflow and airspeed, is comparable to that of figure 16 without engine interaction. The boundary-layer profiles for both inlet configurations are quite similar at $\alpha = 0^\circ$ and $\alpha = 25^\circ$ with the exception of slightly lower total pressure recovery near the duct wall with engine interaction. Beginning at $\alpha = 30^\circ$, figure 24, the total pressure levels near the inlet wall are below the level of the neighboring wall surface static pressure. Combining this fact with the shape of the total pressure profile near the wall implies that boundary-layer separation has occurred. This region near the inlet wall persists as angle-of-attack increases but, in addition, the profile as a whole acquires larger and larger irregularities. The source of these irregularities was traced to the existence of a non-stationary flow condition being sampled by a measurement system requiring stationary conditions. Evidence supporting this conclusion is presented in figures 25 and 26. The rms amplitude of dynamic total pressures measured on the $\theta = 185^\circ$ arm of the recovery rake is plotted versus angle-of-attack in figure 25. As shown previously, without engine interaction, a significant increase in rms dynamic pressure amplitude can be correlated with inlet boundary-layer separation. In figure 25, an abrupt increase in rms pressure level occurs at the same angle-of-attack that irregularities in the boundary-layer profiles become most pronounced. Further, a comparison of peak to peak dynamic total pressure amplitude time histories, figure 26, provides the final proof. Without engine interaction, time histories with the inlet flow separated, $\alpha = 28^\circ$, show an amplitude characteristic reasonably consistent with time. In contrast, the corresponding time history with engine interaction at $\alpha = 32^\circ$ shows intermittent periods of large pressure amplitude changes indicative of a non-stationary flow. The periods of increased pressure amplitude are basically indicators of accompanying flow conditions which apparently caused stress limits to be reached in the fan outlet guide vane. Upon reaching these stress limits, the angle-of-attack polar was terminated which eliminated the opportunity to possibly reach a stationary separated flow condition at higher angles-of-attack. Having established the cause for a somewhat transient behavior in a portion of the steady-state boundary-layer total-pressure profiles, it is useful to return to this data (figure 24) and examine more closely what appears to be happening. Boundary-layer separation was first indicated at $\alpha = 30^\circ$. Additional evidence that separation had occurred, as well as an indication of the axial location of separation can be interpreted from the corresponding surface Mach number distribution, figure 27. Inlet diffuser pressure recovery is also reduced starting at $\alpha = 30^\circ$. A repeat run, figure 28, shows this trend even more clearly due to measurements at smaller angle-of-attack increments prior to $\alpha = 30^\circ$. Also from these figures, the axial location of boundary-layer separation is indicated to be in the diffuser at about the 45% cowl station. No change in this location is seen as angle-of-attack is increased to $\alpha = 31^\circ$.

The steady-state data at $\alpha = 32^\circ$ shows irregularities caused by the non-stationary flow and is not useful for accurately determining the axial location of flow separation. However, the dynamic surface static pressure measurements made in this same region can provide insight as to the flow separation process. Figure 29 compares the time histories from all the keel ($\theta = 180^\circ$) dynamic surface static pressures and a corresponding time history from one of the dynamic total-pressure probes on the recovery rake at $\theta = 185^\circ$. Note that the ampli-

tude behavior with time correlates for all measurements and indicates that flow separation during the larger amplitude periods occurs on the inlet lip at least as far forward as the forwardmost dynamic transducer location. If the point of flow separation had remained at approximately the 45% cowl station, as was the case at $\alpha = 30^\circ$ and 31° , the amplitude versus time characteristic of the dynamic measurements made forward of that point (i.e., cowl stations 40.15%, 31.73% and 23.33%) should be different from those measurements aft of 45% cowl station.

Considering the information obtained from both the steady-state and dynamic measurements, it seems possible to conclude the following. Inlet separation for this test condition is characterized initially by a quasi-steady state diffuser separation and as angle-of-attack is increased, diffuser separation develops into a non-stationary separation intermittently moving from diffuser to lip and back again.

Finally, knowing that the axial location of diffuser separation at $\alpha = 30^\circ$ and 31° was forward of the recovery rake, a comparison of the total pressure recovery measured by the boundary-layer rake and the recovery rake is of interest. The data, figure 30, are in reasonable agreement.

A similar sequence of data plots for another airspeed but the same inlet airflow is presented starting with figure 31. At $\alpha = 35^\circ$ the slope of the boundary-layer total-pressure profile near the wall and the relative level of local total and wall static pressure indicate boundary-layer separation. The overall boundary-layer profile at $\alpha = 35^\circ$ has some small irregularities, but the corresponding dynamic pressure time histories (figure 32) show no large time-dependent pressure amplitude variations. These small irregularities and similar ones in figure 24, $\alpha = 30^\circ$, may be the result of unsteady three-dimensional flow effects in the separated region or small amounts of movement in the point of separation.

Cowl Mach number distributions, figure 33, also indicate separation at $\alpha = 35^\circ$ and the axial location of separation to be at about the 45% cowl station. Investigation of inlet separation characteristics beyond $\alpha = 35^\circ$ was impossible as $\alpha = 35^\circ$ was the mechanical limit of the wind tunnel/model installation.

Somewhat similar results were found at lower inlet airflows over the same airspeed range. An abbreviated series of boundary layer, cowl Mach number and dynamic time history plots are presented in figures 34 to 45 for review of the main characteristics of interest.

At inlet airflows corresponding to $WKIA = 32$ (156), a quasi-steady-state boundary-layer separation was identified prior to the onset of intermittent separation as shown in figure 34 for $\alpha = 30^\circ$ and in figure 36 for $\alpha = 26.5^\circ$. However, the corresponding cowl Mach number distributions, figures 35 and 37 did not indicate separation. Because data repeatability in general was very good, it is thought that this result is valid. What it may indicate, is that the axial location of diffuser separation moved very close to the end of the inlet. This would make any identification of the separated region impossible given the distribution of the cowl wall static pressure orifices. But since the boundary-layer rake is located at the end of the inlet it can measure such an occurrence. A separation of this type would not be identifiable with the recovery rake, but it is of little consequence relative to inlet distortion because of the very small radial and circumferential region involved. More importantly, some test

conditions at WKIA = 32 (156) provided the first opportunity to pitch the inlet through the intermittent separation region without exceeding fan outlet guide vane stress limits and measure a more developed quasi-stationary boundary-layer separation. The repeat run of test conditions presented in figure 37 provided just enough additional stationarity at $\alpha = 27.5^\circ$, based on the dynamic pressure time history traces of figure 38, to allow a reasonable measurement. The corresponding cowl Mach number distribution, figure 39, indicated flow separation occurred at about the 24% cowl station, well forward of the recovery rake. The total-pressure recovery measured by the recovery rake ($\theta = 185^\circ$) and the boundary-layer rake are compared in figure 40.

Some of the measured data at WKIA = 22 (107.3) did not allow clear identification of diffuser separation from the boundary-layer rake because of an almost simultaneous onset of intermittent separation which distorted the boundary-layer profile. But, it was again possible at WKIA = 22 (107.3) to reach a quasi-stationary inlet separation beyond the intermittent region at several airspeeds. Representative data at $V_T = 172$ (318.5) and $\alpha = 27^\circ$ is shown in figures 41 through 43. The time history of dynamic pressure measurements is shown in figure 41. The corresponding cowl Mach number distribution, figure 42, indicated the axial location of boundary-layer separation to be at about the 24% cowl station; again well forward of the recovery rake. Total-pressure recovery measured by the recovery rake ($\theta = 185^\circ$) and the boundary-layer rake are presented in figure 43.

Some additional comments may be useful for interpreting the comparison of total-pressure recovery profiles measured by the boundary-layer rake and the recovery rake presented in figures 40 and 43. It seems probably that the more irregular profile measured by the boundary-layer rake reflects the longer scan time, about six times that of the recovery rake, to acquire data over the same radial depth of 3 in. (7.62 cm). Both measurements start at the same time and sequence at the same rate but while the boundary-layer rake has eighteen measurements to acquire, the recovery rake needs only three to four measurements to cover the same radial depth. Admittedly the resolution of the recovery rake is poorer, but when the flow condition is only quasi-stationary, the shorter scan time provides a more instantaneous picture and probably a smoother profile.

In general, boundary-layer separation characteristics with engine interaction can be described as beginning with a measurable quasi-steady-state inlet diffuser separation. Diffuser separation then developed into an intermittent or non-stationary diffuser/lip separation which persisted for several degrees of angle-of-attack. No flow reattachment close to the fan rotor was indicated from measurements with the traversing boundary-layer probe. As previously discussed, many but not all α polars had to be terminated before reaching a stationary separation condition because of reaching engine mechanical stress limits. In those cases where the inlet angle-of-attack could be increased until a quasi-stationary separation occurred, the axial location of boundary-layer separation remained aft of the comparable location without engine interaction by as much as 6% of inlet length at the same or higher angles-of-attack. Some representative comparisons are shown in figures 44 and 45.

For a broader view of the inlet separation characteristics, inlet separation boundaries (that angle-of-attack at which boundary-layer separation was first detected) for both inlet configurations are compared in figure 46 over a range of inlet airflows and airspeeds. Data with and without engine interaction are compared by plotting separation angle-of-attack versus

inlet airflow for a constant airspeed. In viewing the comparisons, it is important to remember the difference in the extent of flow separation associated with these boundaries. Without engine interaction, the separation boundary equates to an extensive stationary separation occurring far forward in the inlet. The corresponding boundary with engine interaction implies a rather small diffuser separation. Accordingly, the separated flow condition without engine interaction creates a larger loss in inlet airflow after separation occurs. This difference in resultant inlet airflow can cause a misleading bias in the comparison. In actuality, the separation boundary for both inlet configurations was approached with essentially the same inlet airflow. Therefore, in figure 46, separation angle-of-attack is plotted versus the inlet airflow measured just prior to flow separation rather than the resultant airflow after separation occurred.

In general, the data show the differences in separation boundaries to be relatively small; in the neighborhood of 2° or less but with some exceptions. Neither inlet configuration consistently maintained a higher separation angle-of-attack than the other over the range of test conditions investigated. It seems appropriate to view this isolated comparison with less emphasis than one would a comparison of separation boundaries for two similar inlets (both either remote-coupled or close-coupled) and unconsciously equate separation boundaries with similar flow separation characteristics. The separation boundaries with engine interaction merely denote the onset of a complex process of separated flow development which, from a performance point of view, is more effectively evaluated by tracking comparative inlet distortion and total pressure recovery levels. These separation boundaries can, however, be quite useful for comparisons with analytical predictions which break down quite early in the development of flow separation.

Evidence that the variation in inlet separation boundaries was not contributed to by errors in mechanical angle-of-attack between the two inlet configurations can be found by comparing inlet surface static pressure distributions for equivalent test conditions. A representative comparison, figure 47, shows very little difference in inlet pressure coefficient at an angle-of-attack below separation.

FAN FACE TOTAL PRESSURE RECOVERY

Given the separation characteristics of both inlet configurations, the impact of the separated region on inlet total pressure recovery is compared with and without engine interaction in figures 48 to 53. In each comparison presented, the recovery data without engine interaction was measured at the angle-of-attack at which a stationary flow separation was first encountered, i.e., corresponds to the separation boundaries of figure 46. Total pressure recovery data with engine interaction for comparison is included at the same or higher angles-of-attack as long as the flow separation remained quasi-stationary. A discussion of each figure will better explain the comparisons shown.

At $WKIA = 36$ (175.5) and $V_T = 172$ (318.5), one would expect the total pressure recovery maps with and without engine interaction to be quite different when compared at the same angle-of-attack because of the increase in the separation angle-of-attack caused apparently by engine interaction. The recovery maps in figures 48 and 49 confirm this prediction. While the low total pressure recovery region without engine interaction ($\alpha = 28^\circ$) was quite large, the comparable region with engine interaction ($\alpha = 28^\circ$) is much smaller. Of course

this is due in a large part to the fact that the boundary layer has not yet separated at $\alpha = 28^\circ$ with engine interaction. Additional recovery data with engine interaction where diffuser separation was detected ($\alpha = 30^\circ$) is also shown in figure 48. Little change in pressure recovery is visible. Figure 49 continues this comparison with data from a repeat run with engine interaction which repeated the $\alpha = 30^\circ$ condition and extended the angle-of-attack range to $\alpha = 31^\circ$. The repeat data at $\alpha = 30^\circ$ agree with the data of figure 48 and the pressure recovery at $\alpha = 31^\circ$ begins to show some growth in the size of the low recovery region. But again this region at $\alpha = 31^\circ$ is much smaller by comparison to that measured without engine interaction at $\alpha = 28^\circ$.

For the same inlet airflow, total-pressure recovery maps with and without engine interaction show similar results at $V_T = 147$ (272.2), figure 50 and $V_T = 186$ (344.5), figure 51. At $V_T = 147$ (272.2), recovery with engine interaction was not measured at the separation angle-of-attack. However, the comparison would have been as previously shown because inlet separation (in the diffuser) was not detected with engine interaction until $\alpha = 35^\circ$. The recovery at $\alpha = 35^\circ$ is used for comparison. Both inlet configurations had the same separation boundary angle-of-attack at $V_T = 186$ (344.5), but the smaller size of the low total pressure recovery region with engine interaction reflects the less developed flow separation.

A representative comparison of total-pressure recovery maps at lower inlet airflows is presented in figures 52 and 53. At these inlet airflows some success was achieved in passing through the non-stationary separation region far enough to achieve a quasi-stationary separation. The importance of this data is that total-pressure recovery maps with engine interaction in which inlet boundary-layer separation has developed beyond diffuser separation can now be compared to similar data without engine interaction. In both figures 52 and 53, the size of the low total-pressure recovery region is smaller with engine interaction.

Several recovery map comparisons with and without engine interaction that could have cleared up some uncertainties in the data were not obtained because of pressure sampling limitations or engine stress limits. A particular case in point is the data at $V_T = 147$ (272.2) and $WKIA = 32$ (156) in which the separation boundary without engine interaction was slightly higher than with engine interaction as shown previously in figure 46. However, engine stress levels caused termination of the α polar one degree below where inlet separation occurred without engine interaction. Even though the measured data with engine interaction appeared to restrict the radial and circumferential growth of the low total-pressure recovery region (given the limitation of the instrumentation), a true comparison can only be made at the same angle-of-attack and with pressure sampling methods consistent with the separation characteristic encountered.

INLET DISTORTION

Any rigorous comparison for fan-face total-pressure distortion levels must again reflect operating conditions consistent with pressure measurement methods used in this investigation. Accordingly, comparisons of the effect of engine interaction have been limited to the same range of operating conditions reviewed in the previous sections on fan-face total-pressure recovery maps.

Three different inlet distortion indices are compared with and without engine interaction on

figures 54 to 58. Each inlet distortion index is plotted versus inlet angle-of-attack for essentially constant inlet airflow and airspeed. In the initial plot of each operating condition series, the specific inlet airflow/unit area of each plotted point above $\alpha = 20^\circ$ is identified and is similarly valid for the following plots of IDCTIP and IDCHUB in a given plot series. Presentation of the data in this way was thought to give a better picture of the effects of engine interaction as opposed to plotting distortion indices versus engine airflow/unit area. The reasoning behind this approach is based on two observations. First, inlet performance obtained with engine interaction cannot be properly reviewed at a single angle-of-attack. Secondly, it is important to show that the condition at which some form of inlet flow separation was detected, was approached essentially with the same inlet airflow for both inlet configurations, although the resultant flow separation characteristics were quite different. Further, because the initial measurable separation characteristics were different, the resultant inlet airflows were also different (i.e., greater decreases in inlet airflow without engine interaction caused in part by the more forward location of flow separation).

The inlet distortion indices used in the figures, IDRTIP, IDCTIP and IDCHUB, represent a computational procedure developed by the General Electric Company and are used here by permission from that organization. The distortion descriptor elements of this computational procedure comply with SAE aerospace recommended practice 1420. The importance of using these types of distortion indices is that they are weighted to depend not only on the magnitude of the total-pressure deficit, but also on the radial and circumferential size of the low total-pressure region. It has been shown in reference 5 that the size of the low total-pressure recovery region, and in particular the circumferential extent, can be directly related to rotor blade loading and compressor stability margin. Reduction in the circumferential extent of the low total-pressure recovery region tends to reduce rotor blade loading excursions by raising the blade reduced frequency which lowers the blade unsteady lift response.

Recall from figures that the one dominant effect of engine interaction was to reduce the size (both radially and circumferentially) of the low total-pressure recovery region which should be substantiated by the comparison of distortion levels. A review of the data shows this to be the case. At an inlet airflow/unit area of WKIA = 36 (175.5), figures 54 to 56, engine interaction allows the inlet to be operated beyond the angle-of-attack of separation experienced without engine interaction and at lower distortion levels. The lower distortion levels being caused, in a large part, by the reduced size of the low total-pressure recovery region.

Additional data for lower inlet airflows is shown in figures 57 and 58 and reflects operating the inlet, with engine interaction, slightly beyond the non-stationary separation angle-of-attack region. Here again, engine interaction allows the inlet to be operated at or beyond the angle-of-attack of separation experienced without engine interaction with lower distortion levels.

The manner in which this improvement occurs seems to involve initially a delay in the rate at which the inlet boundary-layer separation process develops with increasing angle-of-attack. It is further suggested that engine interaction is involved at some yet undetermined angle-of-attack interval just before the inlet boundary layer separates. During this interval, the cause for any redistribution of the flow by the rotor is due to the total-pressure deficit of a thickened but unseparated boundary layer. When the rotor responds to the total-pressure deficit and accelerates the flow in that region, there is a corresponding reduction in

local static pressure. The reduced static pressure helps relieve a portion of the inlet diffuser pressure gradient which in turn delays the onset of boundary-layer separation.

As inlet boundary-layer separation occurs and develops, the influence of the fan rotor continues. In the process of accelerating the flow in the low total-pressure recovery region, there will be a three-dimensional bending of the flow streamlines ahead of the fan rotor both toward the duct wall and toward the center of the low total-pressure region. Thus, reducing the radial and circumferential size of the low total-pressure recovery region as shown by the data presented.

From the parallel compressor analyses and experimental work in ref. 3 and 6, it has been shown that the amount of attenuation of axial velocity distortion is a function of the slope of the constant speed lines on the compressor map expressed as static pressure rise versus axial velocity $\frac{\partial \Delta P}{\partial U}$. In reference 3, the more negative the slope, the greater the attenuation of the upstream velocity distortion. In general, the compressor map for a single-stage fan will contain a more negative-slope constant speed line nearer the design point of the compressor or in effect at operating points farther up the operating line (increasing airflow). Possibly, this dependence on the slope of the compressor characteristic may offer some explanation for the variation in separation boundaries and the different rates of inlet distortion increase with increasing angle of attack measured for different inlet airflows, i.e., different engine operating points in this investigation.

CONCLUSIONS

Based on the data presented, it seems reasonable to conclude that engine interaction allows an inlet to be operated with lower distortion levels at and beyond the separation angle-of-attack experienced without engine interaction. Admittedly, this performance advantage could not be confirmed for all test conditions due to mechanical stress limits in the test engine.

It is further suggested that, initially, this reduction in inlet distortion level is the result of engine interaction delaying the onset of inlet boundary-layer separation. Variations in inlet separation boundaries and distortion trends with engine operating point were also thought to show some relationship to predictions from parallel compressor theory and experiment. Theory indicates the amount of distortion attenuation obtained to be dependent on the slope of the constant speed line on the compressor map.

REFERENCES

1. Pearson, H. and McKenzie, A. B., "Wakes in Axial Compressors," *Journal of Royal Aeronautical Society*, 1959, Vol. 63, No. 583.
2. Katz, R., "Performance of Axial Compressors with Asymmetric Inlet Flows," AFOSR TR-59-59, California Institute of Technology, 1958.
3. Callahan, G. M. and Stenning, A. H., "Attenuation of Inlet Flow Distortion Upstream of Axial Flow Compressors," AIAA Paper No. 69-485, 1969.
4. Syberg, J. and Koncsek, J. I., "Low-Speed Tests of Fixed Geometry Inlet For a Tilt Nacelle V/STOL Airplane," NASA CR-151922, 1977.
5. Kimzey, W. F., "An Analysis of the Influence of Some External Disturbances on the Aerodynamic Stability of Turbine Engine Axial Flow Fans and Compressors," AEDC-TR-77-80, 1977.
6. Colpin, J., "Propagation of Inlet Flow Distortions Through an Axial Compressor Stage," *Journal of Engineering For Power*, Vol. 101, 1979.

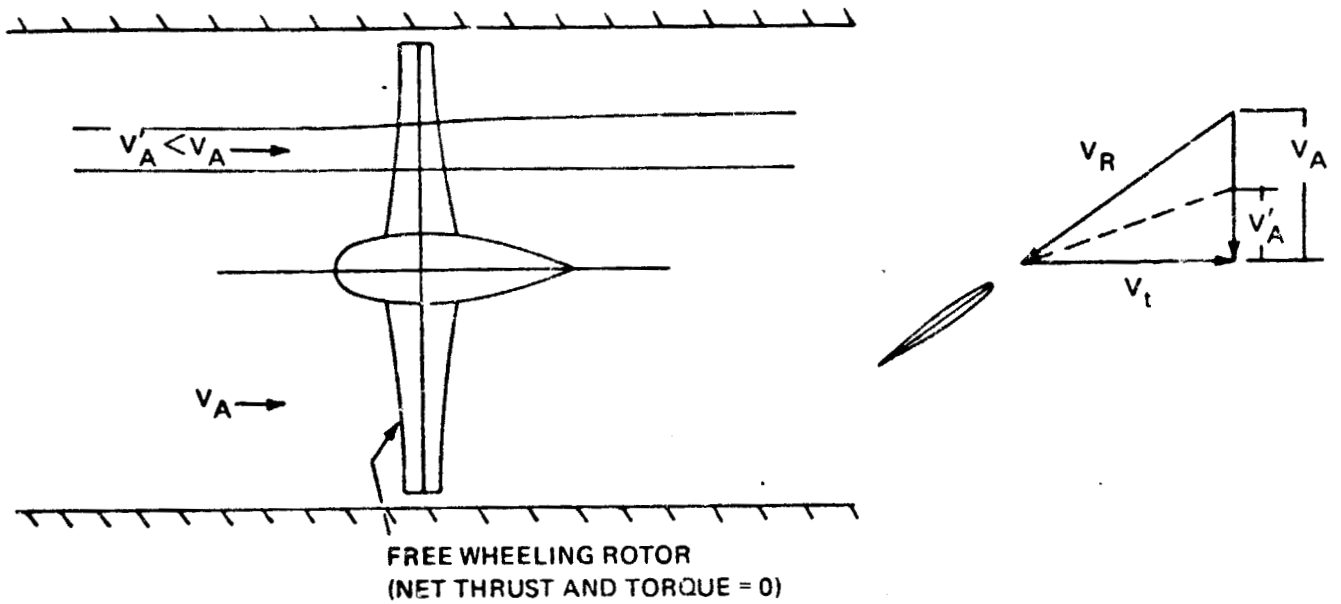


Figure 1.—Definition of Inlet/Engine Flow Field Interaction (Using Windmill Analogy)

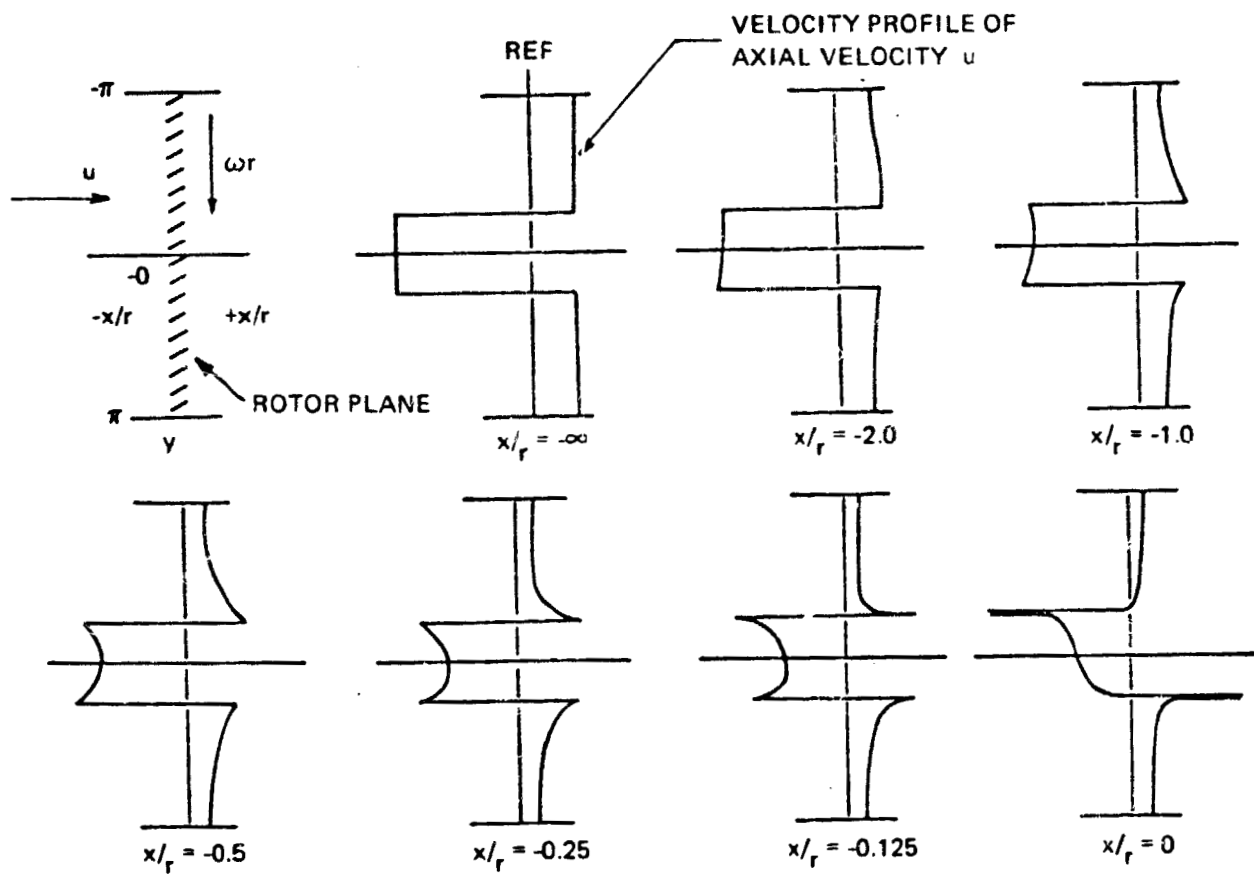


Figure 2.—Redistribution of Distorted Inlet Flow Velocity Caused by a Rotor
(2-D Calculation From Ref. 2)

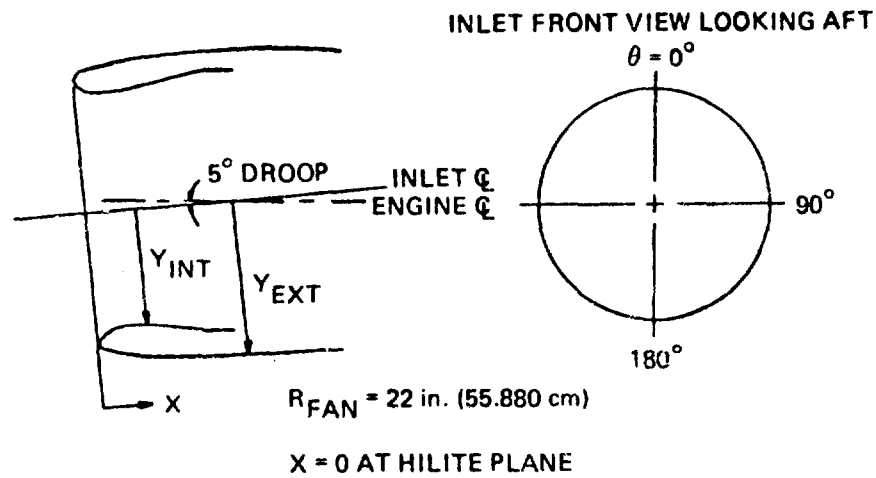


Figure 3.—Inlet Coordinates

$\theta = 0^\circ$			
X/R_{FAN}	Y_{EXT}/R_{FAN}	X/R_{FAN}	Y_{INT}/R_{FAN}
.00000	1.00438	.00000	1.00498
.01127	1.03863	.00504	.97297
.03736	1.06199	.01324	.96096
.06937	1.07579	.02677	.94615
.10411	1.08433	.05644	.92620
.13862	1.08963	.08927	.91296
.17332	1.09331	.12371	.90439
.20907	1.09642	.15899	.89925
.24477	1.09982	.19478	.89659
.28030	1.10475	.23065	.89563
.31580	1.10995	.26621	.89550
.35137	1.11471	.30029	.89552
.38699	1.11905	.33439	.89651
.42089	1.12261	.37019	.89894
.45483	1.12622	.40588	.90258
.48880	1.12931	.43971	.90695
.52280	1.13210	.47345	.91202
.55682	1.13460	.50770	.91771
.59086	1.13684	.54303	.92401
.62492	1.13883	.57829	.93063
.65899	1.14058	.61352	.93747
.69307	1.14213	.64698	.94408
.72892	1.14355	.68116	.95084
.76479	1.14478	.71635	.95781
.80065	1.14585	.74982	.96440
.83521	1.14670	.78331	.97088
.87109	1.14738	.81858	.97748
.90697	1.14786	.85390	.98378
.94108	1.14813	.88931	.98957
.97519	1.14822	.92486	.99447
1.00930	1.14814	.96048	.99875
1.04340	1.14789	.99584	1.00251
1.07751	1.14749	1.03128	1.00446
1.11162	1.14692	1.06712	1.00274
1.14572	1.14621	1.10287	.99961
1.17982	1.14535	1.13861	.99648
1.21392	1.14435	1.17436	.99335
1.24801	1.14321	1.22818	.98865

$\theta = 90^\circ$

X/R _{FAN}	Y _{EXT} /R _{FAN}	X/R _{FAN}	Y _{INT} /R _{FAN}
.00000	1.00203	.00000	1.00203
.00406	1.02305	.01593	.97798
.02603	1.04888	.03867	.95163
.05596	1.06381	.06758	.93282
.08946	1.07345	.09982	.91919
.12374	1.08024	.13351	.90945
.15833	1.08610	.16758	.90286
.19274	1.09282	.20207	.89863
.22713	1.09973	.23708	.89636
.26163	1.10611	.27177	.89556
.29621	1.11199	.30585	.89551
.32916	1.11713	.33920	.89634
.36218	1.12187	.37421	.89858
.39524	1.12623	.40913	.90199
.42836	1.13024	.44394	.90637
.46151	1.13393	.47693	.91125
.49469	1.13732	.51155	.91693
.52791	1.14044	.54509	.92304
.56114	1.14332	.58058	.92947
.59440	1.14598	.61502	.93613
.62939	1.14858	.64774	.94257
.66439	1.15100	.68045	.94905
.69940	1.15327	.71486	.95586
.73126	1.15522	.74758	.96232
.76528	1.15720	.78031	.96870
.80132	1.15900	.81307	.97492
.83637	1.16063	.84759	.98120
.86969	1.16204	.88195	.98709
.90302	1.16331	.91532	.99192
.93535	1.16445	.95109	.99655
.96969	1.16546	.98612	.99850
1.00303	1.16636	1.02121	.99950
1.03637	1.16714	1.05629	.99850
1.06972	1.16782	1.09138	.99850
1.10307	1.16840	1.12646	.99850
1.13642	1.16888	1.15007	.99850
1.17150	1.16930		

 $\theta = 180^\circ$

X/R _{FAN}	Y _{EXT} /R _{FAN}	X/R _{FAN}	Y _{INT} /R _{FAN}
.00000	1.01343	.00000	1.01343
.01245	1.04082	.00979	.98304
.03992	1.05842	.02095	.96953
.06974	1.07009	.04178	.95270
.10076	1.08082	.07011	.93683
.13211	1.09054	.10021	.92468
.16375	1.09929	.13161	.91510
.19562	1.10712	.16328	.90784
.22811	1.11378	.19560	.90228
.25675	1.11976	.22819	.89848
.28751	1.12510	.26023	.89610
.31837	1.12989	.29356	.89538
.34931	1.13418	.32478	.89609
.38031	1.13804	.35755	.89792
.41135	1.14154	.39025	.90083
.44243	1.14475	.42225	.90465
.47353	1.14773	.45375	.90896
.50622	1.15068	.48612	.91404
.53892	1.15352	.51848	.91956
.57163	1.15634	.55078	.92541
.60432	1.15920	.58303	.93151
.63675	1.16203	.61525	.93778
.66946	1.16474	.64586	.94383
.70219	1.16731	.67799	.95019
.73492	1.16977	.71019	.95656
.76604	1.17200	.74080	.96260
.79717	1.17414	.77143	.96857
.82831	1.17619	.80208	.97440
.85945	1.17816	.83437	.98031
.89059	1.18005	.86670	.98593
.92174	1.18189	.87973	.98553
.95289	1.18367	.91105	.98822
.98405	1.18540	.94375	.99109
1.01521	1.18708	.97645	.99395
1.04798	1.18882	1.00915	.99681
1.08076	1.19053	1.05430	1.00076

Figure 3.—(Concluded)

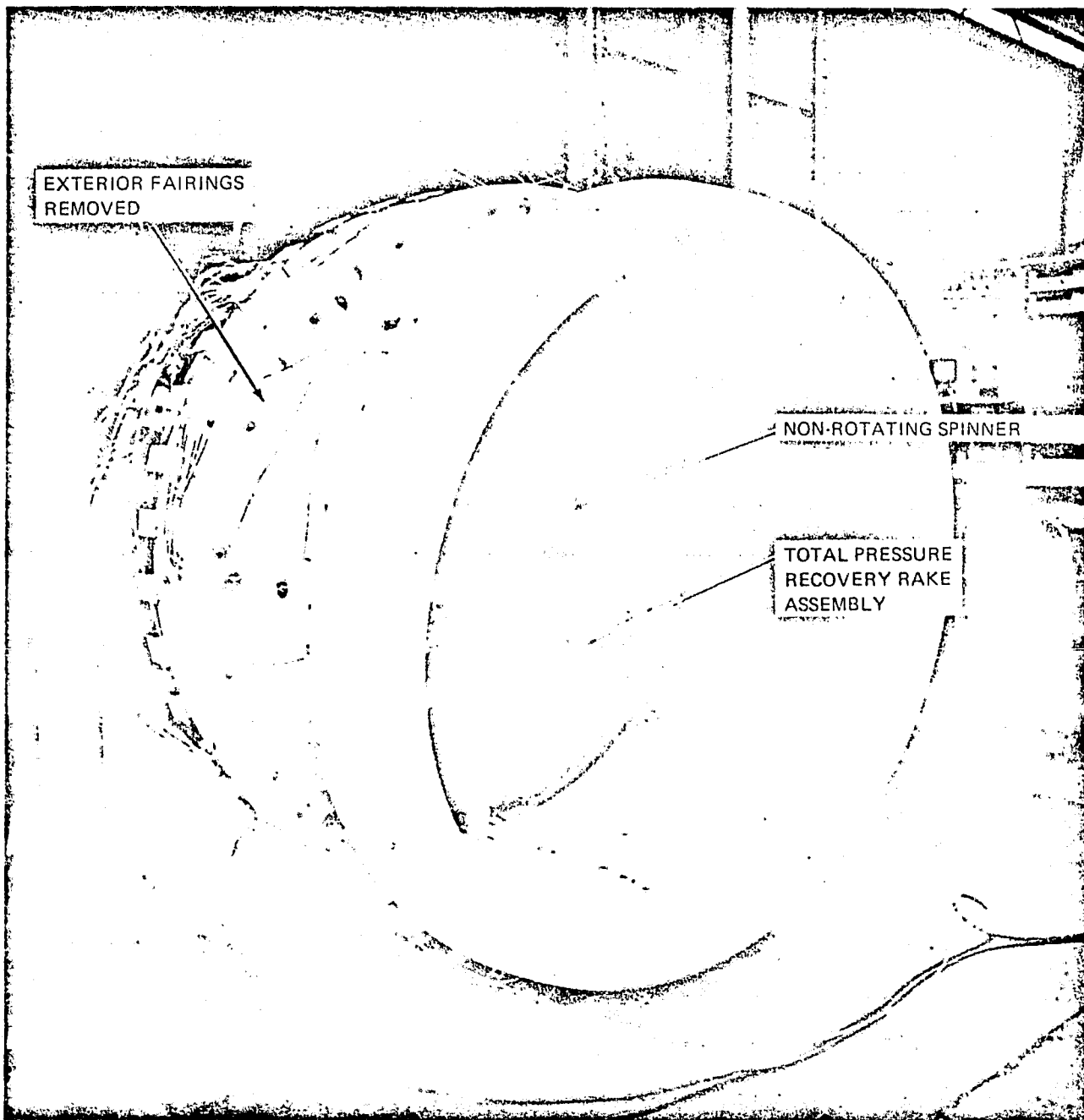


Figure 4.—Front View of Inlet Configuration For the Close-Coupled Inlet Installation

ORIGINAL PAGE IS
OF POOR QUALITY

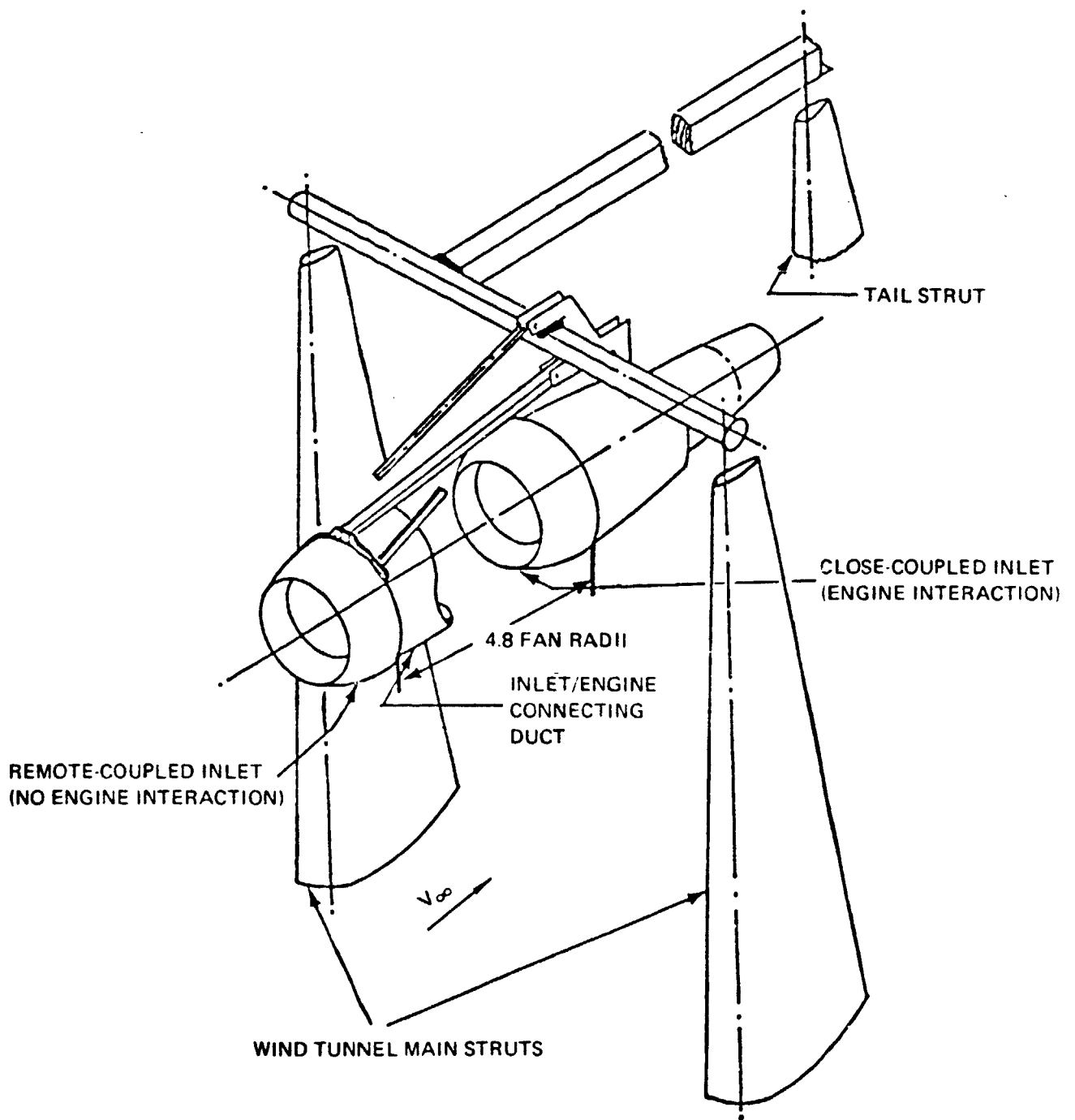


Figure 5.—Conceptual Inlet System With and Without Inlet/Engine Interaction

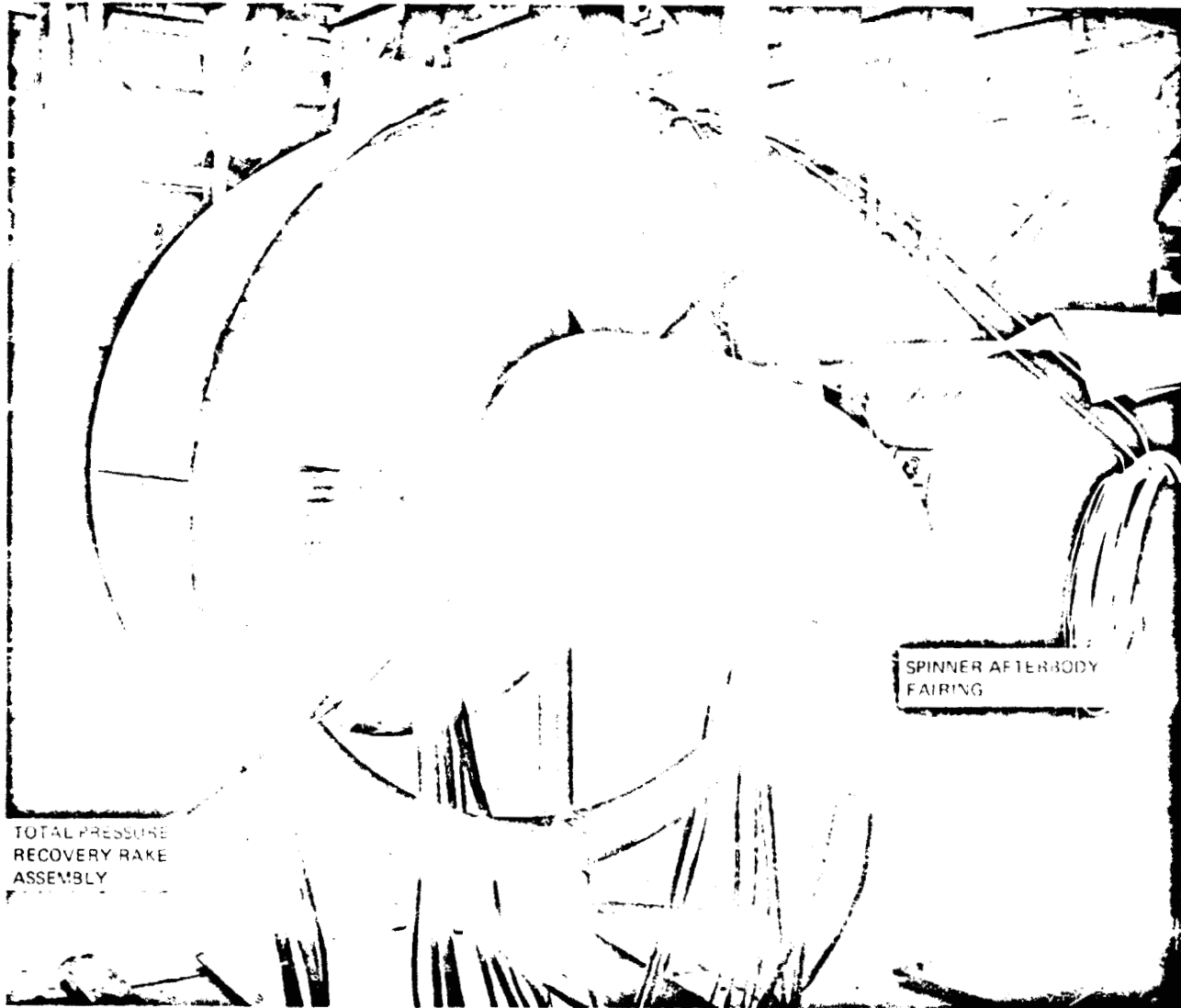
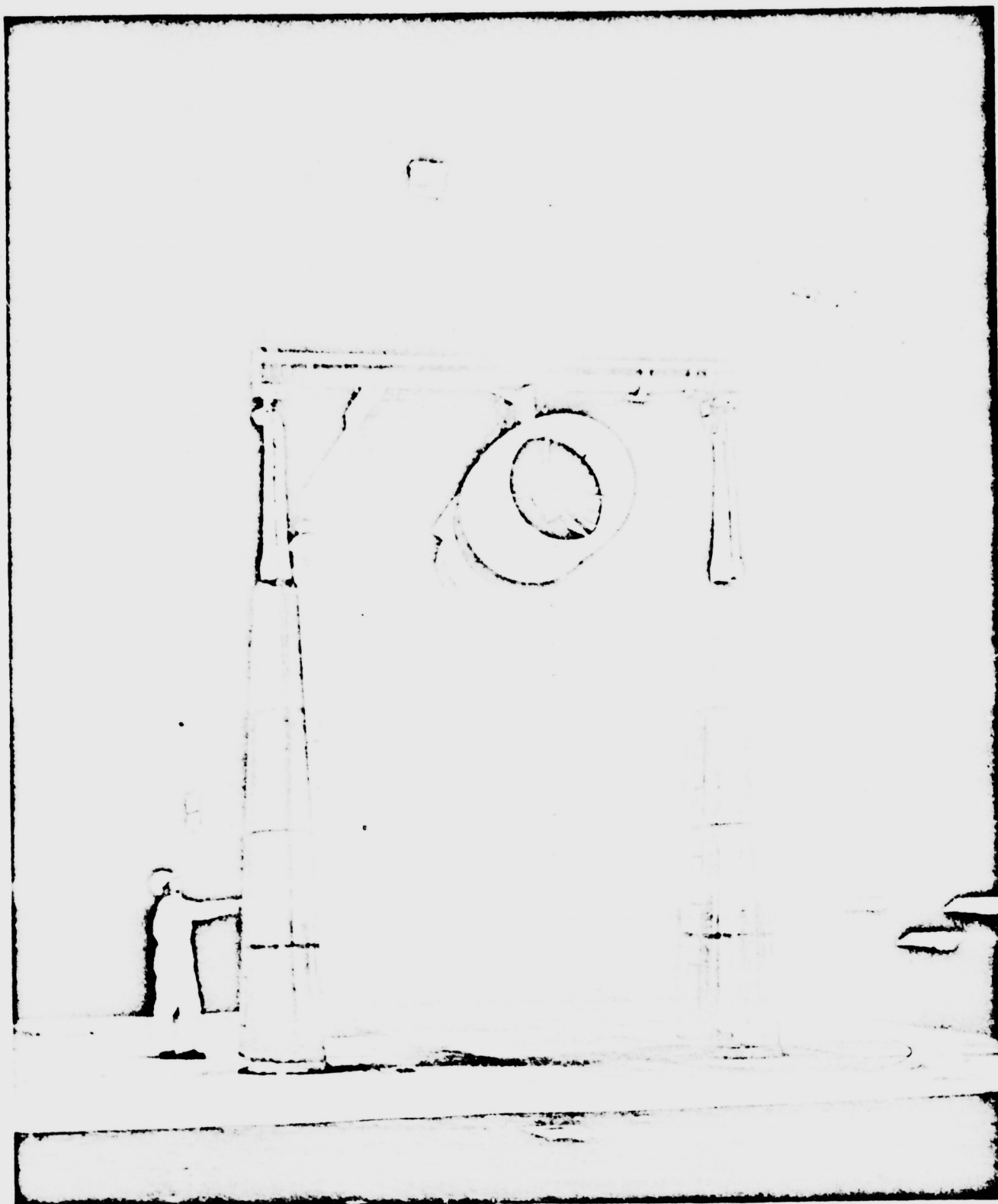


Figure 6.—Aft View of Inlet Configuration For the Remote-Coupled Inlet Installation Showing the Spinner Afterbody Fairing

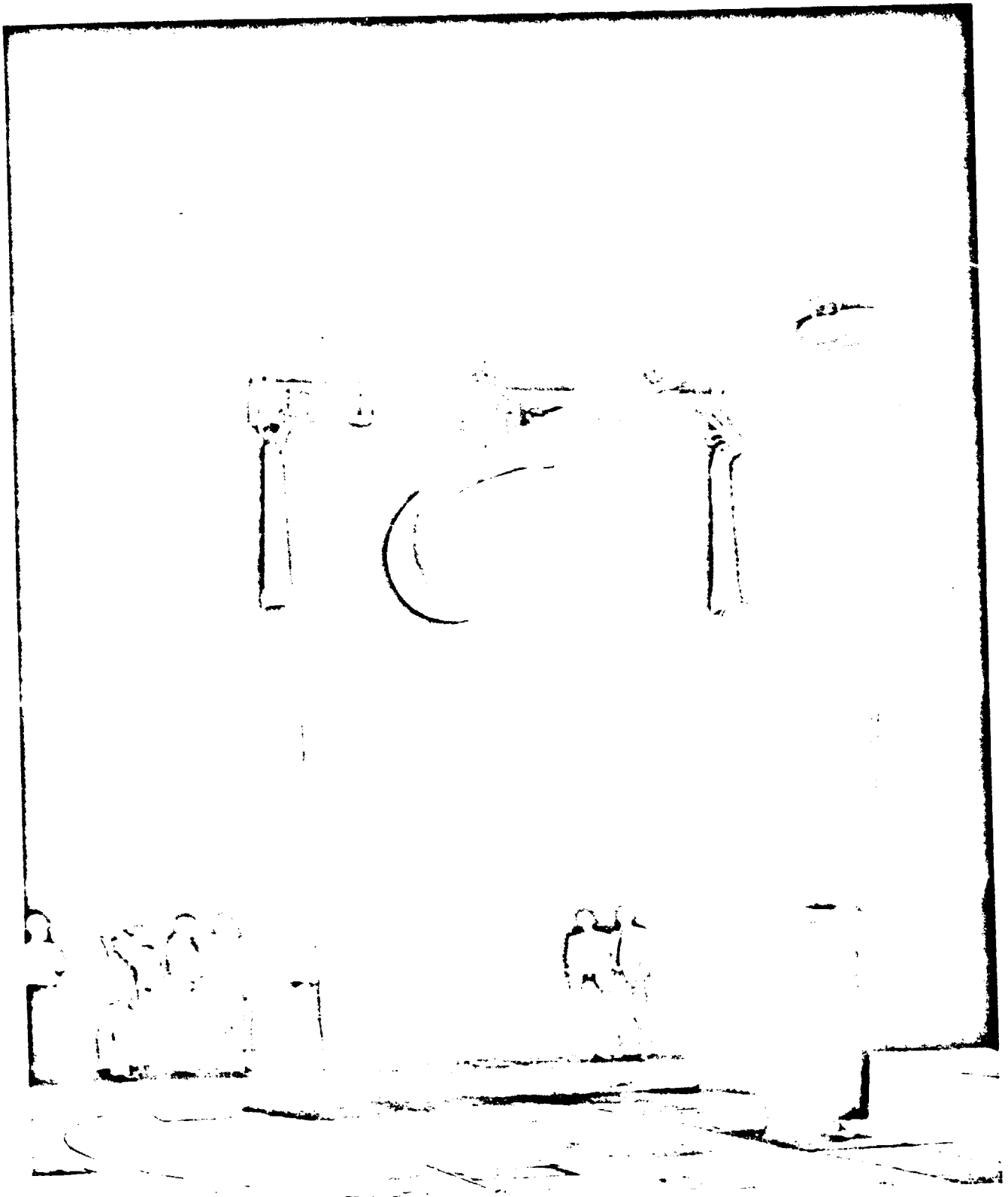
ORIGINAL PAGE IS
OF POOR QUALITY



(a) $\frac{3}{4}$ FRONT VIEW

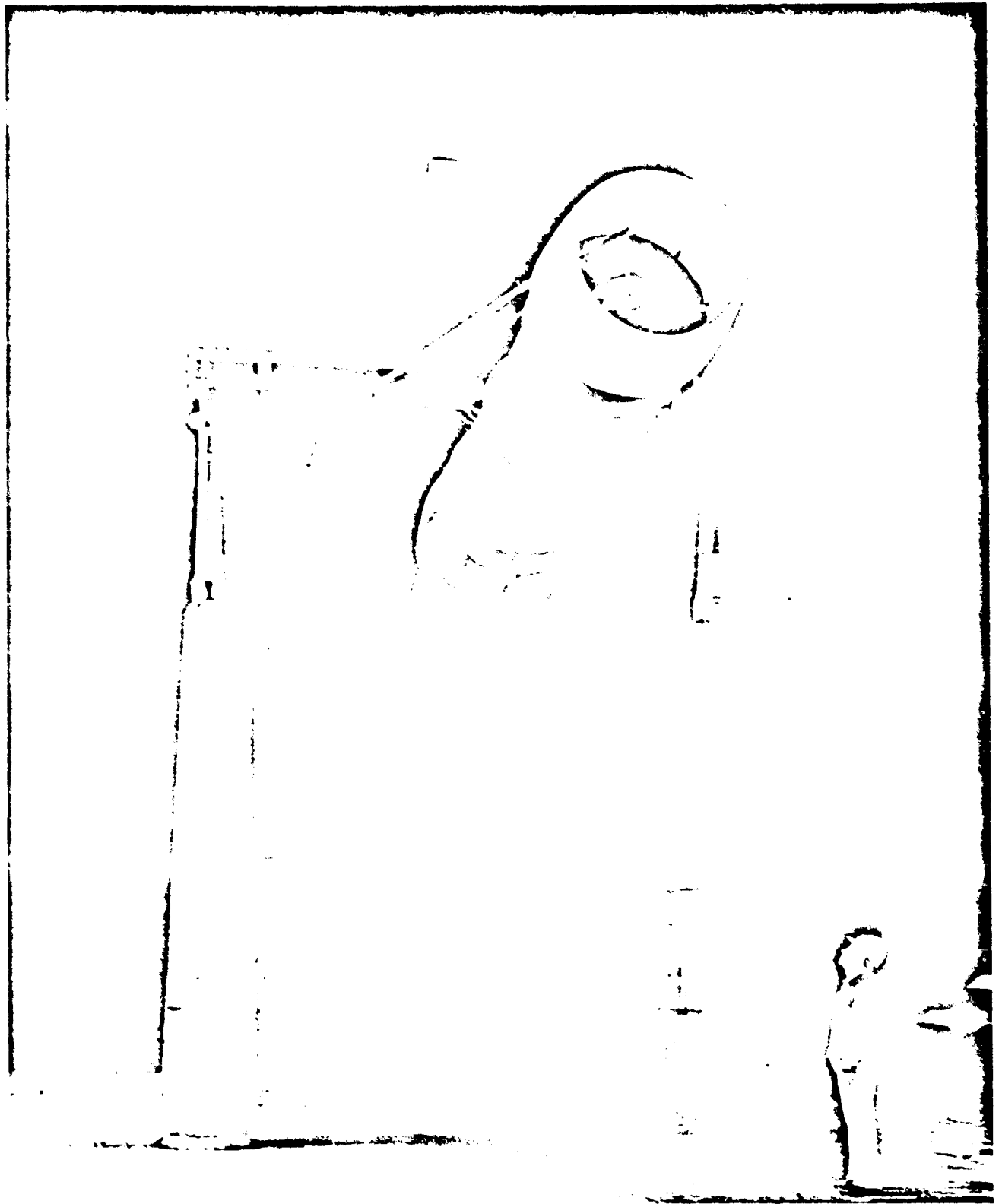
*Figure 7.—Close-Coupled Engine/Inlet Installation Mounted in the NASA-Ames
40-by-80-Foot Wind Tunnel*

ORIGINAL PAGE IS
OF POOR QUALITY



(b) REAR VIEW

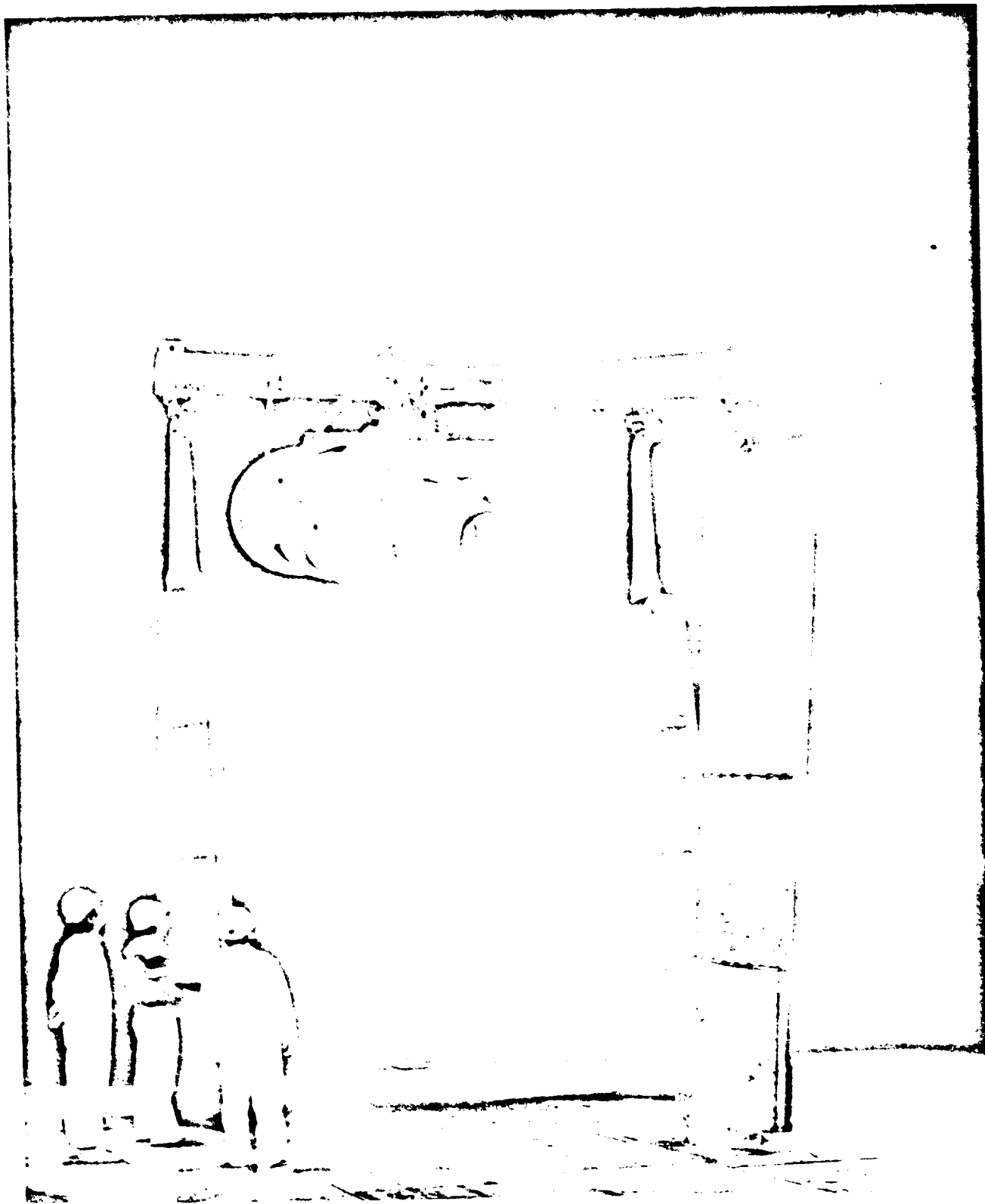
Figure 7.—(Concluded)



(a) $\frac{1}{2}$ FRONT VIEW

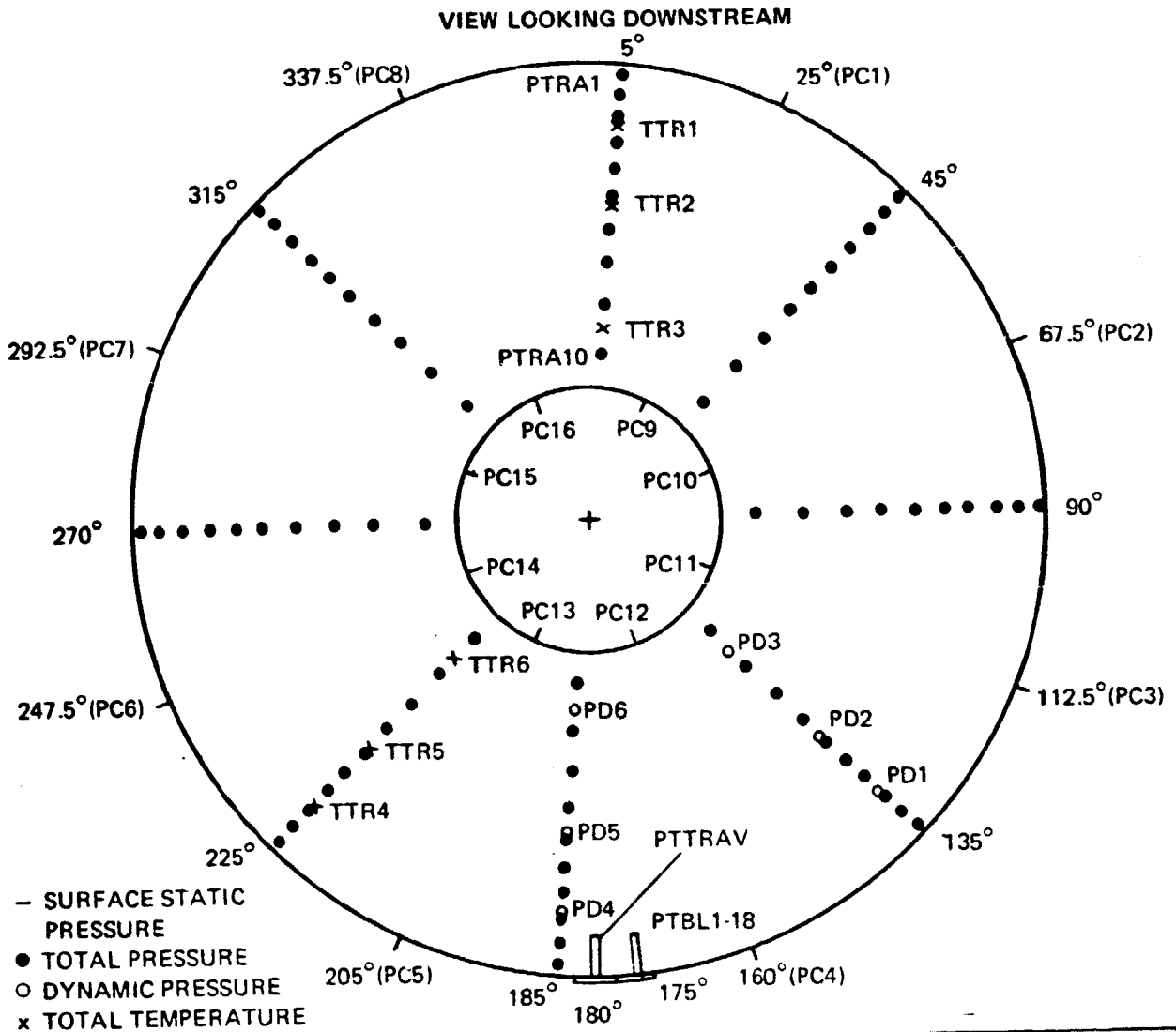
Figure 8.—Remote-Coupled Engine/Inlet Installation Mounted in the NASA-Ames
40- by-80-Foot Wind Tunnel

ORIGINAL PAGE IS
OF 12 PAGES



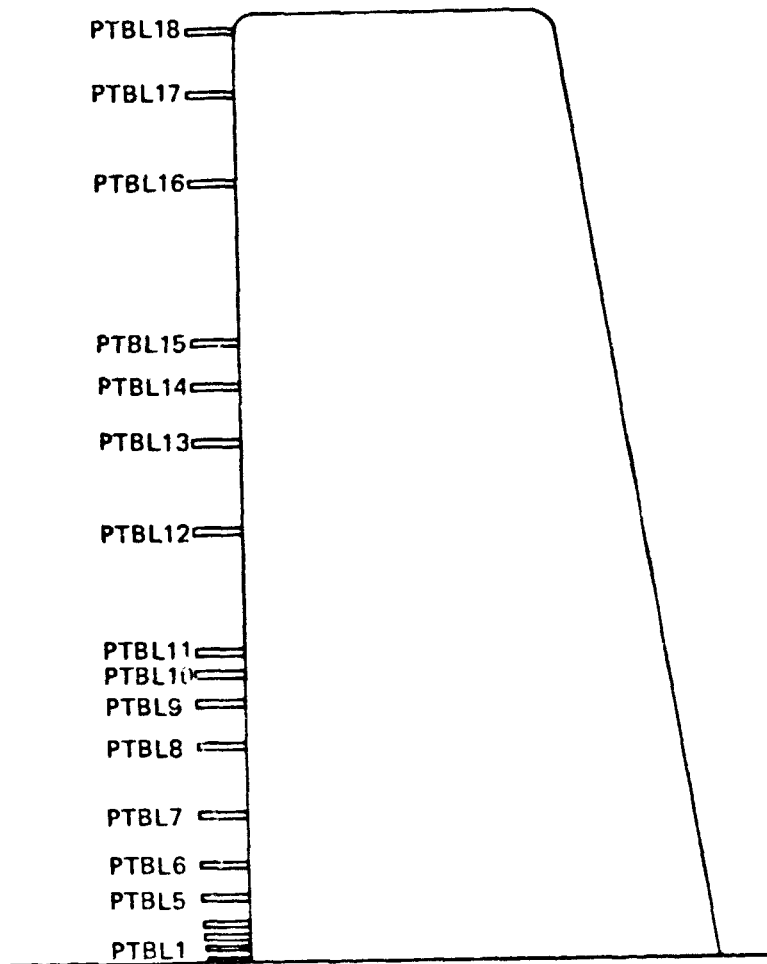
(b) \times REAR VIEW

Figure 8.—(Concluded)



PROBE RADIUS in. (cm)	ANGULAR LOCATION							
	5°	45°	90°	135°	185°	225°	270°	315°
21.49(54.58)	PTRA1	PTRB1	PTRC1	PTRD1	PTRE1	PTRF1	PTRG1	PTRH1
20.43(51.89)	PTRA2	PTRB2	PTRC2	PTRD2	PTRE2	PTRF2	PTRG2	PTRH2
19.32(49.07)	PTRA3	PTRB3	PTRC3	PTRD3	PTRE3	PTRF3	PTRG3	PTRH3
19.16(48.67)	TTR1			PD1	PD4	TTR4		
18.13(46.05)	PTRA4	PTRB4	PTRC4	PTRD4	PTRE4	PTRF4	PTRG4	PTRH4
16.86(42.08)	PTRA5	PTRB5	PTRC5	PTRD5	PTRE5	PTRF5	PTRG5	PTRH5
15.49(29.34)	PTRA6	PTRB6	PTRC6	PTRD6	PTRE6	PTRF6	PTRG6	PTRH6
15.33(38.94)	TTR2			PD2	PD5	TTR5		
13.99(35.53)	PTRA7	PTRB7	PTRC7	PTRD7	PTRE7	PTRF7	PTRG7	PTRH7
12.30(31.24)	PTRA8	PTRB8	PTRC8	PTRD8	PTRE8	PTRF8	PTRG8	PTRH8
10.34(26.26)	PTRA9	PTRB9	PTRC9	PTRD9	PTRE9	PTRF9	PTRG9	PTRH9
9.28(23.57)	TTR3			PD3	PD6	TTR6		
7.91(20.09)	PTRA10	PTRB10	PTRC10	PTRD10	PTRE10	PTRF10	PTRG10	PTRH10

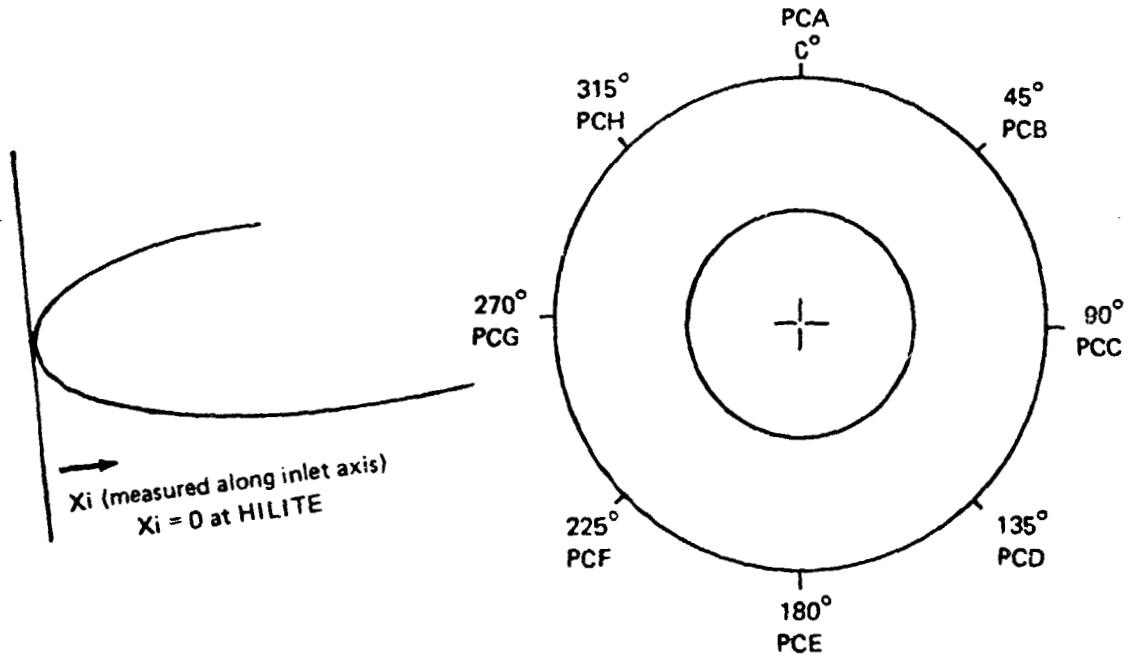
Figure 9.—Fan Face Instrumentation



PROBE	PROBE & DIST TO SURFACE IN. (CM)
PTBL1	0.013(0.033)
PTBL2	0.062(0.157)
PTBL3	0.095(0.241)
PTBL4	0.146(0.371)
PTBL5	0.223(0.566)
PTBL6	0.334(0.848)
PTBL7	0.491(1.247)
PTBL8	0.711(1.806)
PTBL9	0.851(2.162)
PTBL10	0.945(2.400)
PTBL11	1.013(2.573)
PTBL12	1.410(3.581)
PTBL13	1.688(4.287)
PTBL14	1.877(4.768)
PTBL15	2.013(5.113)
PTBL16	2.526(6.416)
PTBL17	2.809(7.135)
PTBL18	3.013(7.653)

Figure 10.—Fan Cowl Boundary Layer Rake

VIEW LOOKING DOWNSTREAM

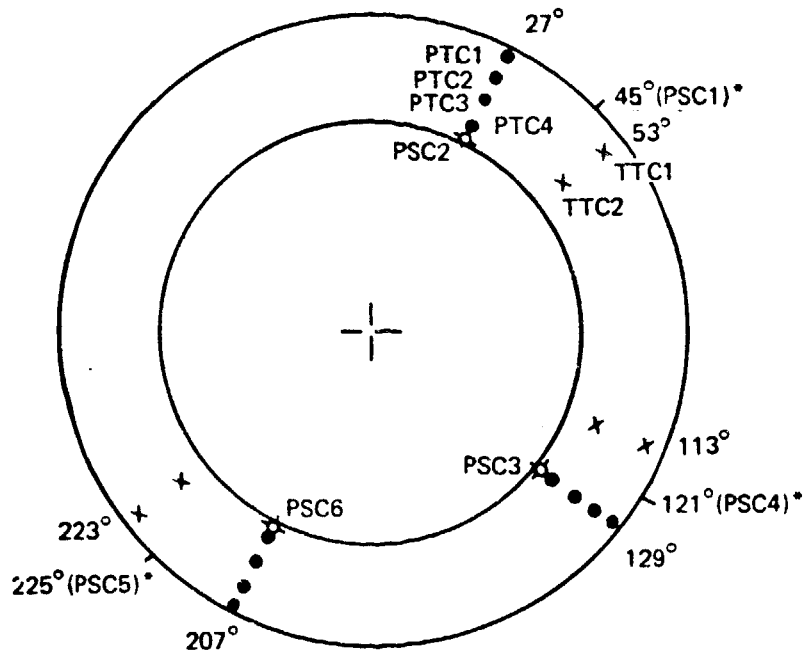


STATION Xi, in. (cm)	ANGULAR LOCATION							
	0°	45°	90°	135°	180°	225°	270°	315°
.469 (1.191)	PCA1				PCE1			
1.06 (2.69)	PCA2				PCE2			
1.88 (4.78)	PCA3				PCE3			
3.05 (7.75)	PCA4				PCE4			
4.45 (11.30)	PCA5				PCE5			
5.86 (14.88)					PD7			
6.10 (15.49)	PCA6	PCB6	PCC6	PCD6	PCE6	PCF6	PCG6	PCH6
7.03 (17.86)	PCA7				PCE7			
7.97 (20.24)					PD8			
8.91 (22.63)	PCA8				PCE8			
10.08 (25.60)					PD9			
11.25 (28.58)	PCA9				PCE9			
12.66 (32.16)					PD10			
14.07 (35.74)	PCA10				PCE10			
15.00 (38.10)	PCA11	PCB11	PCC11	PCD11	PCE11	PCF11	PCG11	PCH11
15.47 (39.29)					PD11			
16.88 (42.88)					PD12			
18.76 (47.65)	PCA12	PCB12	PCC12	PCD12	PCE12	PCF12	PCG12	PCH12
20.63 (52.40)	PCA13				PCE13			
22.04 (55.98)					PD13			
22.51 (57.18)	PCA14				PCE14			

PC - COWL INTERNAL SURFACE STATIC PRESSURE
 PD - COWL INTERNAL SURFACE DYNAMIC PRESSURE

Figure 11.—Inlet Internal Surface Instrumentation

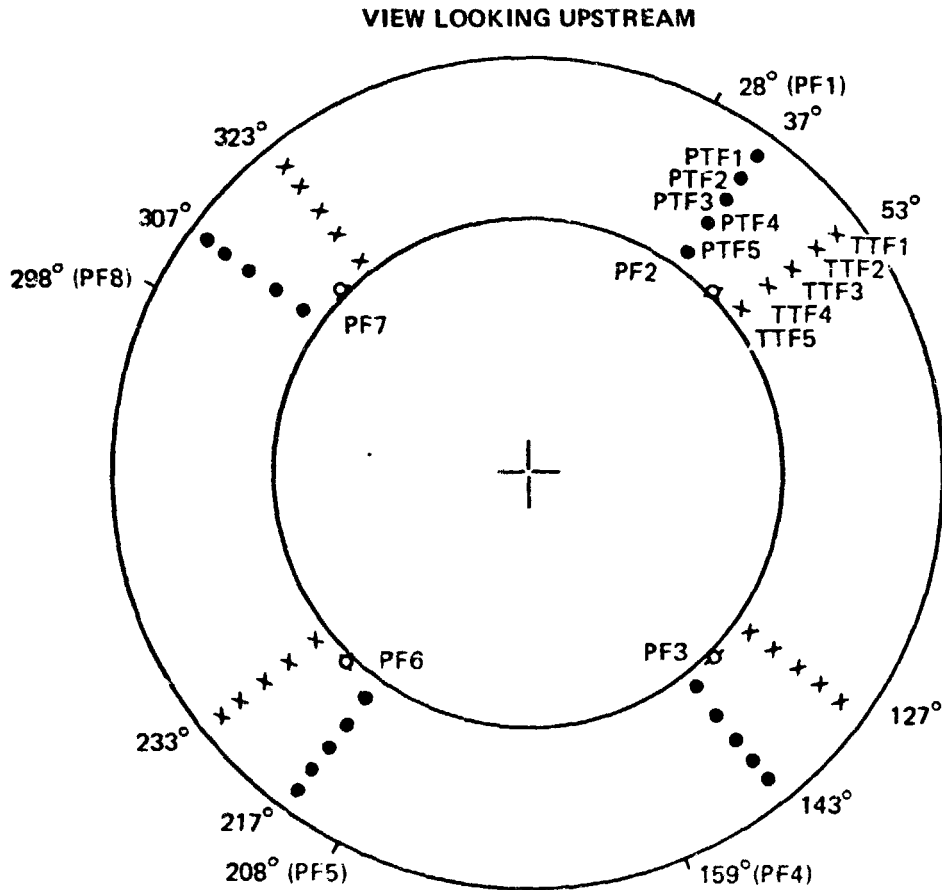
VIEW LOOKING UPSTREAM



PROBE RADIUS in. (cm)	ANGULAR LOCATIONS					
	27°	53°	113°	129°	207°	233°
8.68 (22.05)	PTC1			PTC5	PTC9	
8.33 (21.10)		TTC1	TTC3			TTC5
7.99 (21.16)	PTC2			PTC6	PTC10	
7.23 (20.29)	PTC3			PTC7	PTC11	
6.81 (17.30)		TTC2	TTC4			TTC6
6.38 (16.21)	PTC4			PTC8	PTC12	
6.25 (15.88)	PSC2			PSC3	PSC6	

PTC - COMPRESSOR INLET TOTAL PRESSURE
 TTC - COMPRESSOR INLET TOTAL TEMPERATURE
 PSC - COMPRESSOR INLET STATIC PRESSURE
 * WALL STATICS, PSC1, PSC4, PSC5 AT R = 9.0 in. (22.86 cm)

Figure 12.—Compressor Inlet Instrumentation



PROBE RADIUS in. (cm)	ANGULAR LOCATIONS							
	37°	53°	127°	143°	217°	233°	307°	323°
20.87(53.01)	PTF1	TTF1	TTF6	PTF6	PTF11	TTF11	PTF16	TTF16
19.48(49.48)	PTF2	TTF2	TTF7	PTF7	PTF12	TTF12	PTF17	TTF17
17.98(45.67)	PTF3	TTF3	TTF8	PTF8	PTF13	TTF13	PTF18	TTF18
16.35(41.53)	PTF4	TTF4	TTF9	PTF9	PTF14	TTF14	PTF19	TTF19
14.53(36.91)	PTF5	TTF5	TTF10	PTF10	PTF15	TTF15	PTF20	TTF20
13.88(35.26)	PF2			PF3	PF6		PF7	

PTF - FAN NOZZLE EXIT TOTAL PRESSURE
TTF - FAN NOZZLE EXIT TOTAL TEMPERATURE
PF - FAN NOZZLE EXIT STATIC PRESSURE

Figure 13.—Fan Nozzle Exit Instrumentation

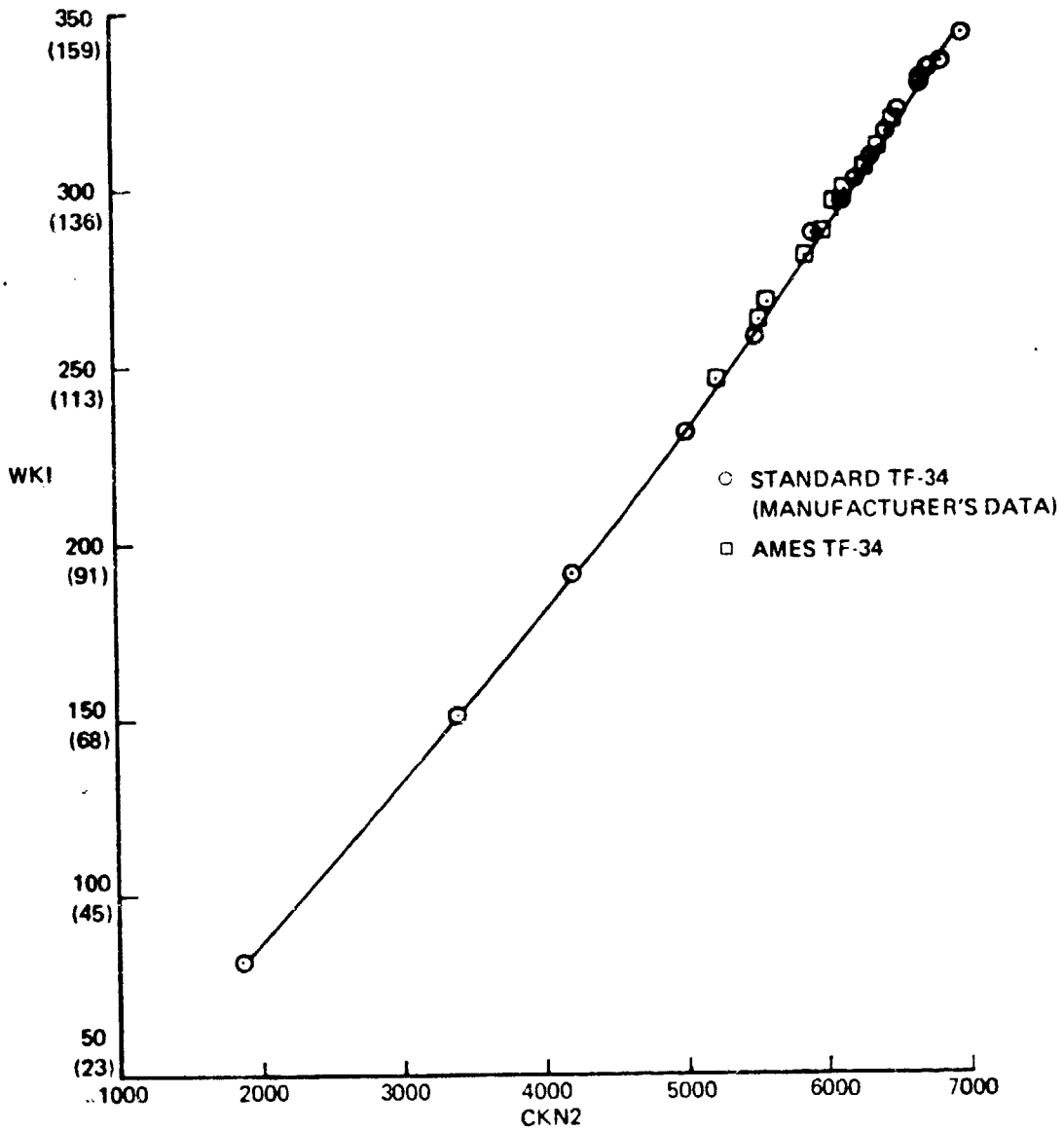


Figure 14.—TF-34 Operating Line Characteristics

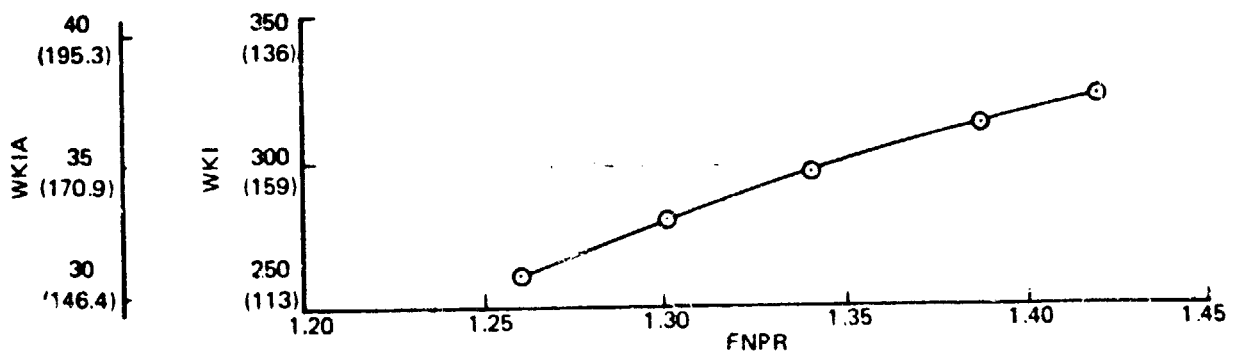


Figure 15.—Inlet Airflow Versus Fan Nozzle Pressure Ratio; Ames TF-34

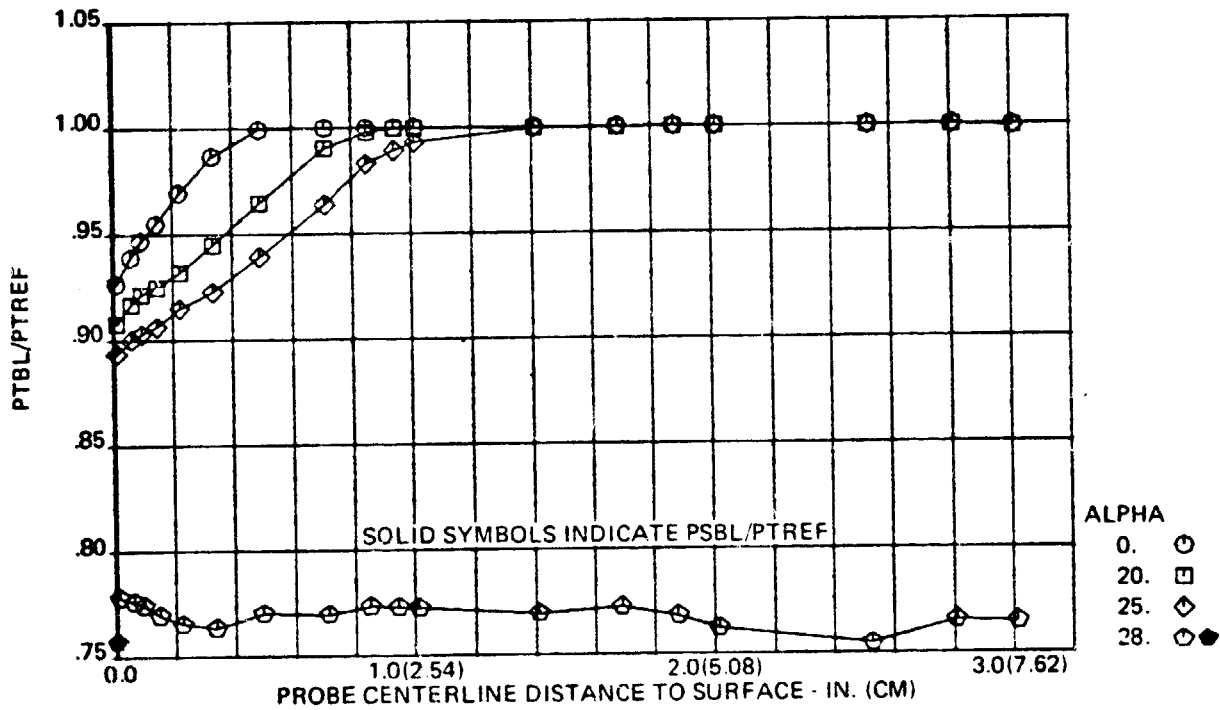


Figure 16.—Variation of Inlet Boundary Layer Total Pressure Profile With Inlet Angle-of-Attack; Without Engine Interaction $V_T = 171.7(318.0)$, $\theta = 175^\circ$, $WKIA = 36.10(176.23)$

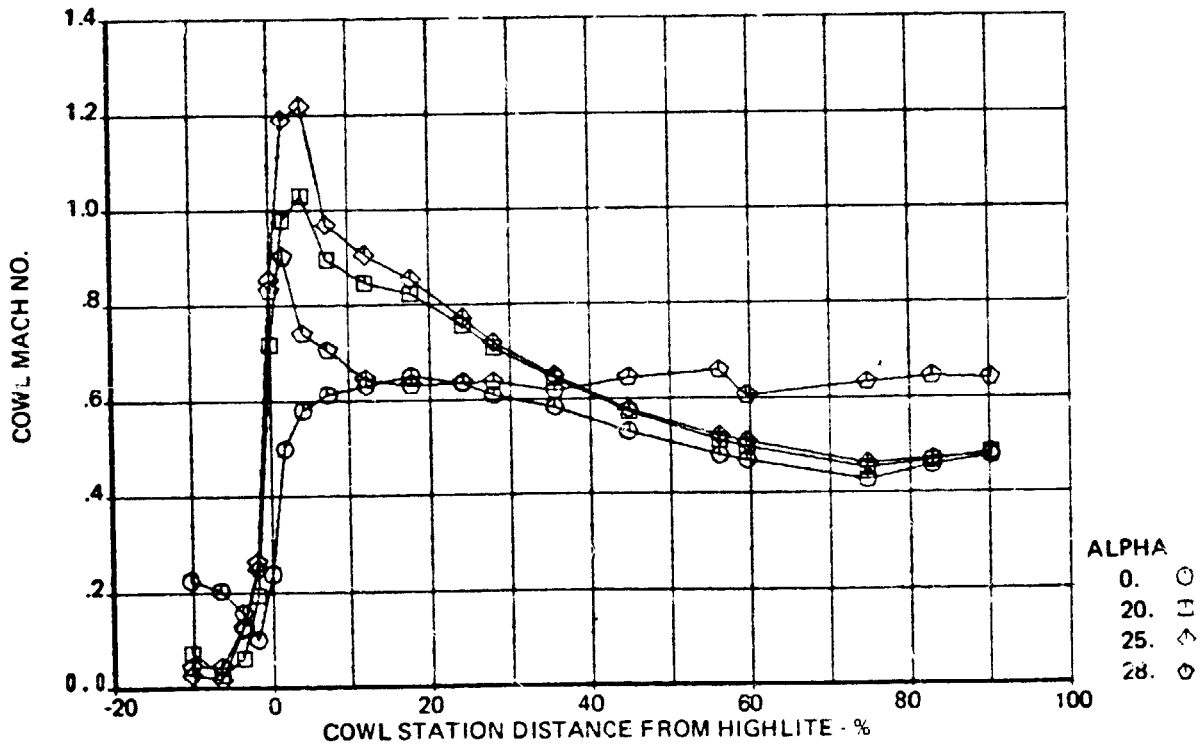


Figure 17.—Variation of Inlet Internal Mach Number Distribution With Inlet Angle-of-Attack; Without Engine Interaction, $V_T = 171.7(318.0)$, $\theta = 180^\circ$, $WKIA = 36.10(176.23)$

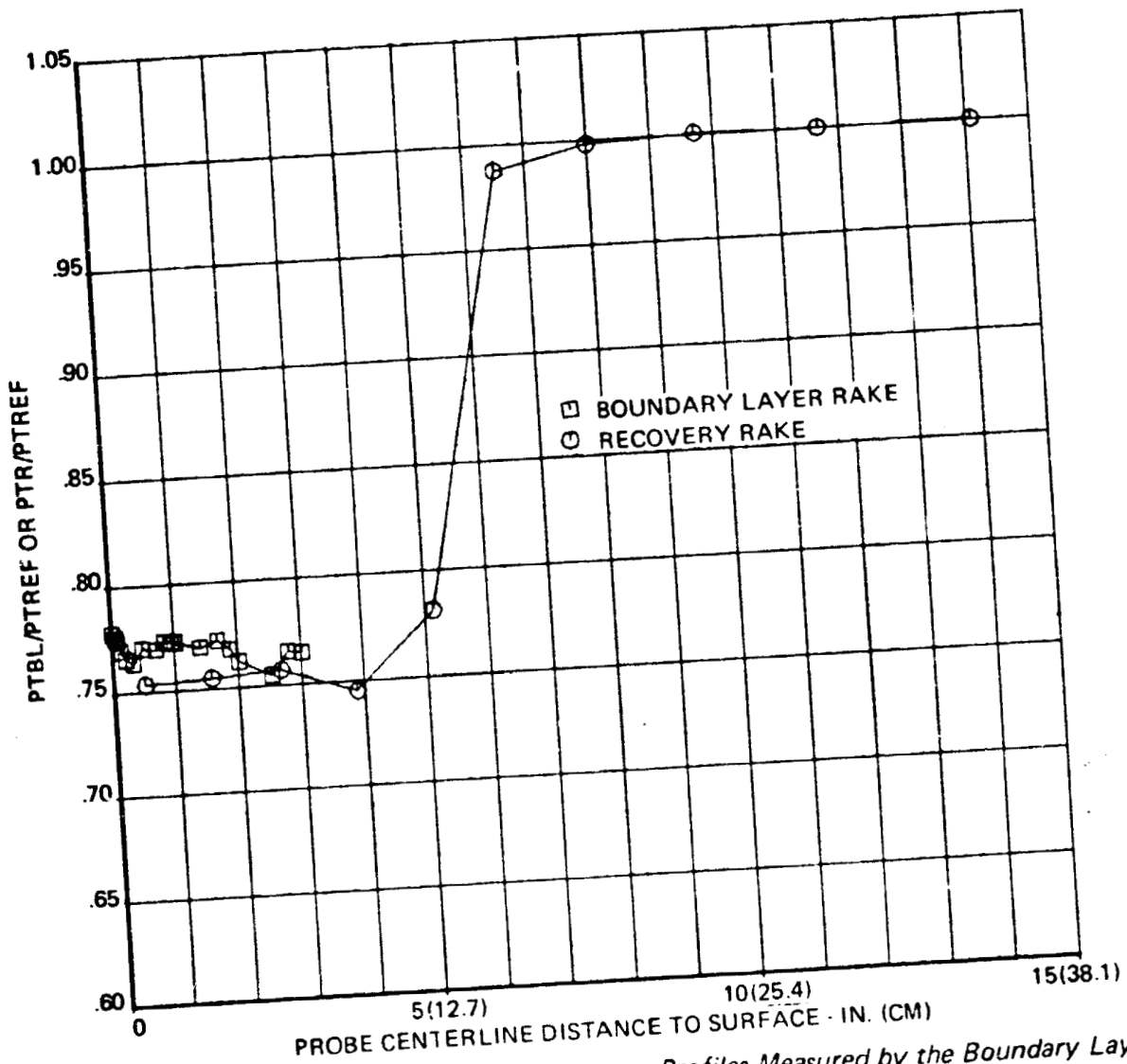


Figure 18.—Comparison of Inlet Total Pressure Profiles Measured by the Boundary Layer Rake and the Recovery Rake With the Inlet Separated; Without Engine Interaction, $V_T = 171.7(318.0)$, $WKIA = 36.10(176.23)$, $\alpha = 28^\circ$

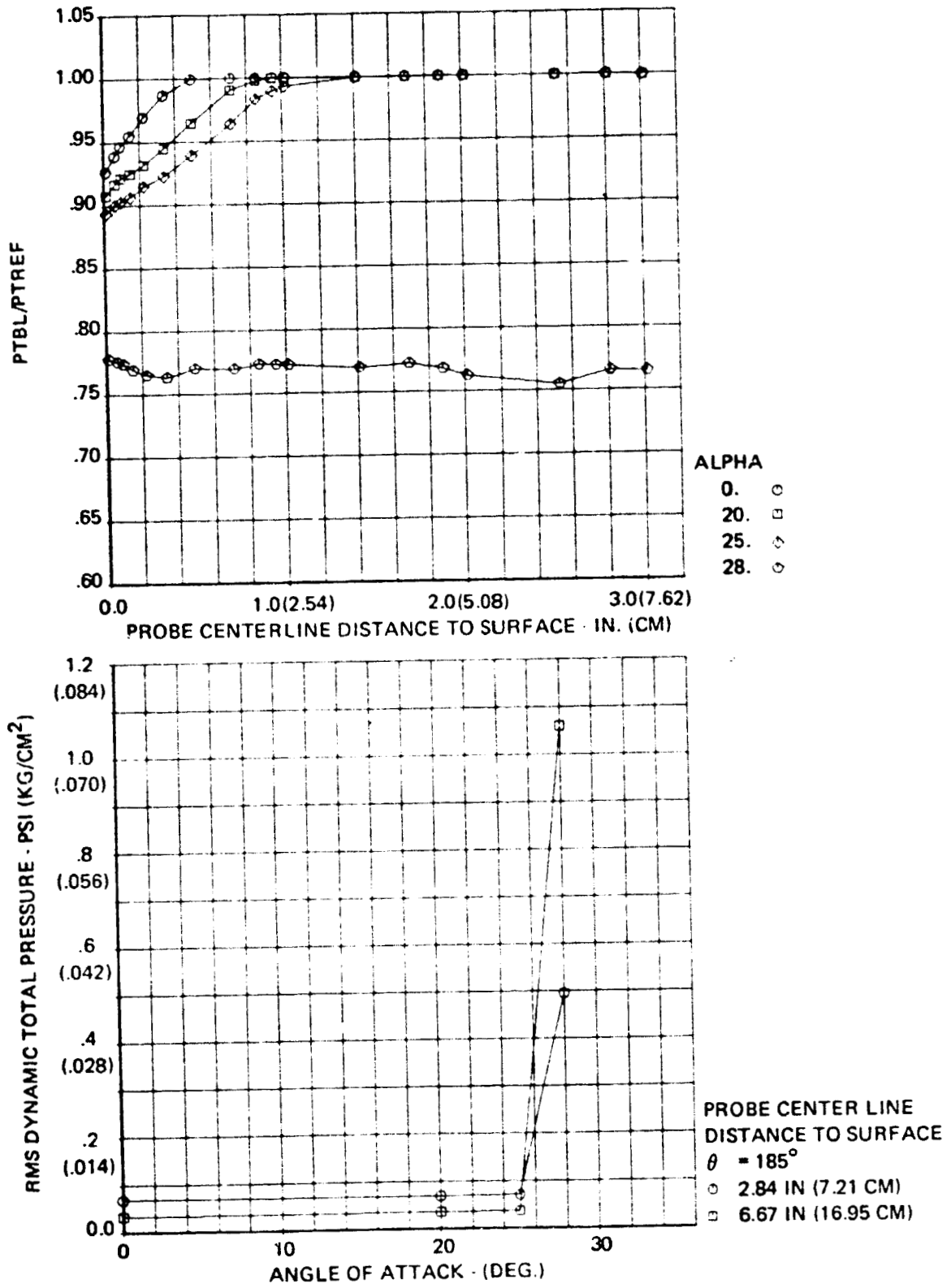


Figure 19.—Variation of Steady-State Inlet Boundary Total Pressure Profiles and RMS Total Pressure Levels With Angle-of-Attack; Without Engine Interaction, $V_T = 171.7(318.0)$, $WKIA = 36.10(176.23)$

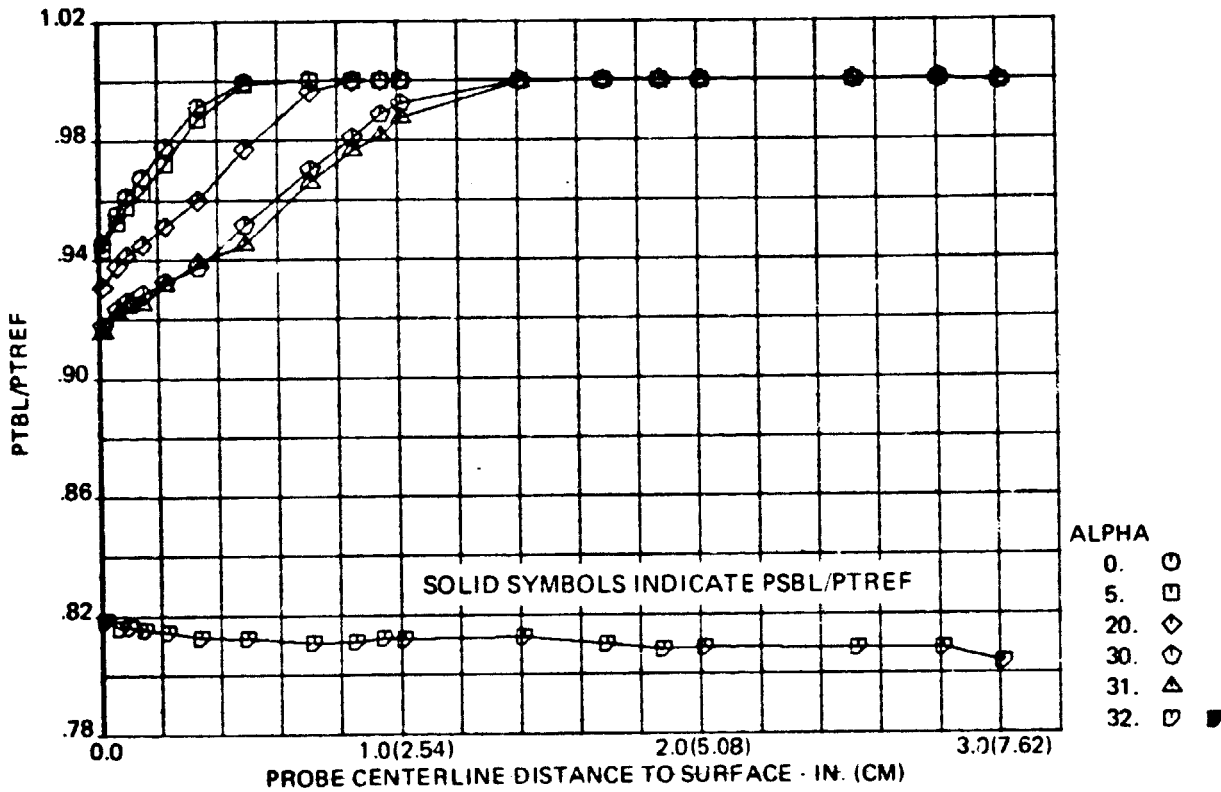


Figure 20.—Variation of Inlet Boundary Layer Total Pressure Profile With Inlet Angle-of-Attack; Without Engine Interaction, $V_T = 147.7(273.5)$, $\theta = 175^\circ$, $WKIA = 32.06(156.5)$

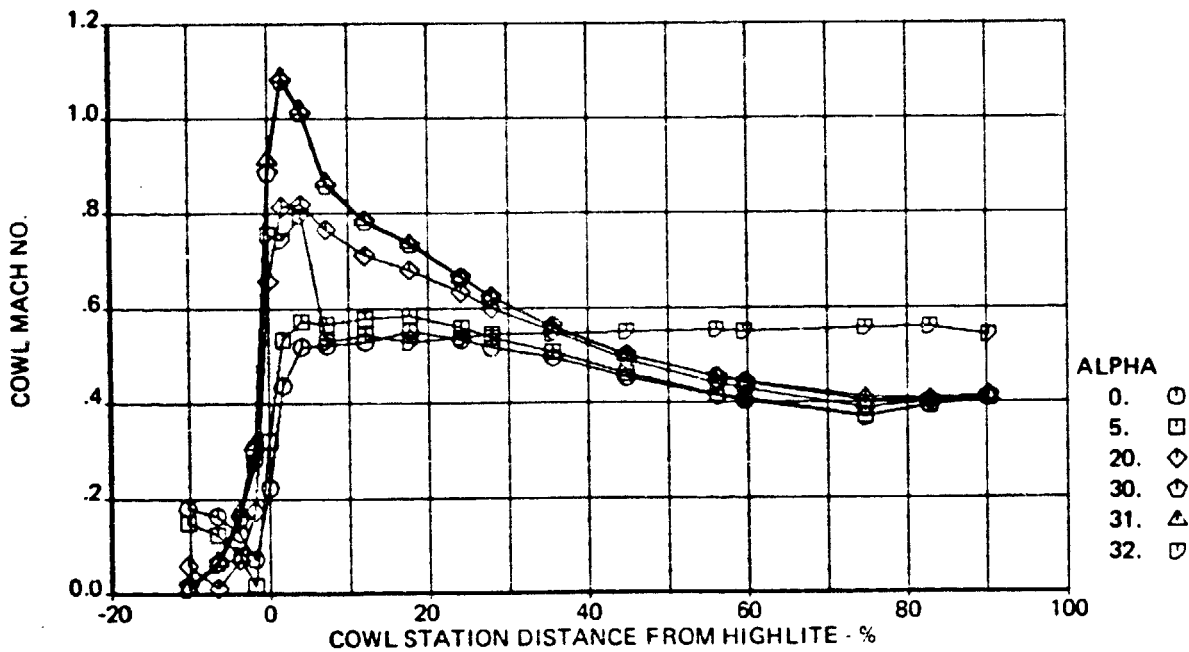


Figure 21.—Variation of Inlet Internal Mach Number Distribution With Inlet Angle-of-Attack; Without Engine Interaction, $V_T = 147.7(273.5)$, $\theta = 180^\circ$, $WKIA = 32.06(156.50)$

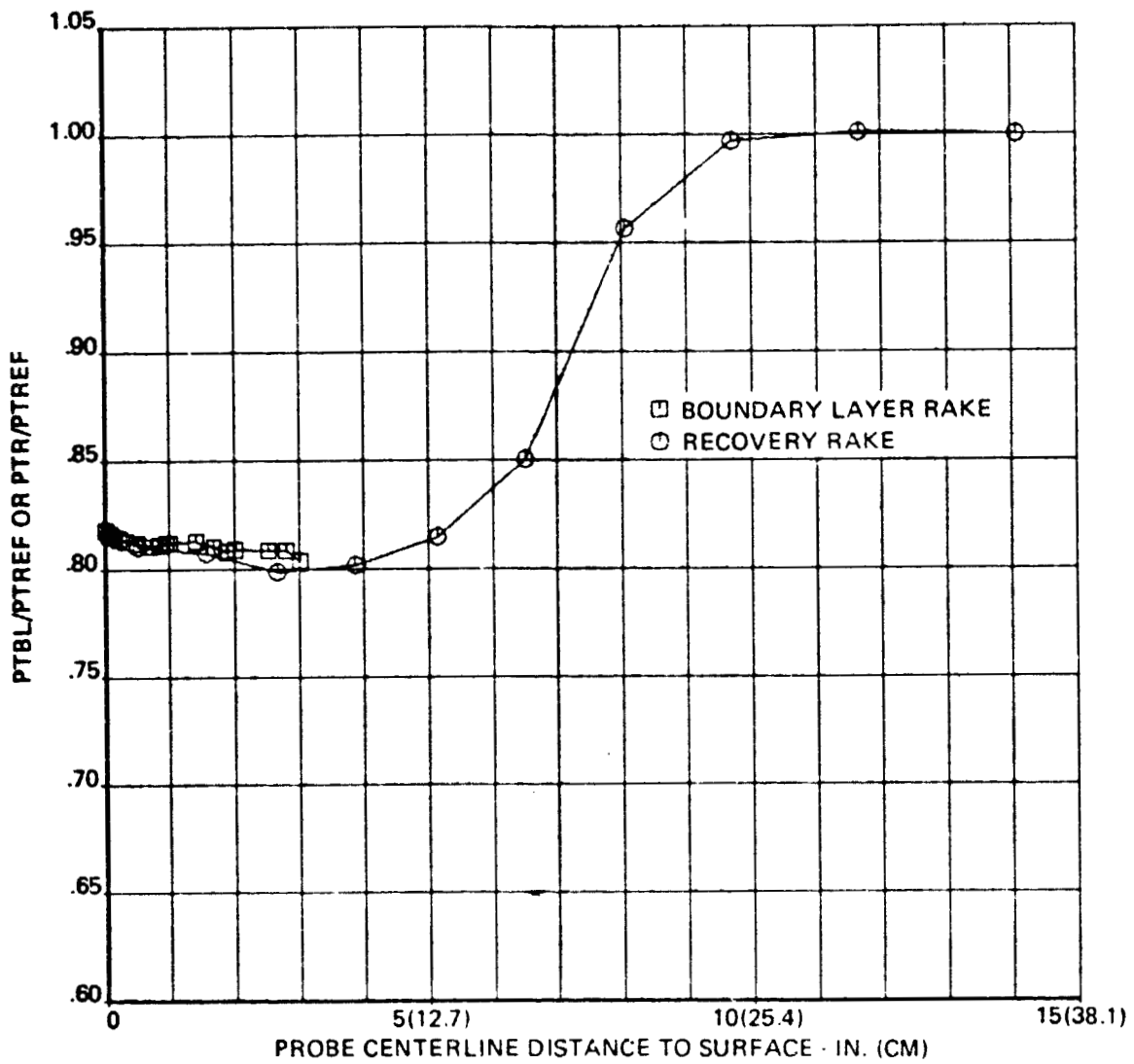


Figure 22.—Comparison of Inlet Total Pressure Profiles Measured by the Boundary Layer Rake and the Recovery Rake With the Inlet Separated; Without Engine Interaction, $V_T = 147.7(273.5)$, $WKIA = 32.06(156.50)$, $\alpha = 32^\circ$

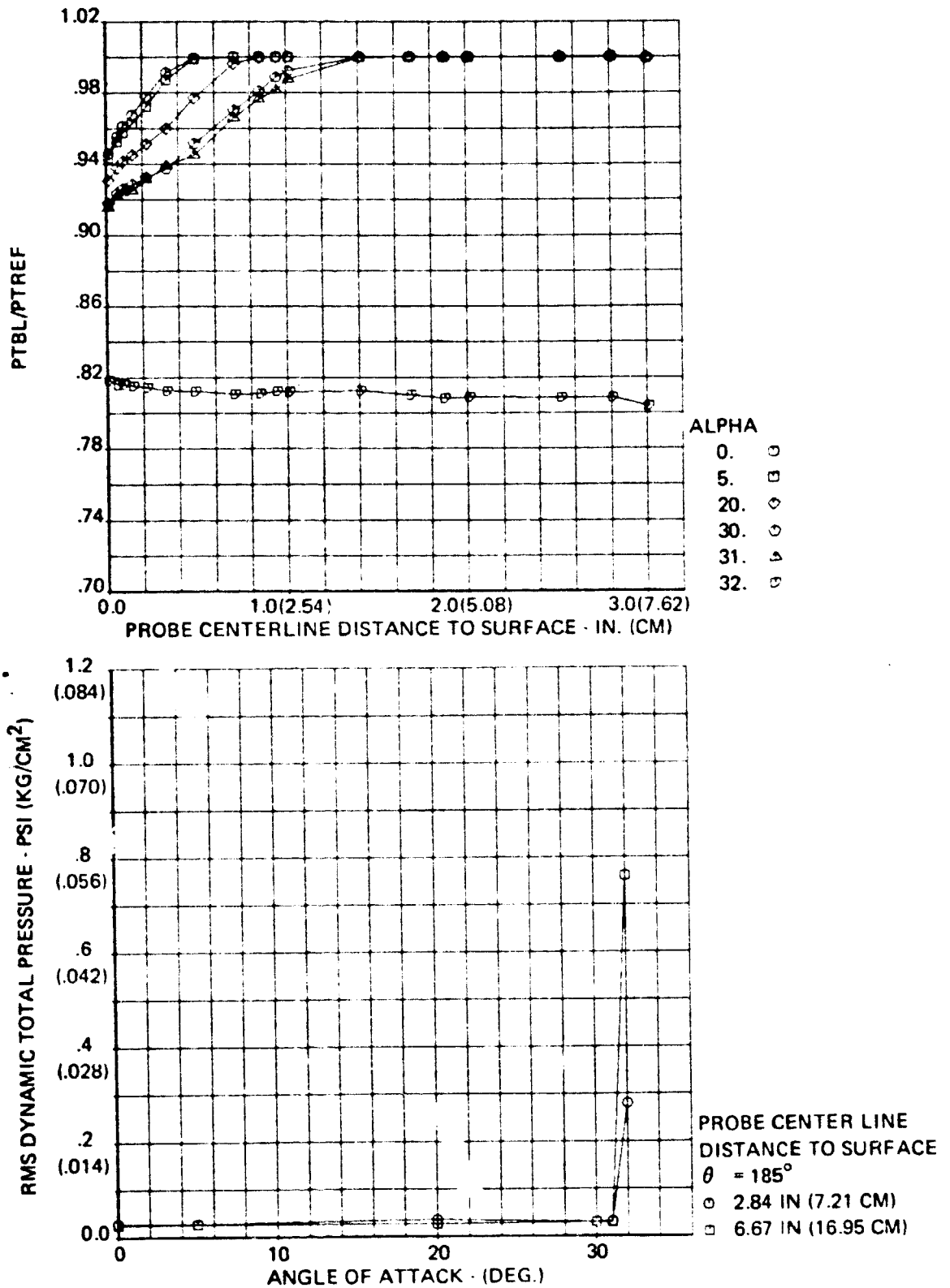


Figure 23.—Variation of Steady-State Inlet Boundary Layer Total Pressure Profiles and RMS Total Pressure Levels With Angle-of-Attack; Without Engine Interaction, $V_T = 147.7(273.5)$, $WKIA = 32.06(156.50)$

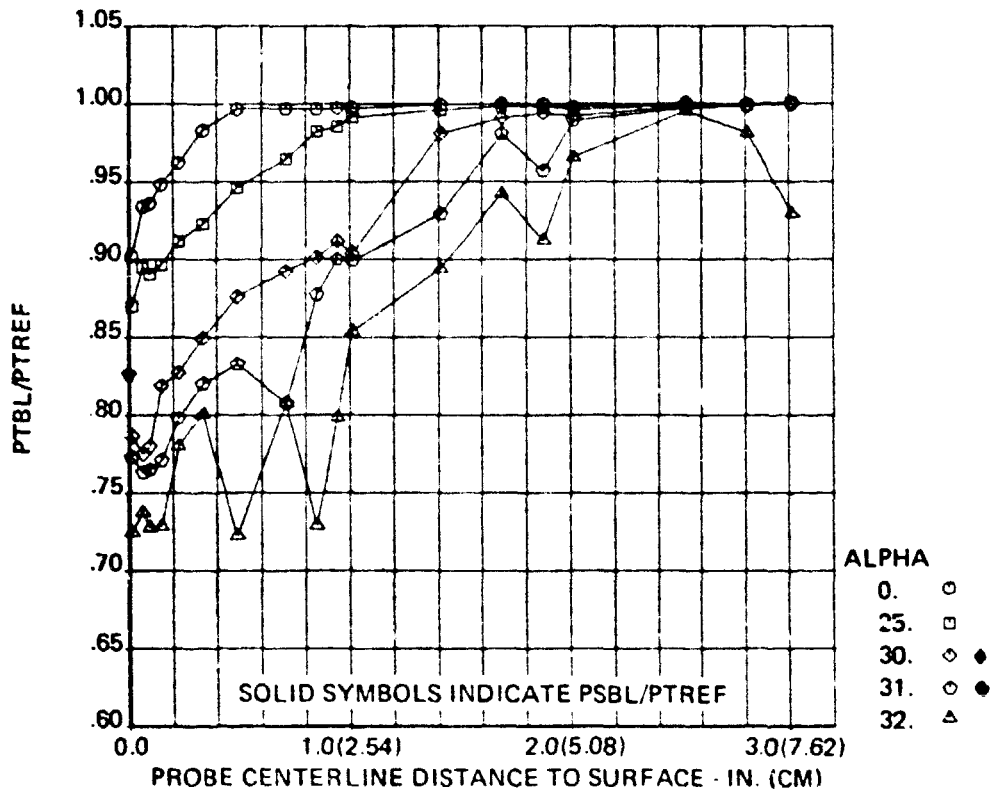


Figure 24.—Variation of Inlet Boundary Layer Total Pressure Profiles With Inlet Angle-of-Attack; With Engine Interaction, $V_T = 171.4(317.4)$, $\theta = 175^\circ$, $WKIA = 36.05(175.98)$

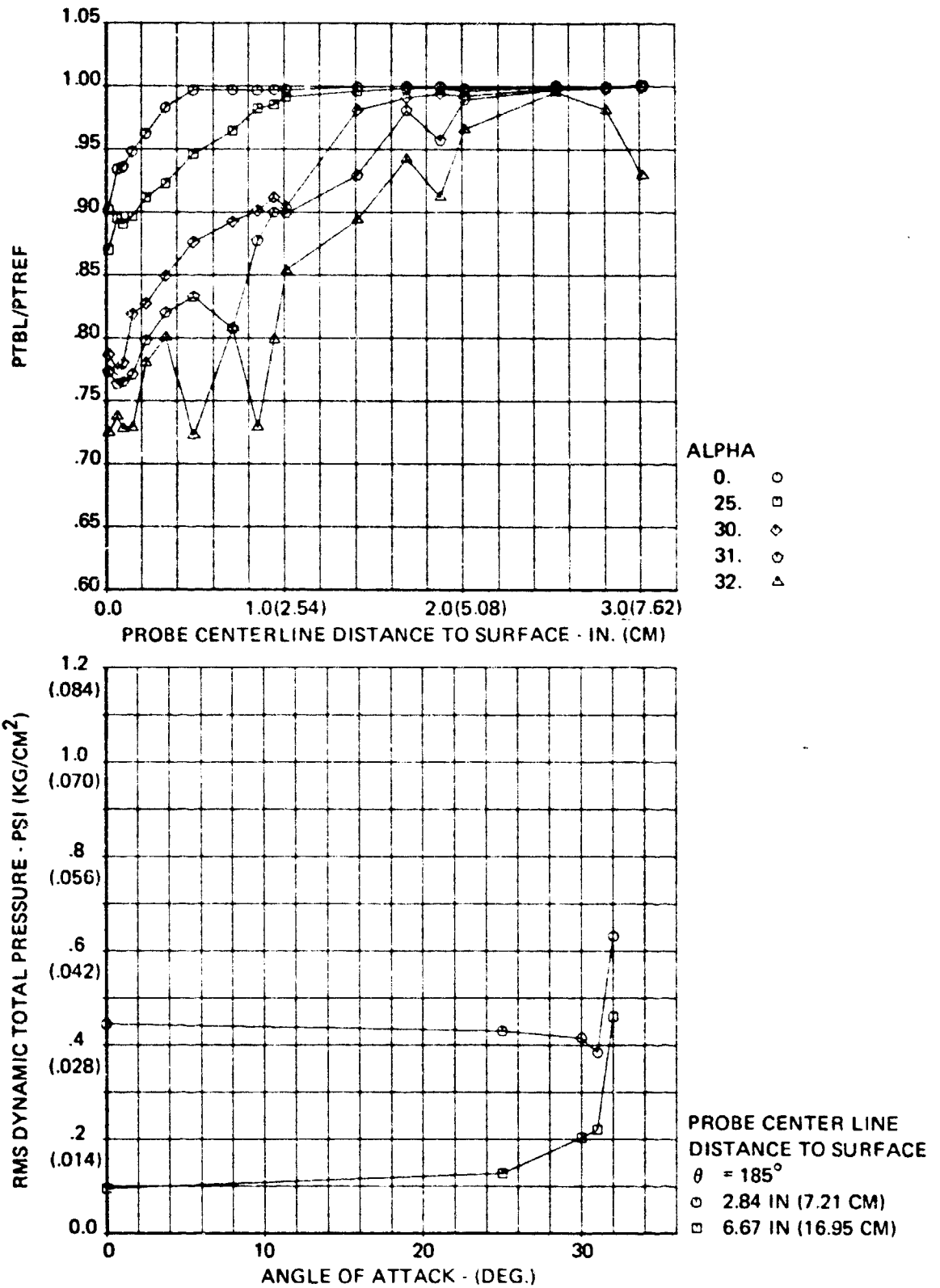


Figure 25. — Variation of Steady-State Inlet Boundary Layer Total Pressure Profiles and RMS Total Pressure Levels With Angle-of-Attack; With Engine Interaction, $V_T = 171.4(317.4)$, $WKIA = 36.05(175.98)$

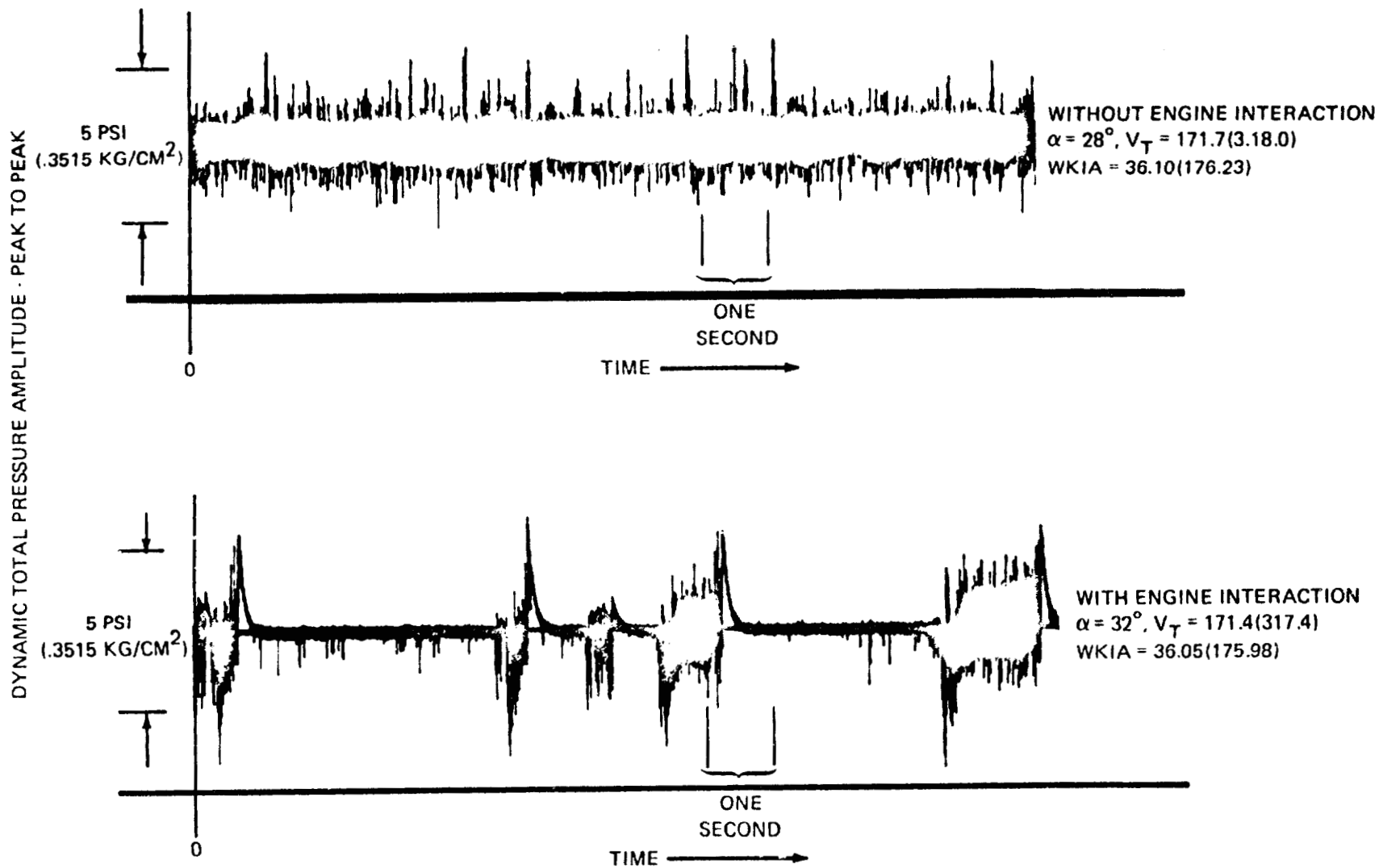


Figure 26.—Comparison of Dynamic Total Pressure Time Histories Measured by the
 Recovery Rake With and Without Engine Interaction, $\theta = 185^\circ$,
 Probe Radius = 19.16 in. (48.67 cm)

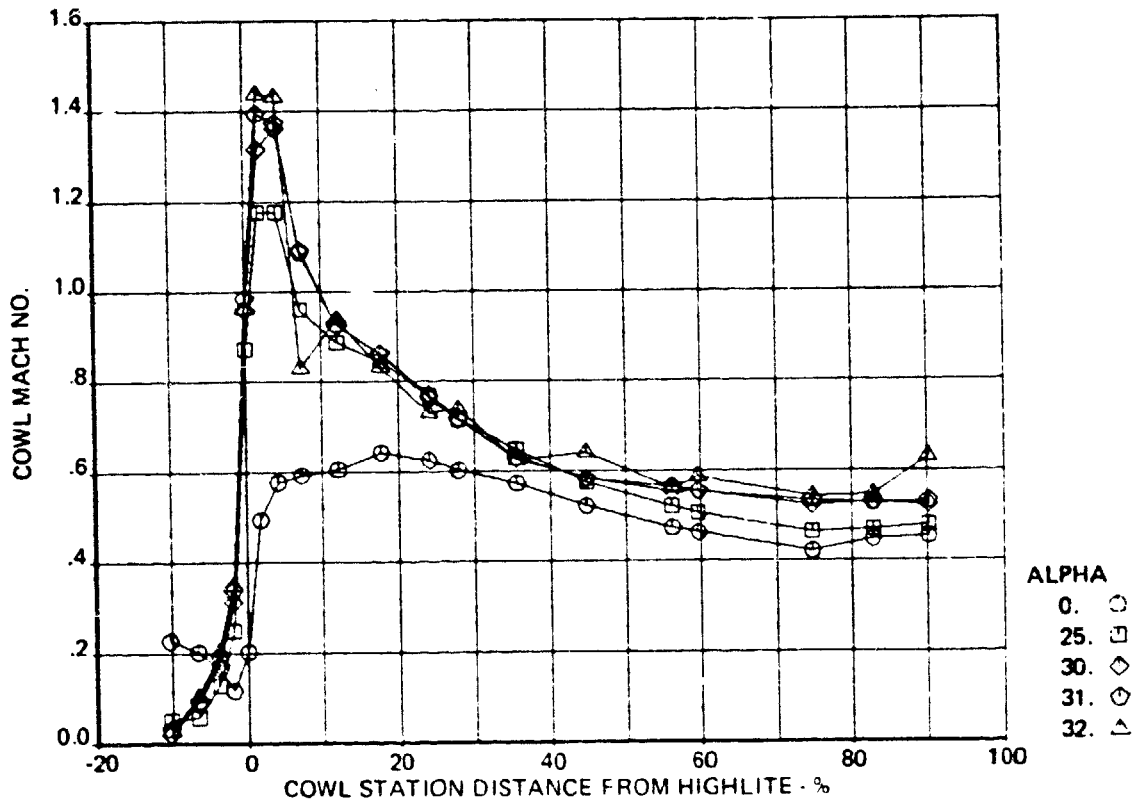


Figure 27.—Variation of Inlet Internal Mach Number Distribution With Inlet Angle-of-Attack; With Engine Interaction, $V_T = 171.4(317.4)$, $\theta = 180^\circ$, WKIA = 36.05(175.98)

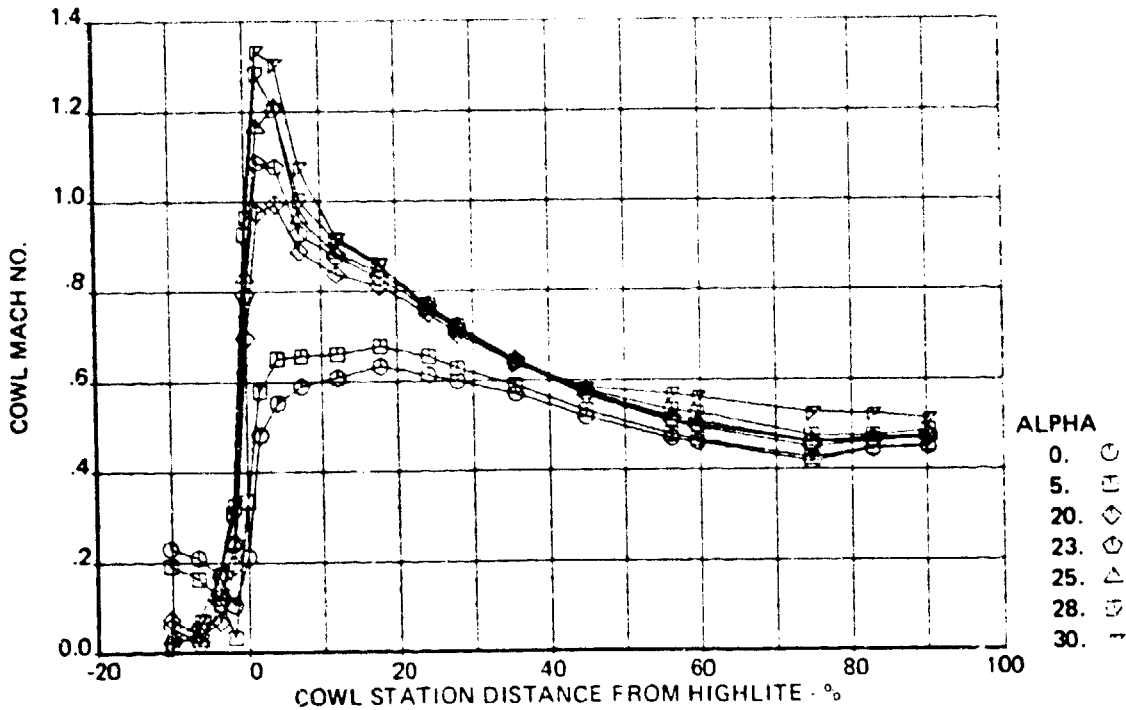


Figure 28.—Variation of Inlet Internal Mach Number Distribution With Inlet Angle-of-Attack; With Engine Interaction, $V_T = 171.7(317.4)$, $\theta = 180^\circ$, WKIA = 36.05(175.98)

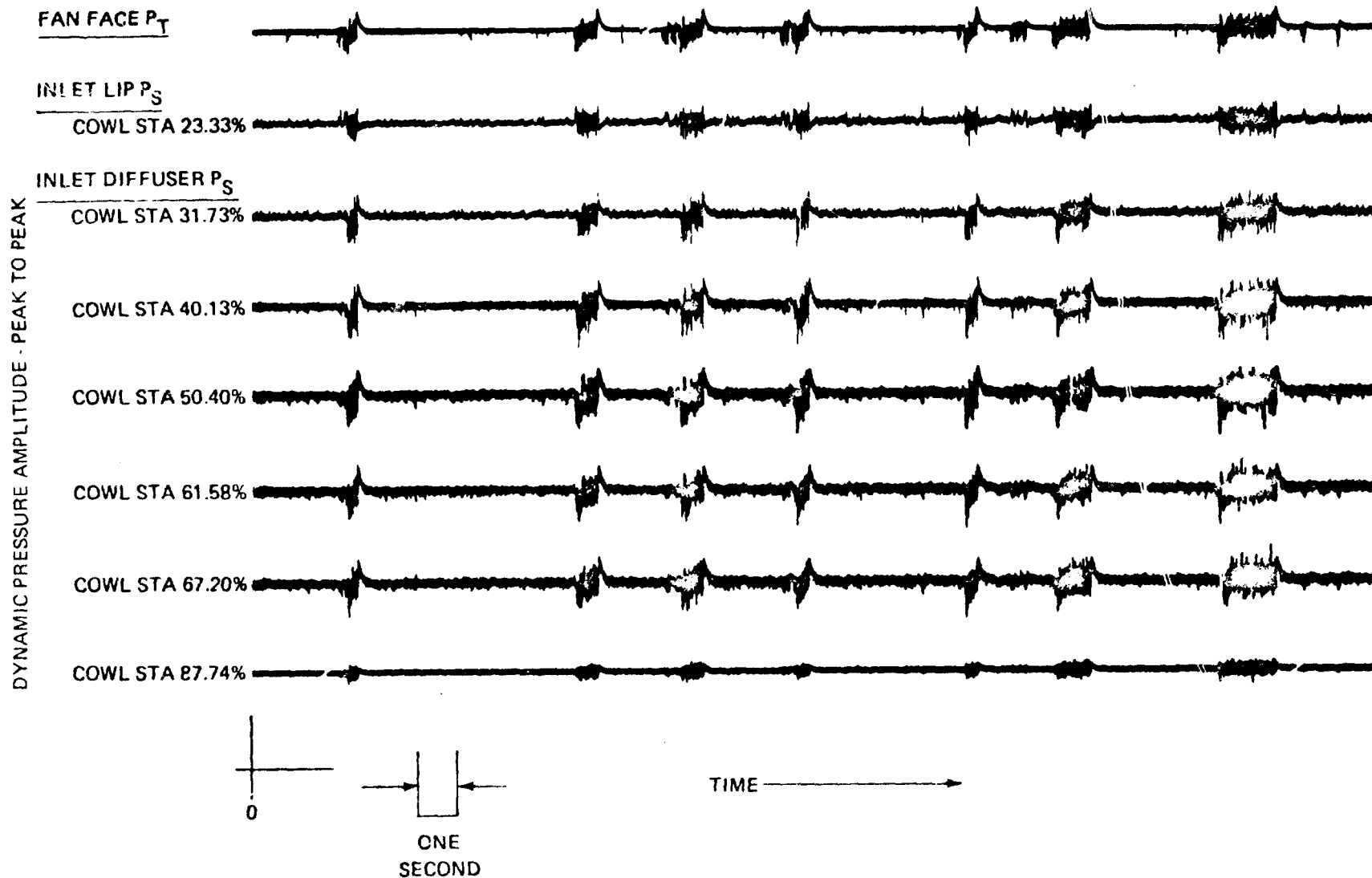
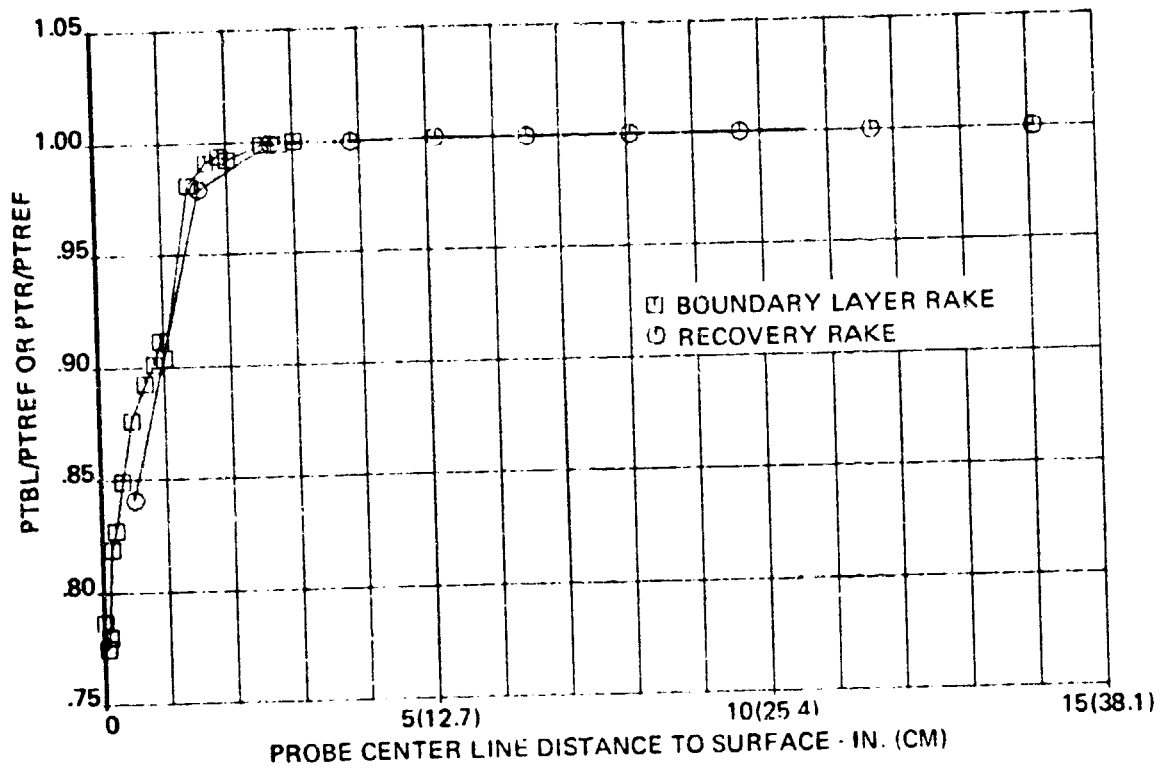
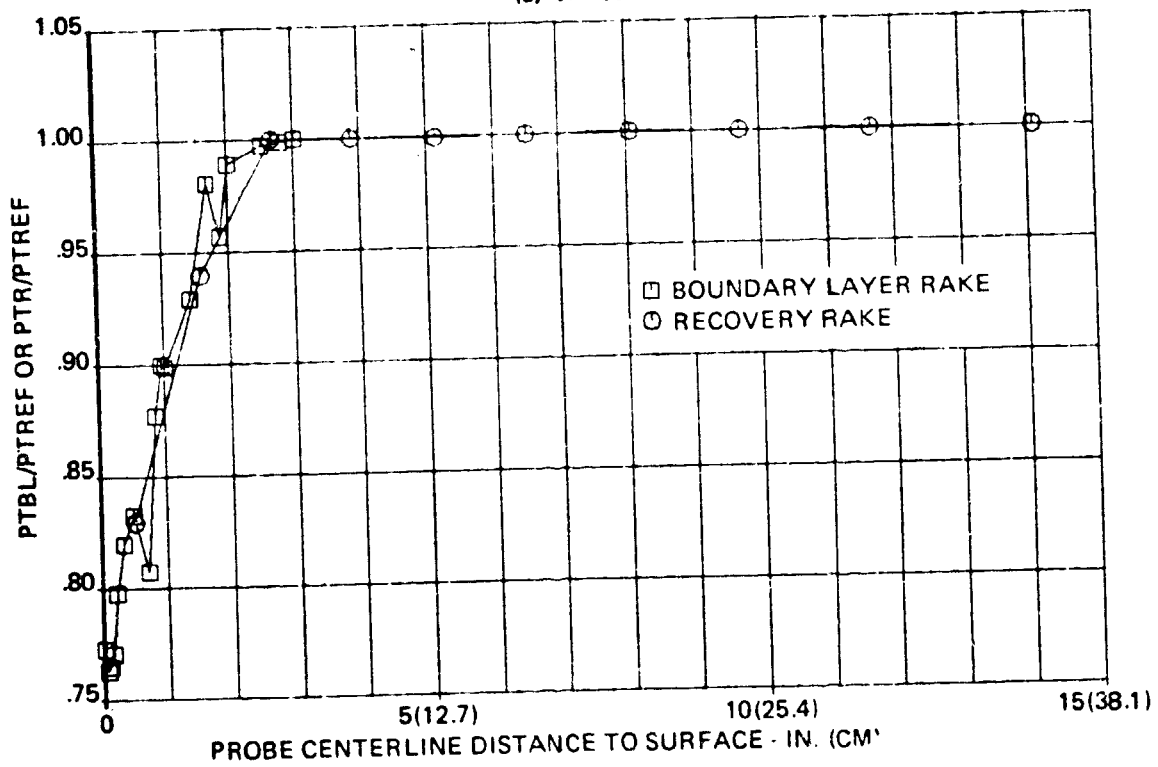


Figure 29.—Comparison of Dynamic Total and Static Pressure Time Histories From the Inlet Recovery Rake and the Inlet Internal Wall ($\theta = 180^\circ$); With Engine Interaction, $V_T = 171.4(317.4)$, $WKIA = 36.05(175.98)$, $\alpha = 32^\circ$



(a) $\alpha = 30^\circ$



(b) $\alpha = 31^\circ$

Figure 30.—Comparison of Inlet Total Pressure Profiles Measured by the Boundary Layer Rake and the Recovery Rake With the Inlet Separated; With Engine Interaction, $V_T = 171.4(317.4)$, $W_{KIA} = 36.05(175.98)$

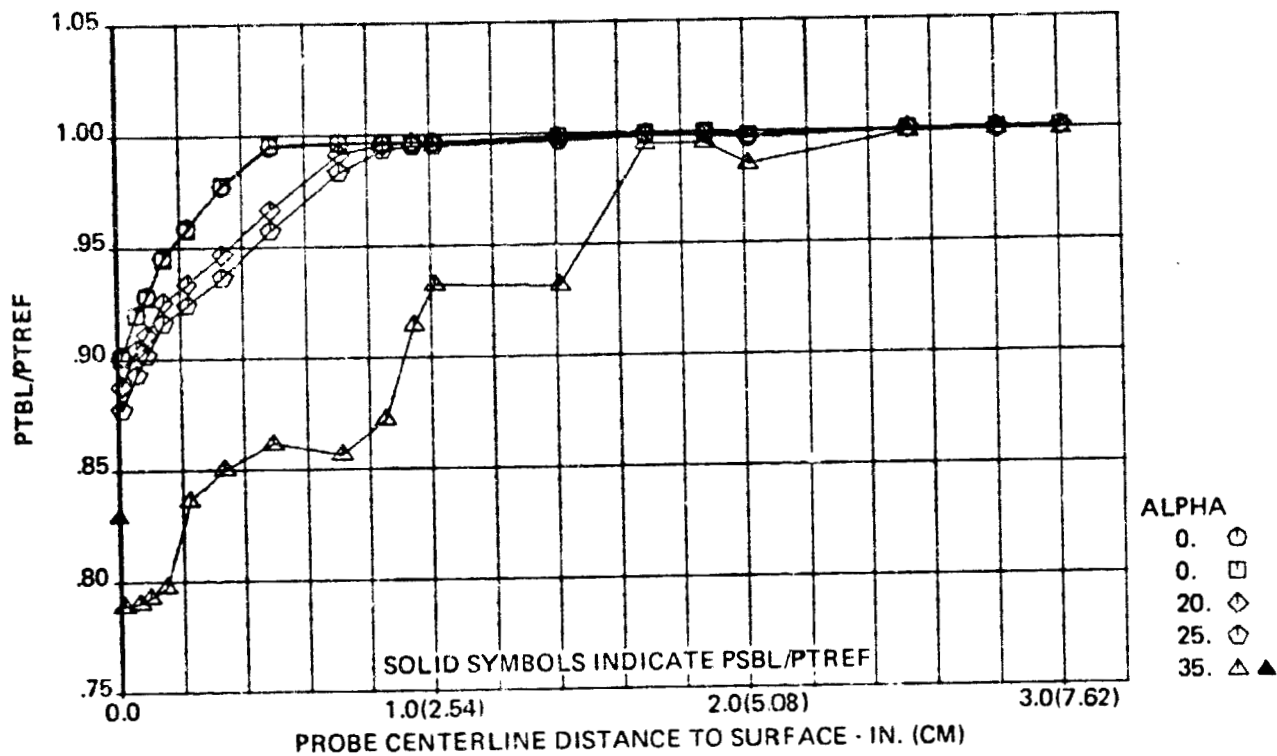


Figure 31.—Variation of Inlet Boundary Layer Total Pressure Profile With Inlet Angle-of-Attack; With Engine Interaction, $V_T = 147.4(273.5)$, $\theta = 175^\circ$, $WKIA = 36.05(175.98)$

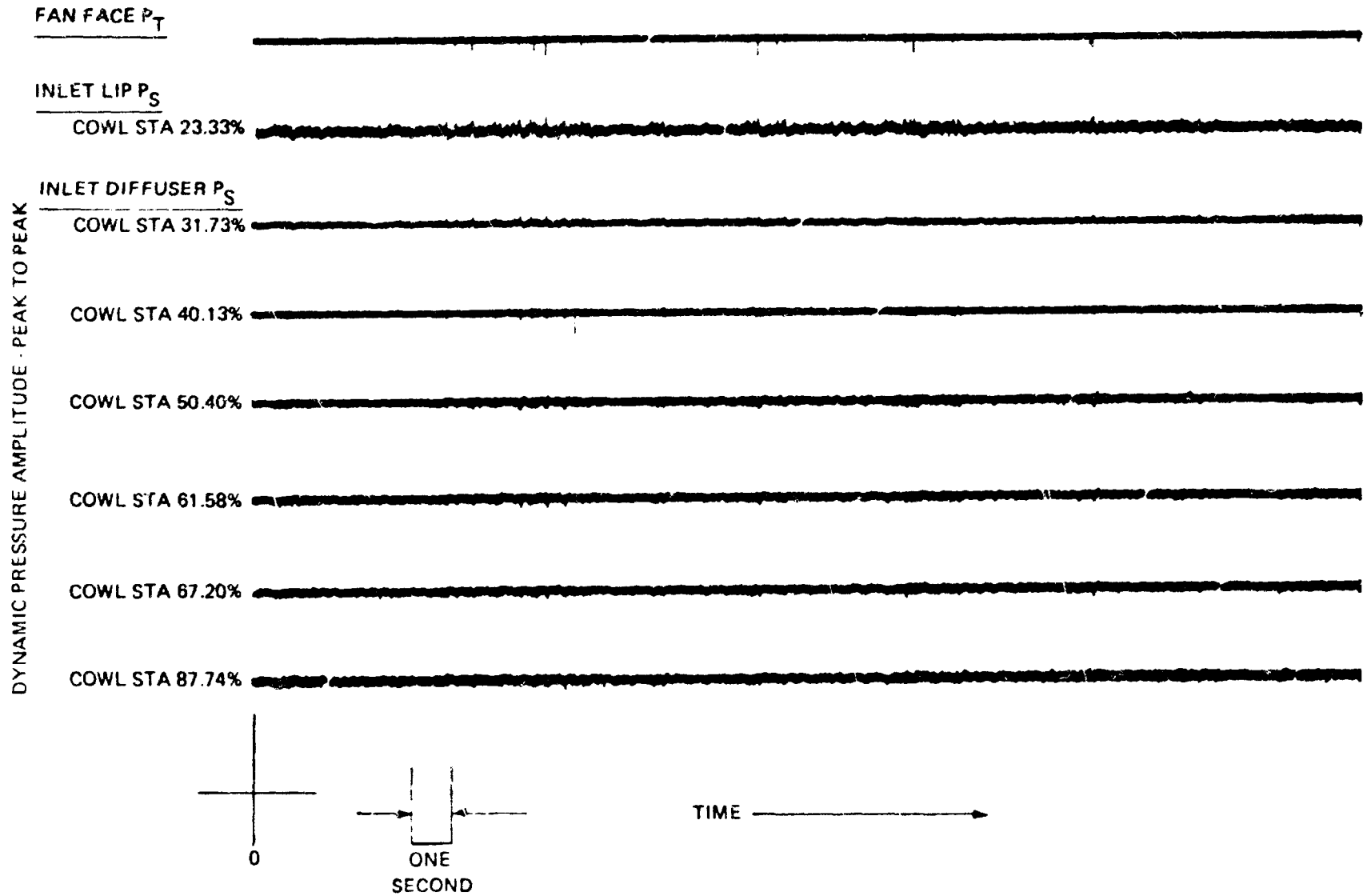


Figure 32.—Comparison of Dynamic Total and Static Pressure Time Histories From the Inlet Recovery Rake and the Inlet Internal Wall ($\theta = 180^\circ$); With Engine Interaction, $V_T = 174.4(273.5)$, $WKIA = 36.05(175.98)$, $\alpha = 35^\circ$

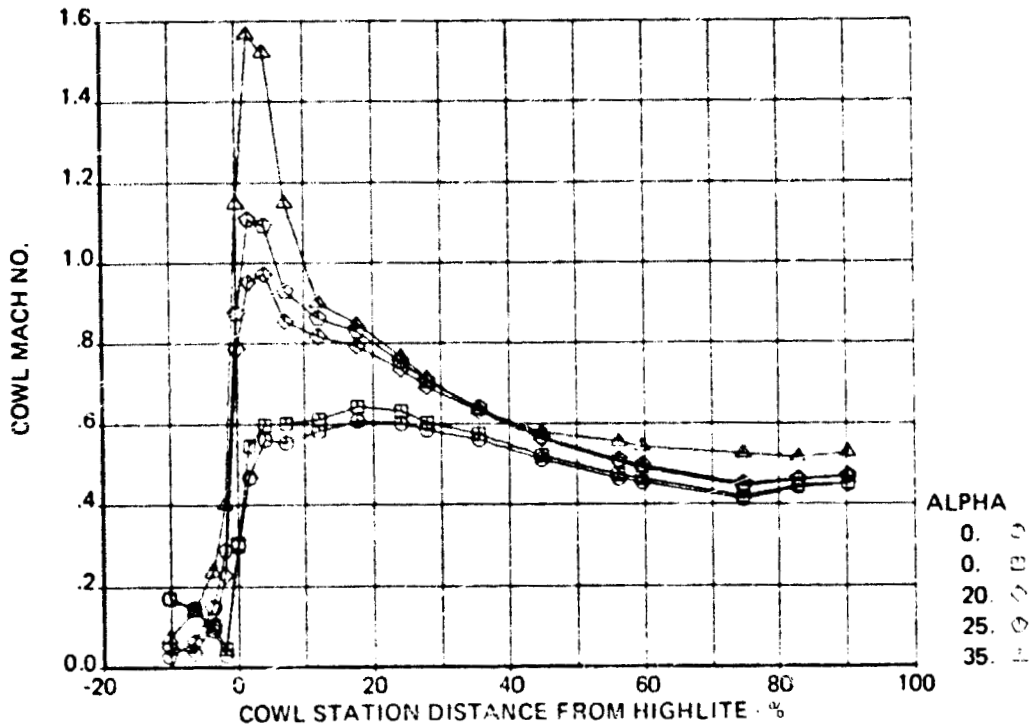


Figure 33.—Variation of Inlet Internal Mach Number Distribution With Inlet Angle-of-Attack; With Engine Interaction, $V_T = 174.4(273.5)$, $\theta = 180^\circ$, $WKIA = 36.05(175.98)$

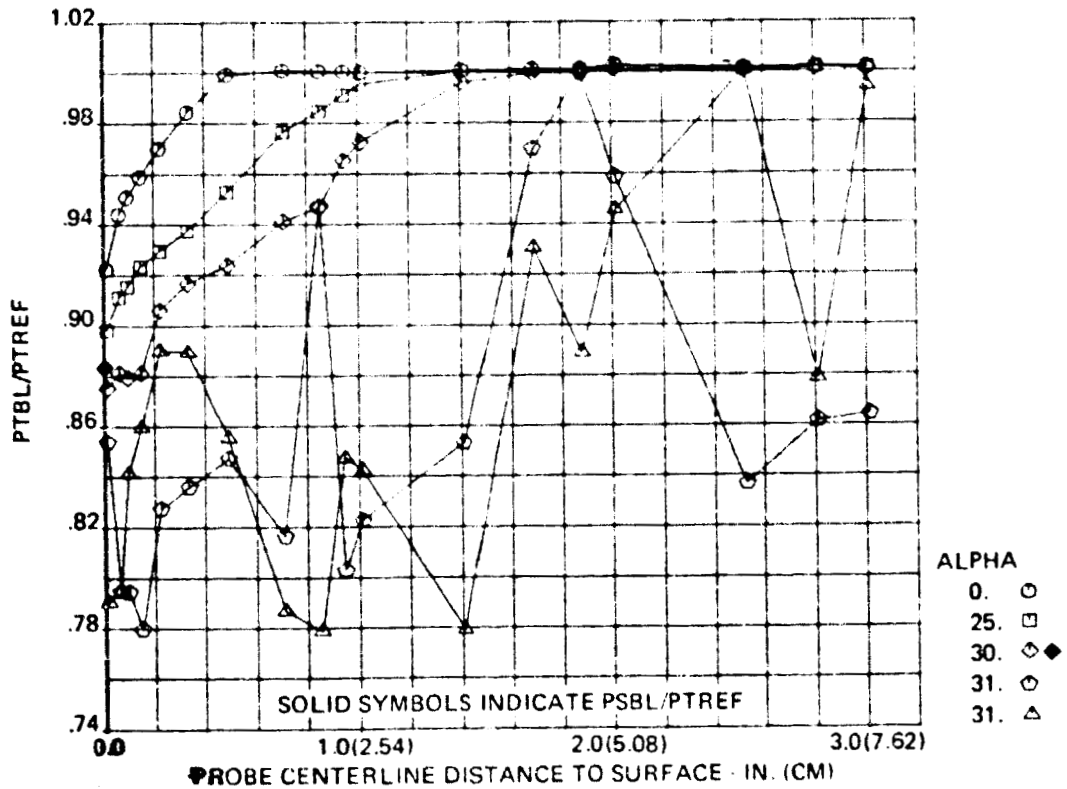


Figure 34.—Variation of Inlet Boundary Layer Total Pressure Profile With Inlet Angle-of-Attack; With Engine Interaction, $V_T = 147.2(273.5)$, $\theta = 175^\circ$, $WKIA = 32.11(156.75)$

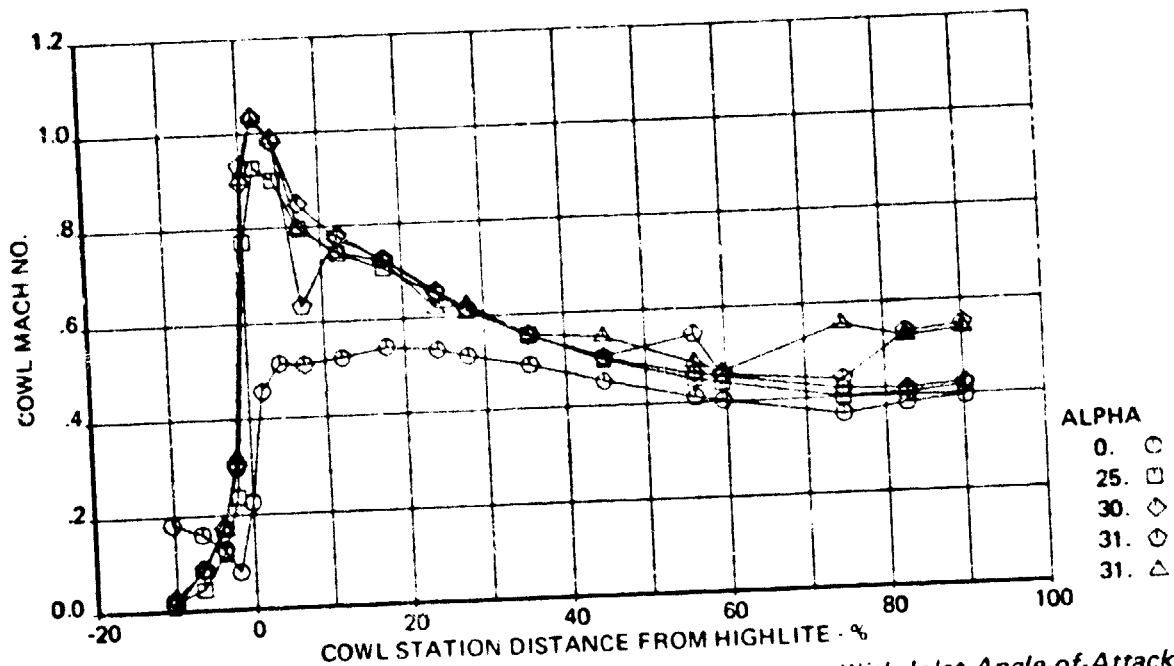


Figure 35.—Variation of Inlet Internal Mach Number Distribution With Inlet Angle-of-Attack; With Engine Interaction, $V_T = 147.2(273.5)$, $\theta = 180^\circ$, $WKIA = 32.11(156.75)$

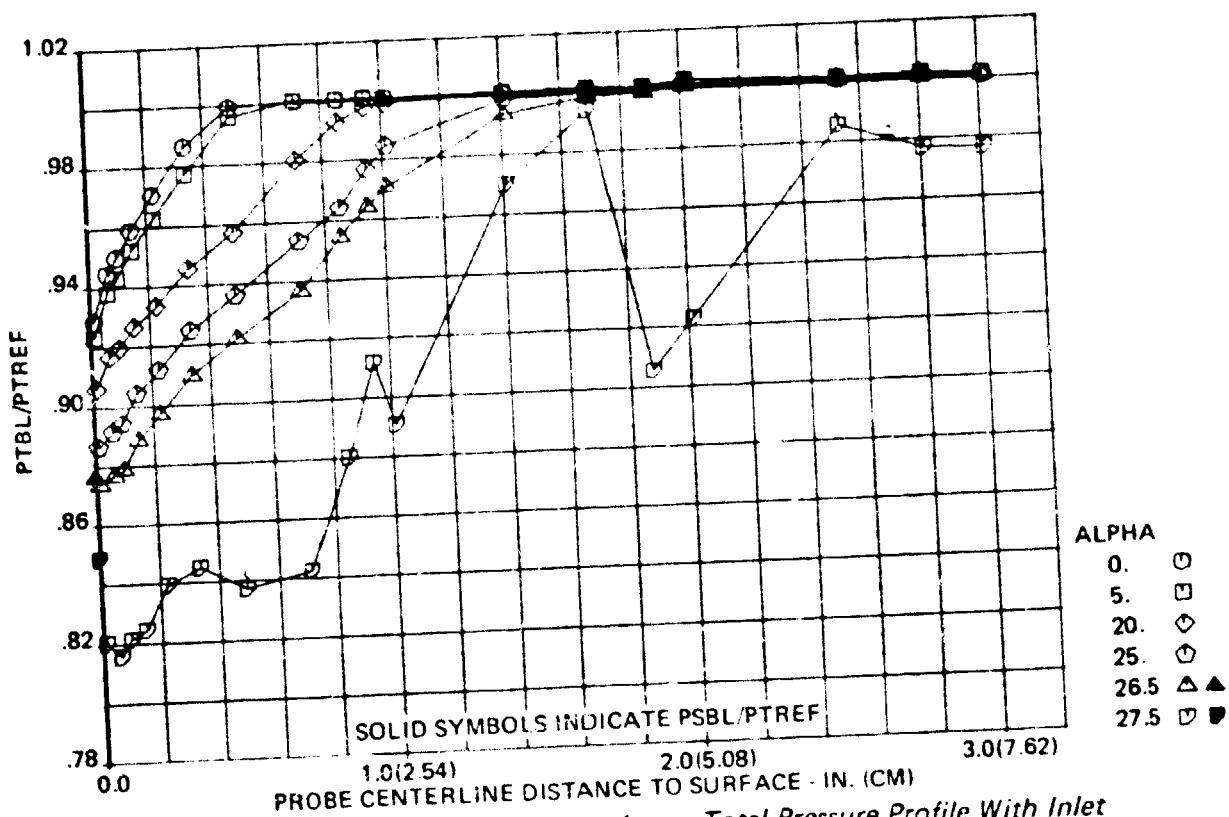


Figure 36.—Variation of Inlet Boundary Layer Total Pressure Profile With Inlet Angle-of-Attack; With Engine Interaction, $V_T = 186.0(344.5)$, $\theta = 175^\circ$, $WKIA = 32.15(156.94)$

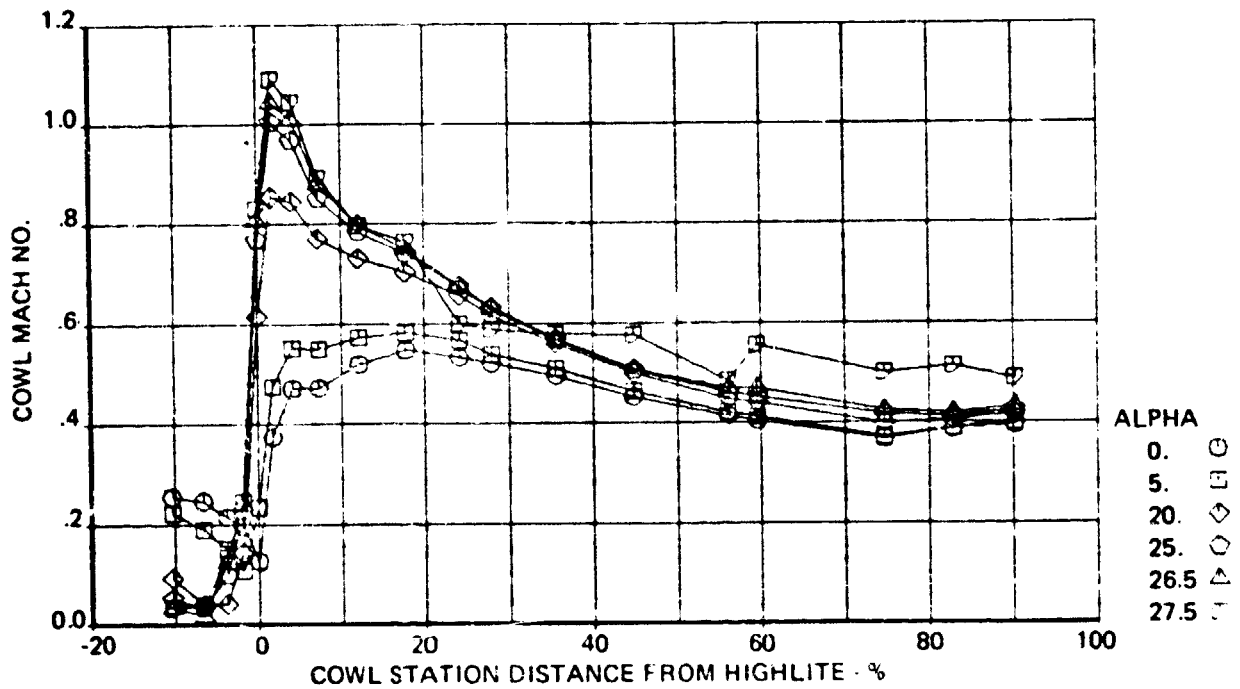


Figure 37. - Variation of Inlet Internal Mach Number Distribution With Inlet Angle-of-Attack; With Engine Interaction $V_T = 186.0(344.5)$, $\theta = 180^\circ$, $WKIA = 32.15(156.94)$

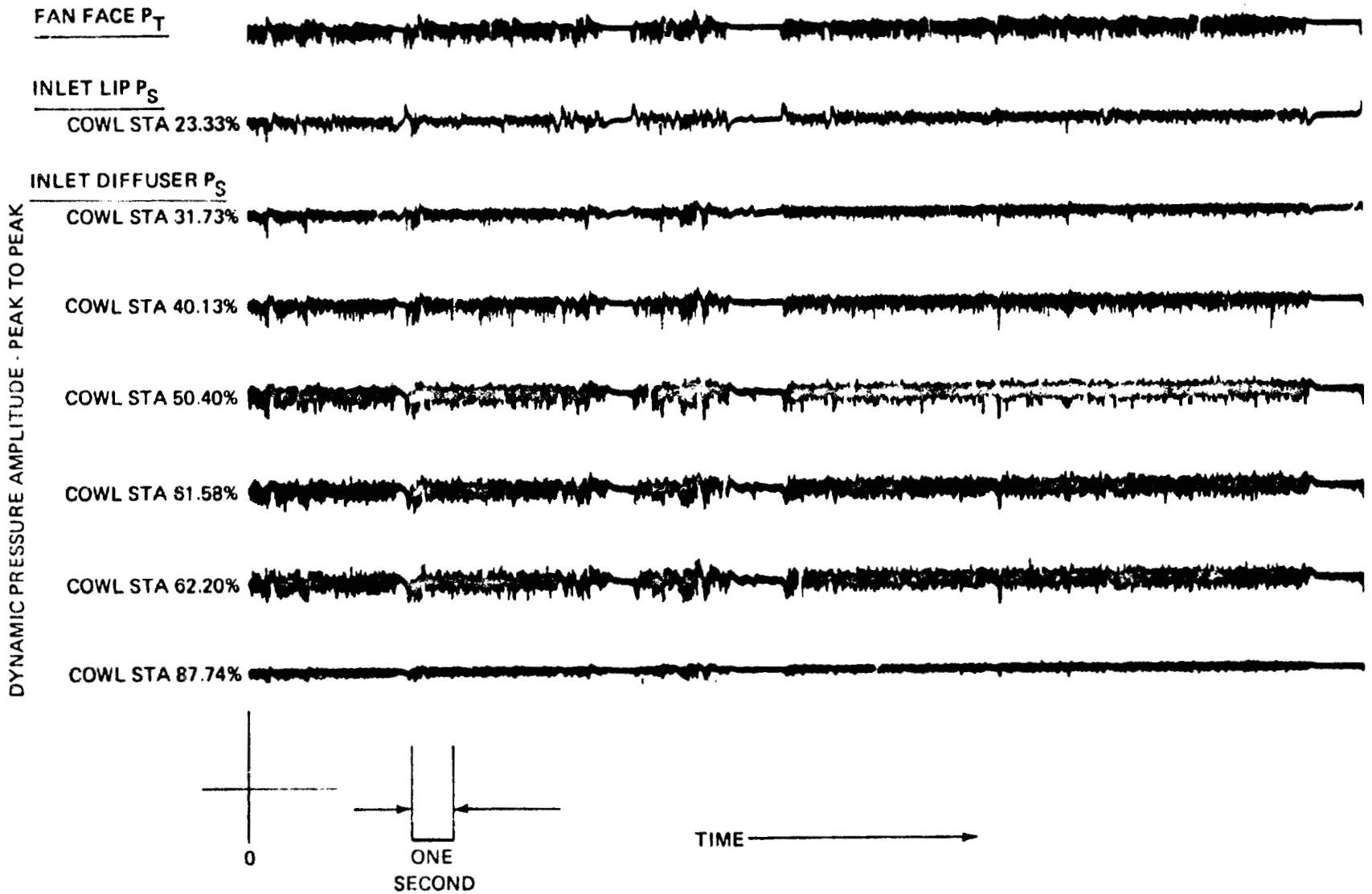


Figure 38.—Comparison of Dynamic Total and Static Pressure Time Histories From the Inlet Recovery Rake and the Inlet Internal Wall ($\theta = 180^\circ$): With Engine Interaction, $V_T = 186.2(344.8)$, $WKIA = 32.04(156.4)1$, $\alpha = 27.5^\circ$

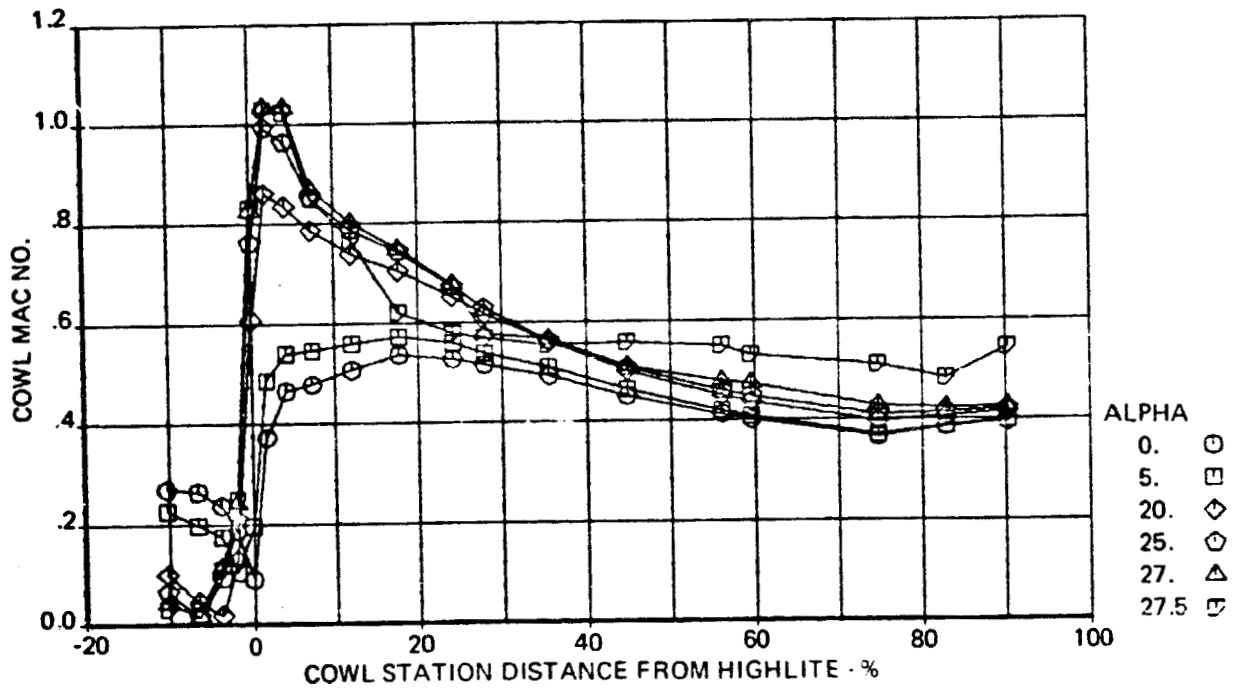


Figure 39.—Variation of Internal Mach Number Distribution With Inlet Angle-of-Attack; With Engine Interaction, $V_T = 186.2(344.8)$, $\theta = 180^\circ$, $WKIA = 32.04(156.41)$

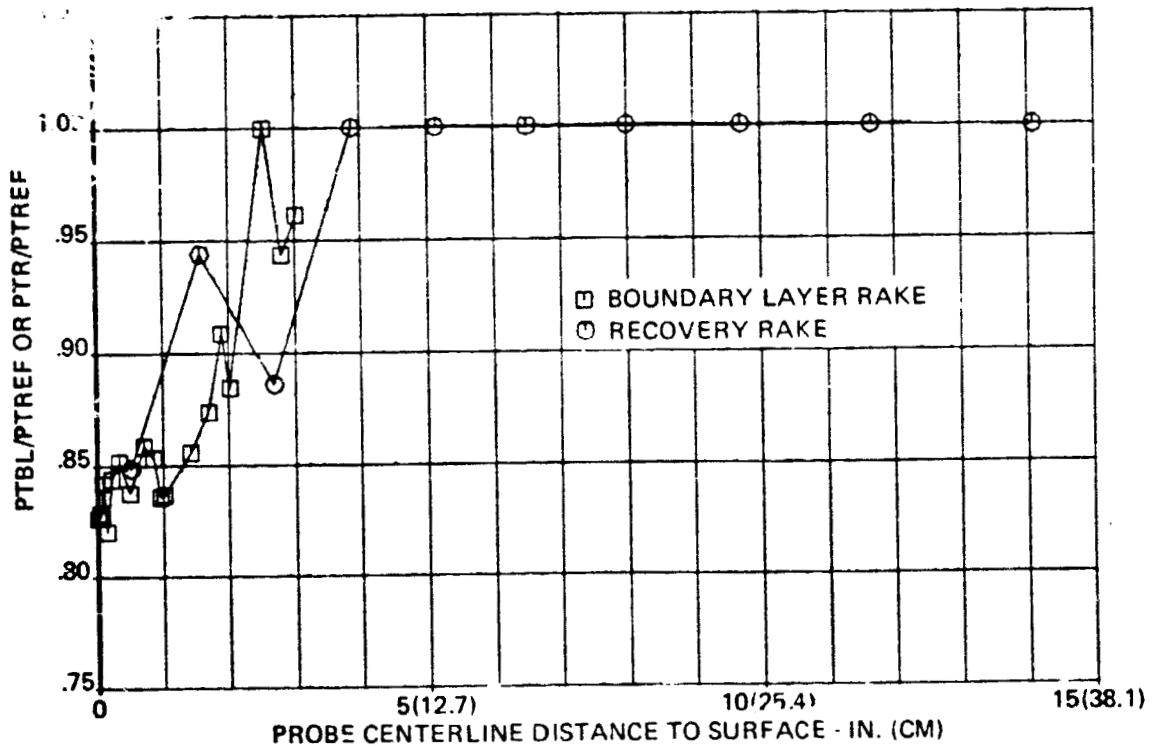


Figure 40.—Comparison of Inlet Total Pressure Profiles Measured by the Boundary Layer Rake and the Recovery Rake With the Inlet Separated; With Engine Interaction, $V_T = 186.2(344.8)$, $WKIA = 32.04(156.41)$, $\alpha = 27.5^\circ$

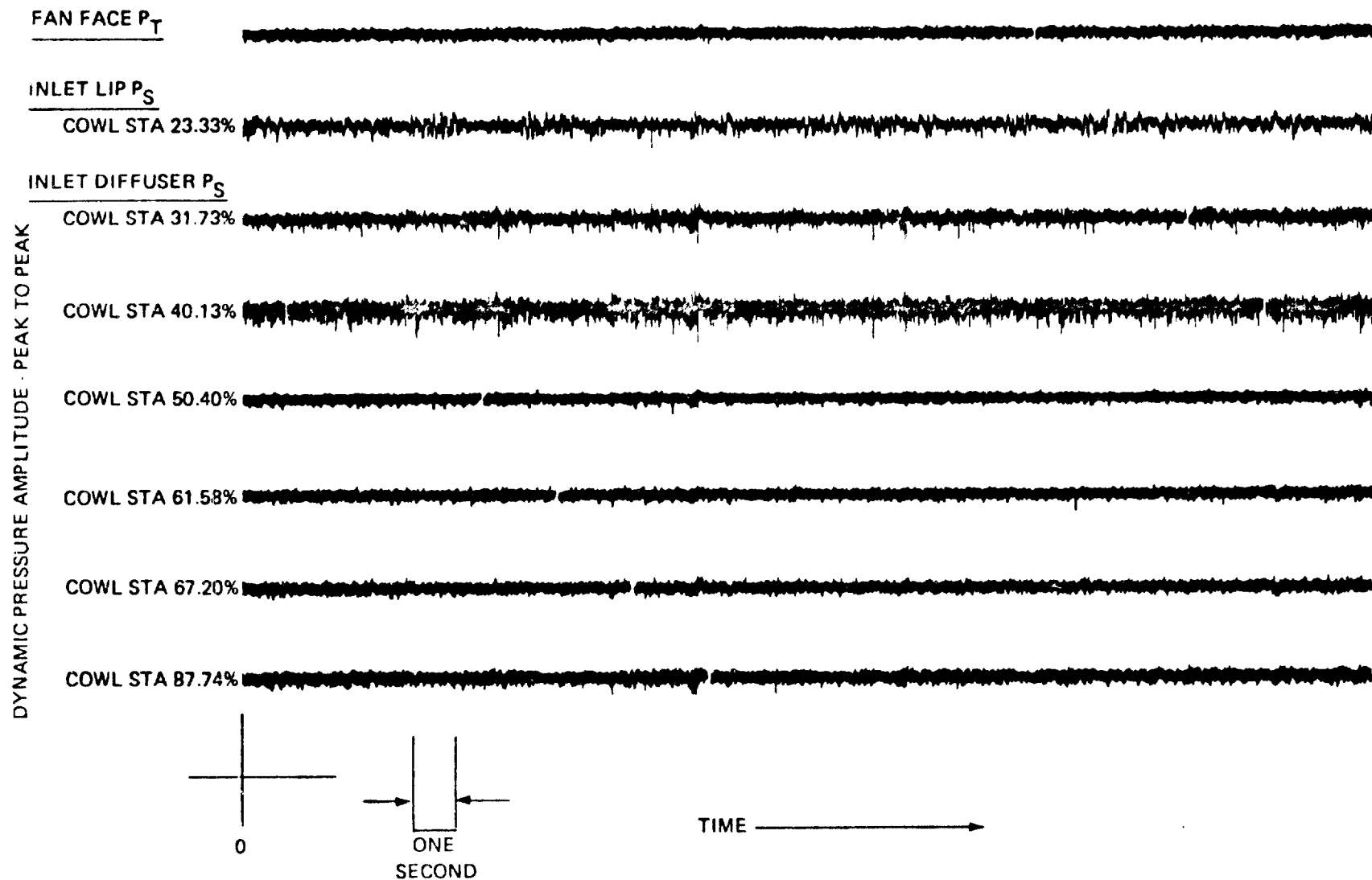


Figure 41.—Comparison of Dynamic Total and Static Pressure Time Histories From the Inlet Recovery Rake and the Inlet Internal Wall ($\theta = 180^\circ$); With Engine Interaction, $V_T = 171.5(317.6)$, $WKIA = 22.26(108.66)$, $\alpha = 27^\circ$

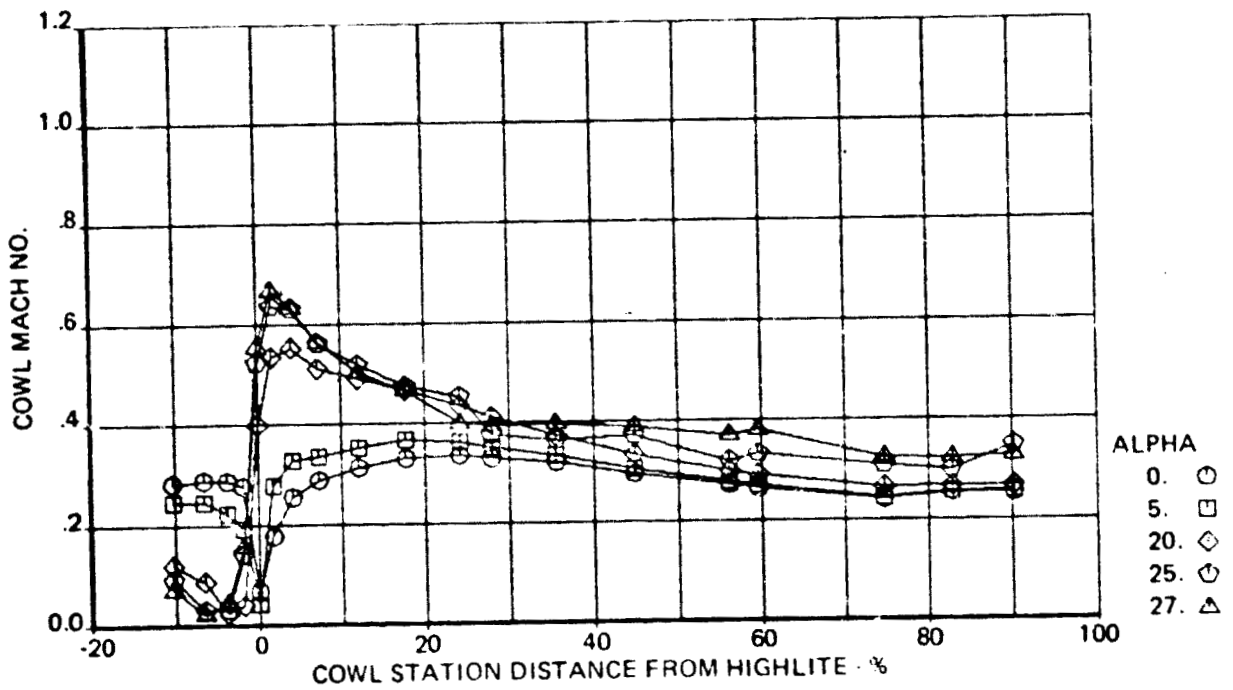


Figure 42.—Variation of Internal Mach Number Distribution With Inlet Angle-of-Attack; With Engine Interaction, $V_T = 171.5(317.6)$, $\theta = 180^\circ$, $WKIA = 22.26(108.66)$

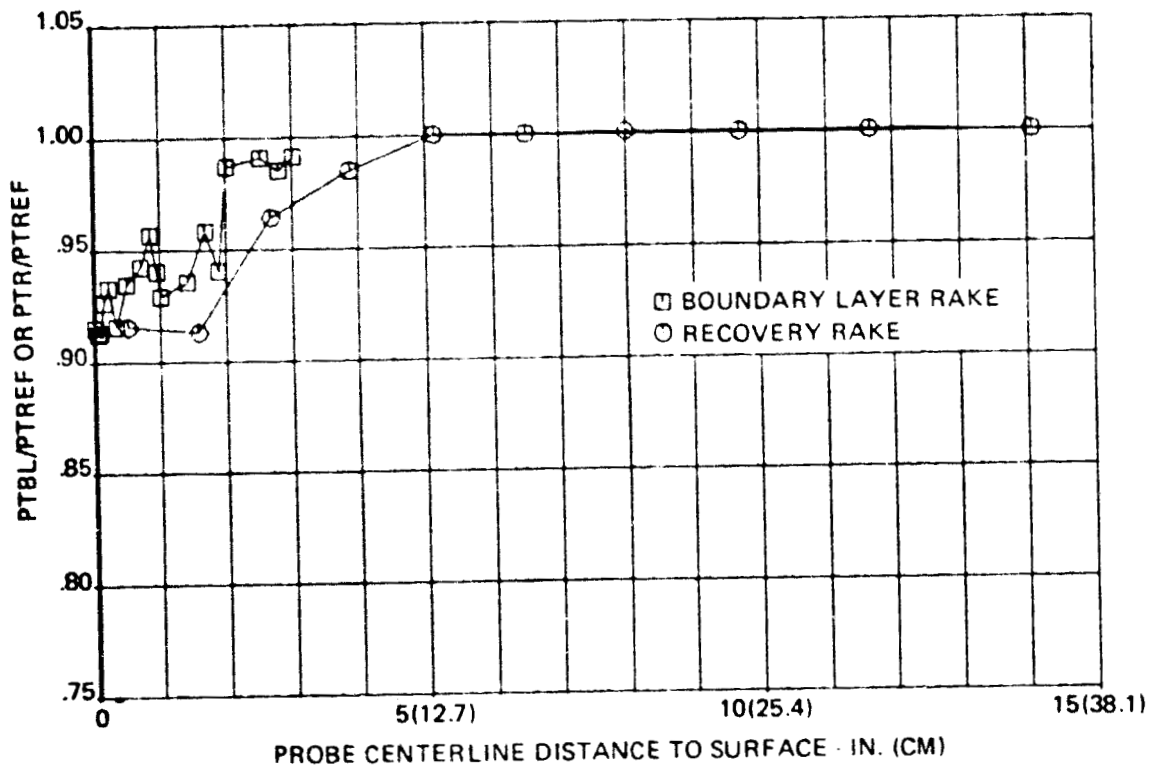


Figure 43.—Comparison of Inlet Total Pressure Profiles Measured by the Boundary Layer Rake and the Recovery Rake With the Inlet Separated; With Engine Interaction, $V_T = 171.5(317.6)$, $WKIA = 22.26(108.66)$, $\alpha = 27^\circ$

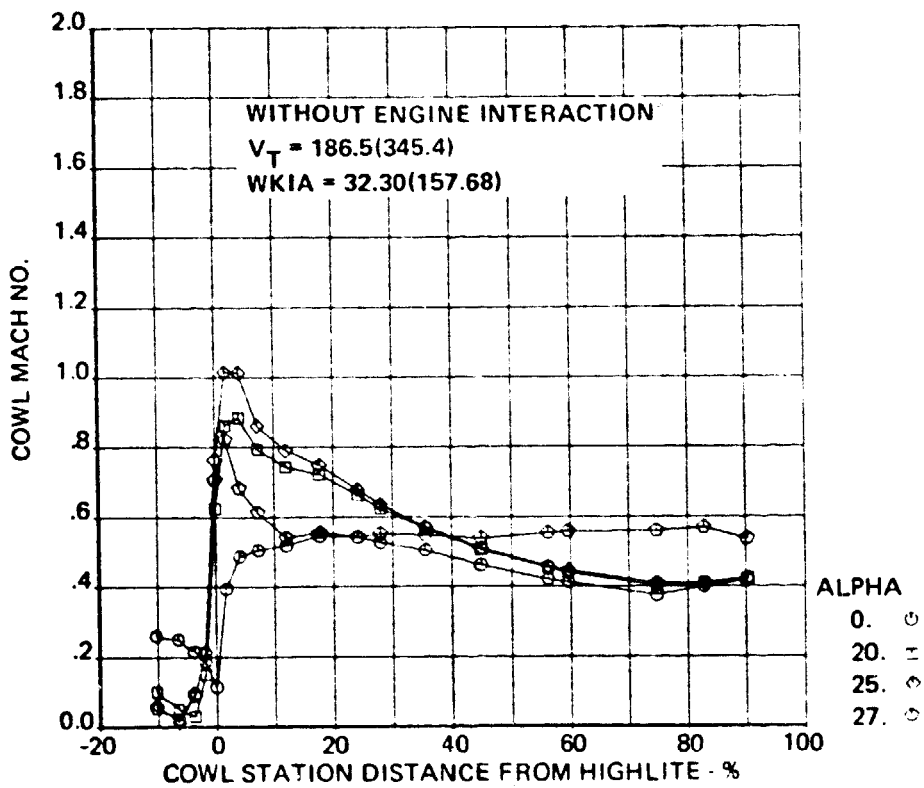
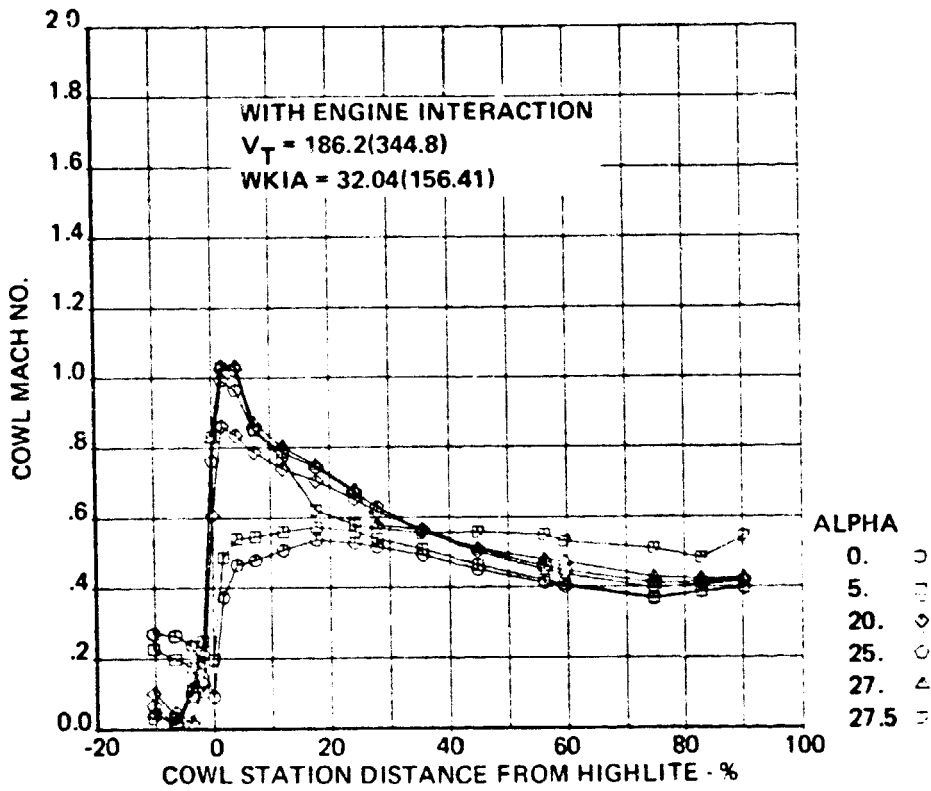


Figure 44.—Comparison of the Axial Location of Boundary Layer Separation With and Without Engine Interaction Determined From Cowl Mach Number Distributions, $\theta = 180^\circ$

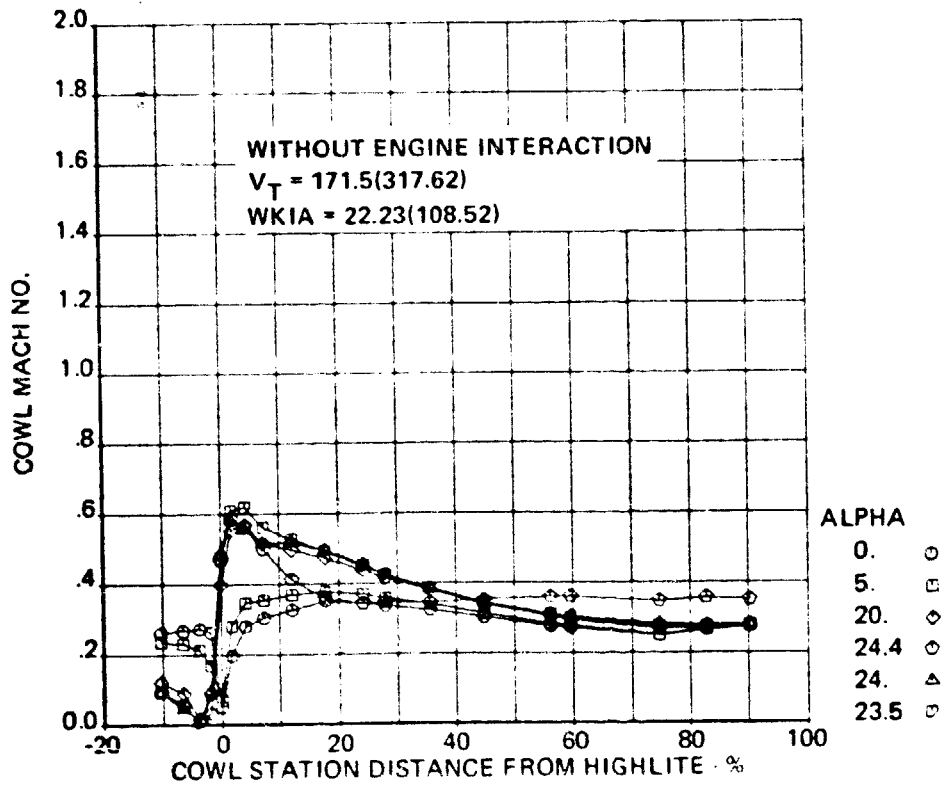
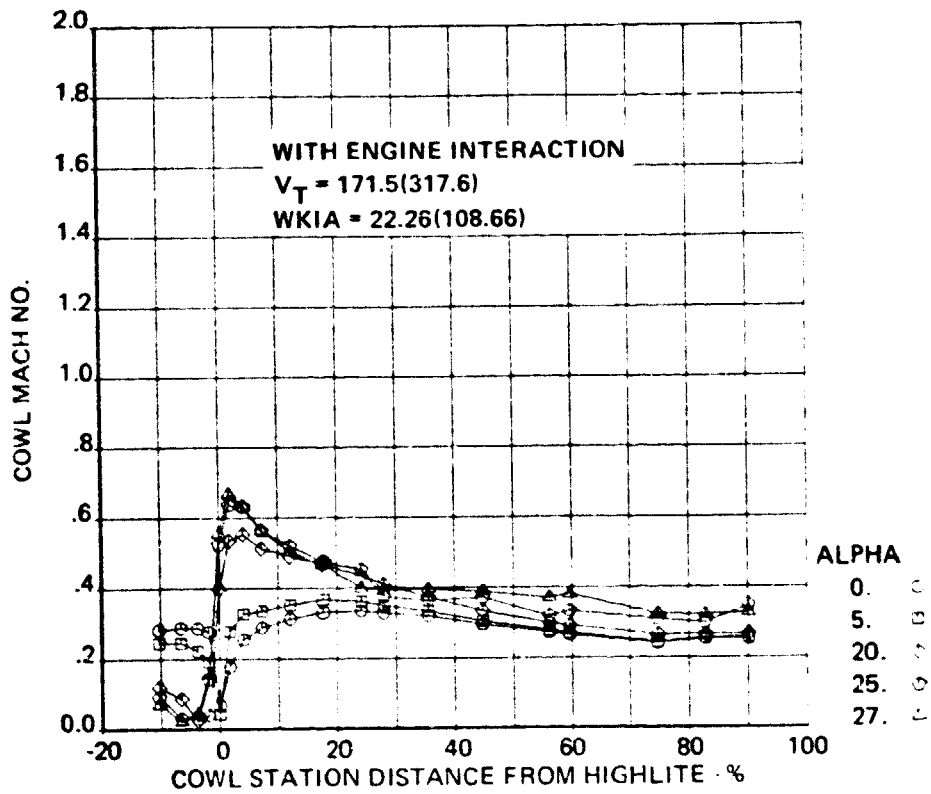
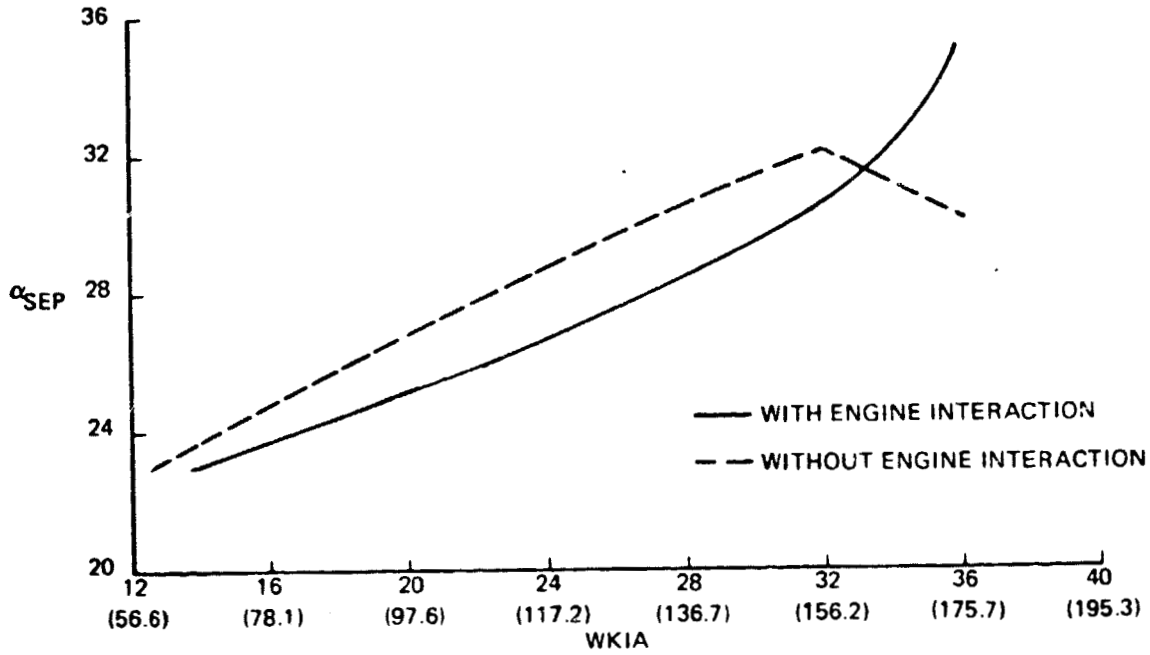
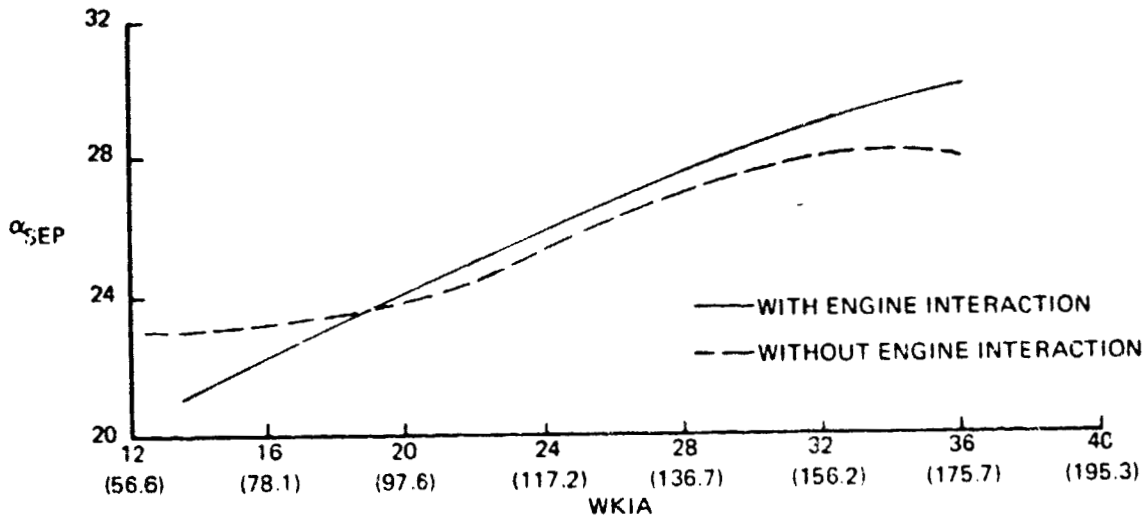


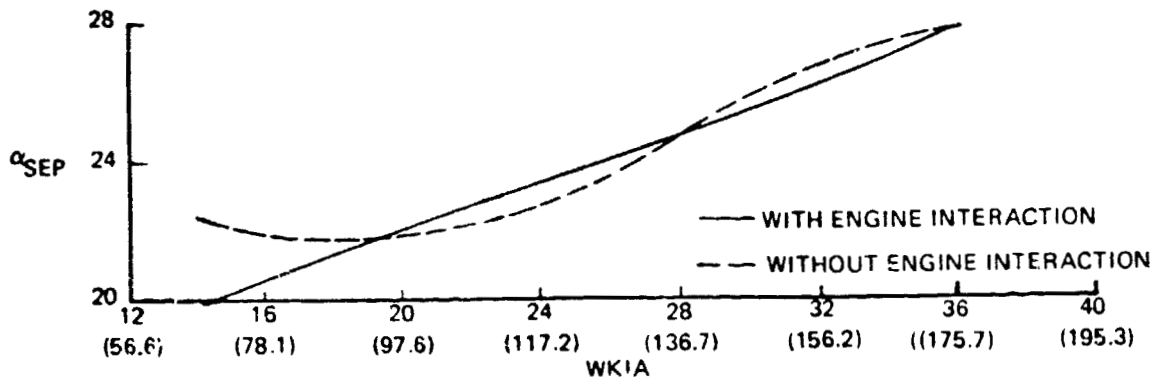
Figure 45.—Comparison of the Axial Location of Boundary Layer Separation With and Without Engine Interaction Determined From Cowl Mach Number Distribution, $\theta = 180^\circ$



(a) $V_T = 147$ (272.2)



(b) $V_T = 172$ (318.5)



(c) $V_T = 186$ (344.5)

Figure 46.—Comparison of Inlet Separation Boundaries With and Without Engine Interaction

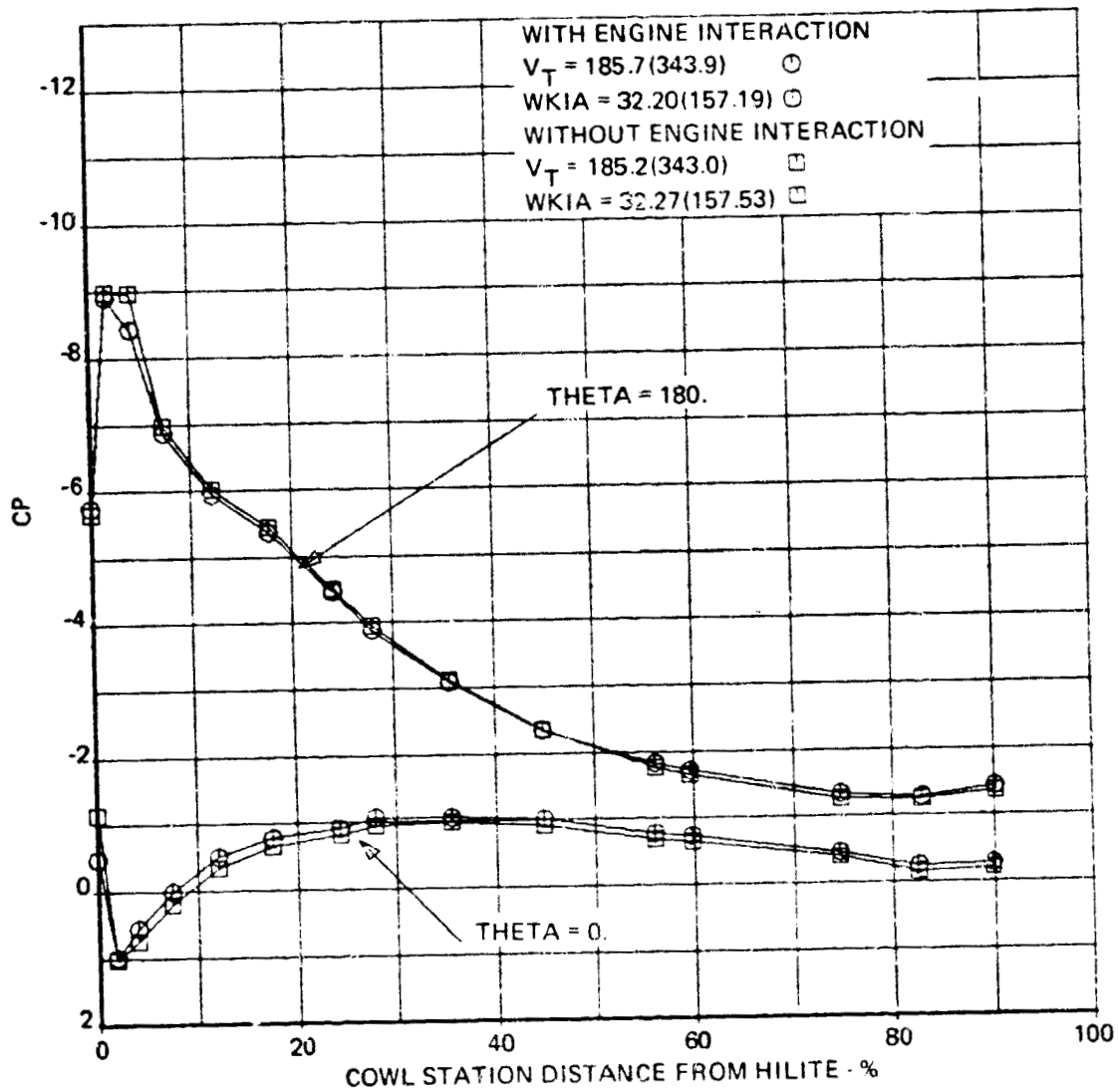
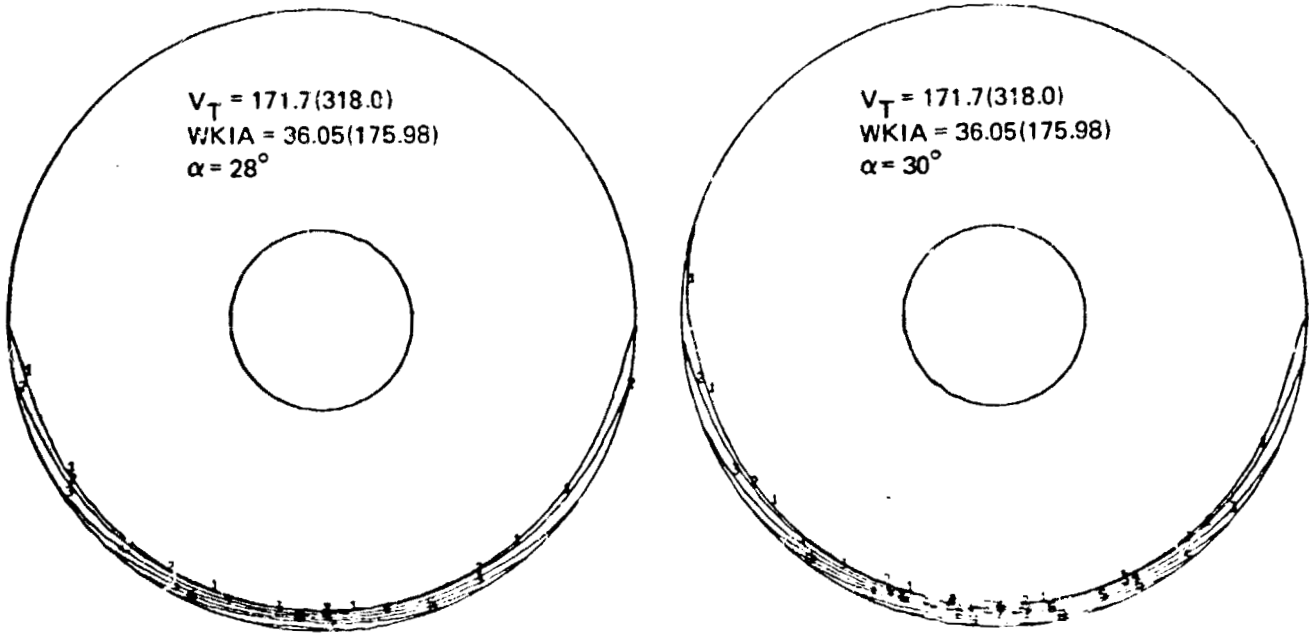


Figure 47.—Comparison of Inlet Internal Static Pressure Distribution With and Without Engine Interaction, $\alpha = 25^\circ$

WITH ENGINE INTERACTION



WITHOUT ENGINE INTERACTION

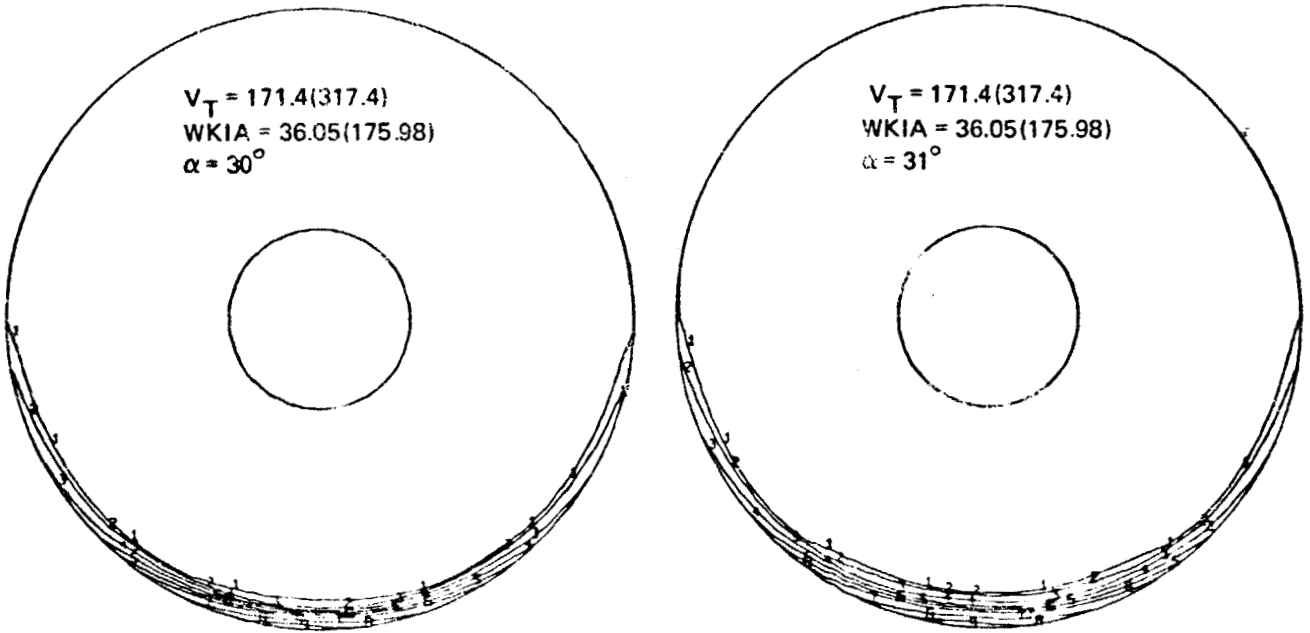
PTR/PTREF

- 1 0.9900
- 2 0.9800
- 3 0.9600
- 4 0.9400
- 5 0.9200
- 6 0.9000
- 7 0.8600
- 8 0.8200
- 9 0.7800
- 0 0.7400



Figure 48.—Comparison of Fan Face Total Pressure Recovery Maps With and Without Engine Interaction

WITH ENGINE INTERACTION



WITHOUT ENGINE INTERACTION

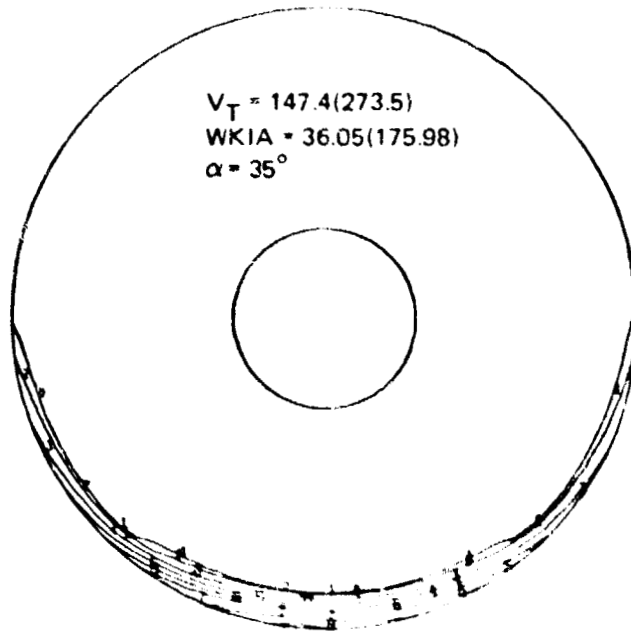
PTR/PTREF

- 1 0.9900
- 2 0.9800
- 3 0.9600
- 4 0.9400
- 5 0.9200
- 6 0.9000
- 7 0.8600
- 8 0.8200
- 9 0.7800
- 0 0.7400



Figure 49.—Comparison of Fan Face Total Pressure Recovery Maps With and Without Engine Interaction

WITH ENGINE INTERACTION



WITHOUT ENGINE INTERACTION

PTR/PTREF

- 1 0.9900
- 2 0.9800
- 3 0.9600
- 4 0.9400
- 5 0.9200
- 6 0.9000
- 7 0.8600
- 8 0.8200
- 9 0.7800
- 0 0.7400

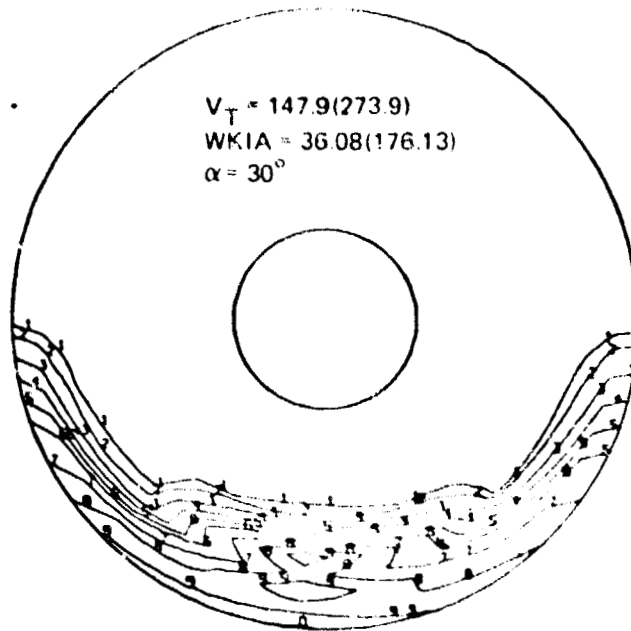
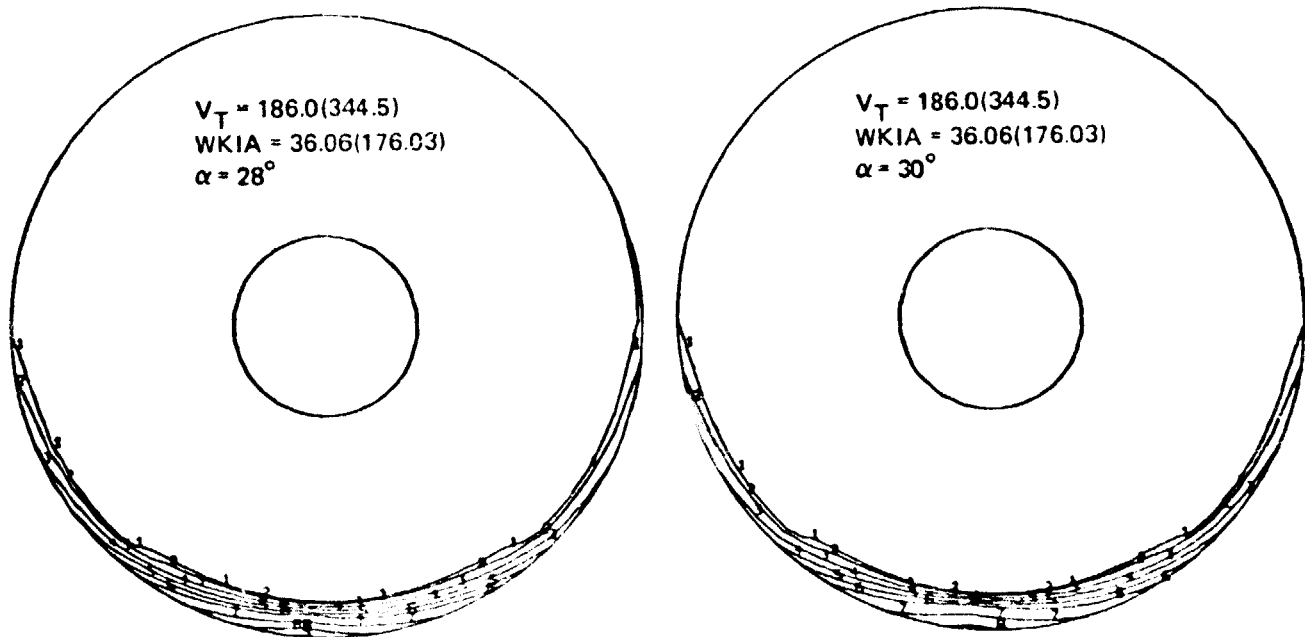


Figure 50.—Comparison of Fan Face Total Pressure Recovery Maps With and Without Engine Interaction

WITH ENGINE INTERACTION



WITHOUT ENGINE INTERACTION

PTR/PTREF	
1	0.9900
2	0.9800
3	0.9600
4	0.9400
5	0.9200
6	0.9000
7	0.8600
8	0.8200
9	0.7800
0	0.7400

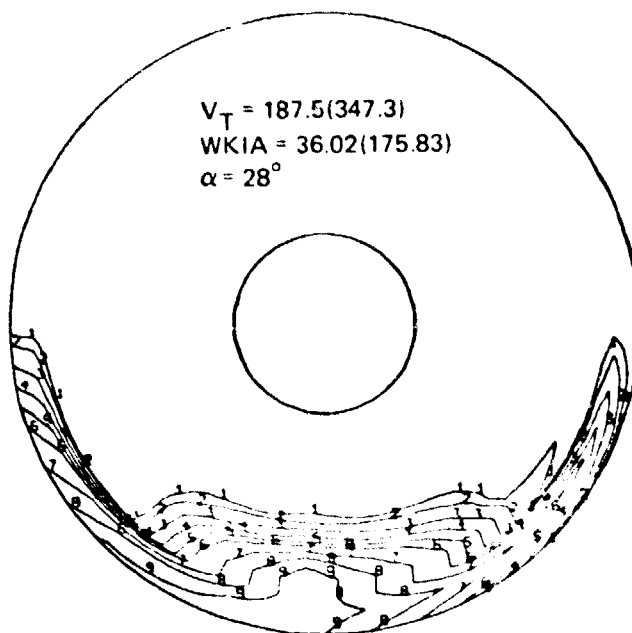


Figure 51.—Comparison of Fan Face Total Pressure Recovery Maps With and Without Engine Interaction

WITH ENGINE INTERACTION



WITHOUT ENGINE INTERACTION

PTR/PTREF

- 1 0.9900
- 2 0.9800
- 3 0.9600
- 4 0.9400
- 5 0.9200
- 6 0.9000
- 7 0.8600
- 8 0.8200
- 9 0.7800
- 0 0.7400

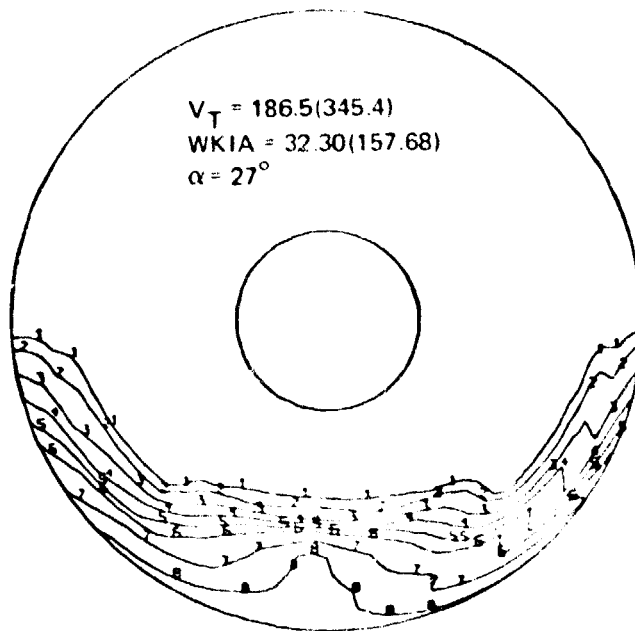
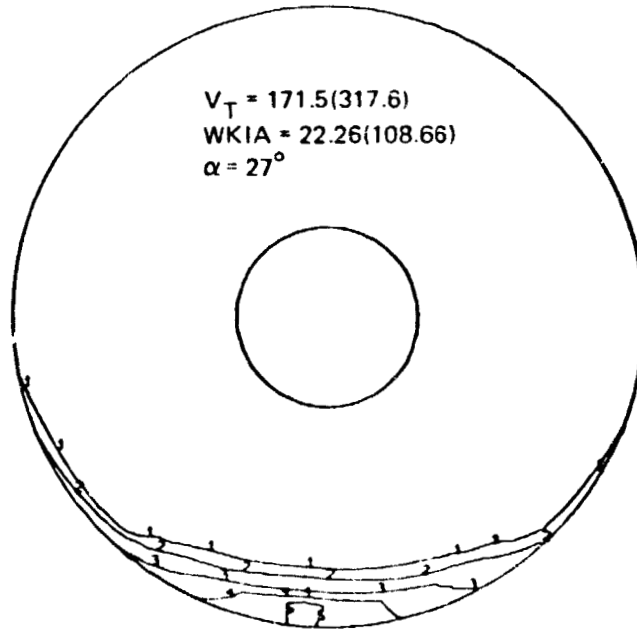


Figure 52.—Comparison of Fan Face Total Pressure Recovery Maps With and Without Engine Interaction

WITH ENGINE INTERACTION



WITHOUT ENGINE INTERACTION

PTR/PTREF

- 1 0.9900
- 2 0.9800
- 3 0.9600
- 4 0.9400
- 5 0.9200
- 6 0.9000
- 7 0.8600
- 8 0.8200
- 9 0.7800
- 0 0.7400

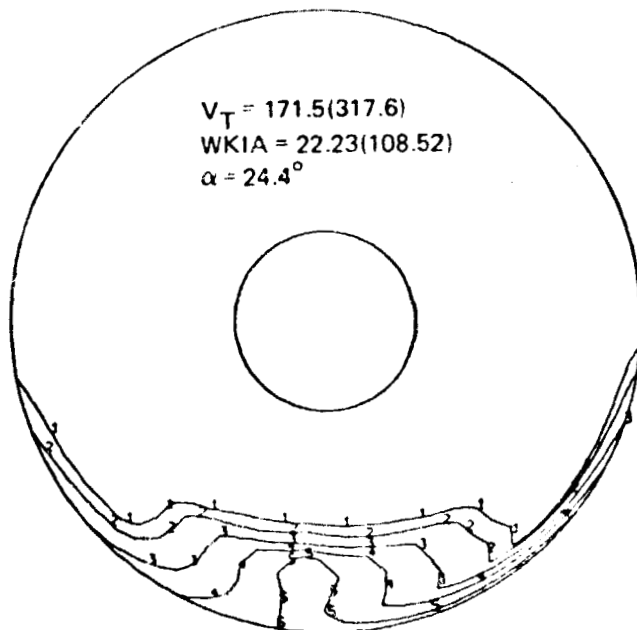
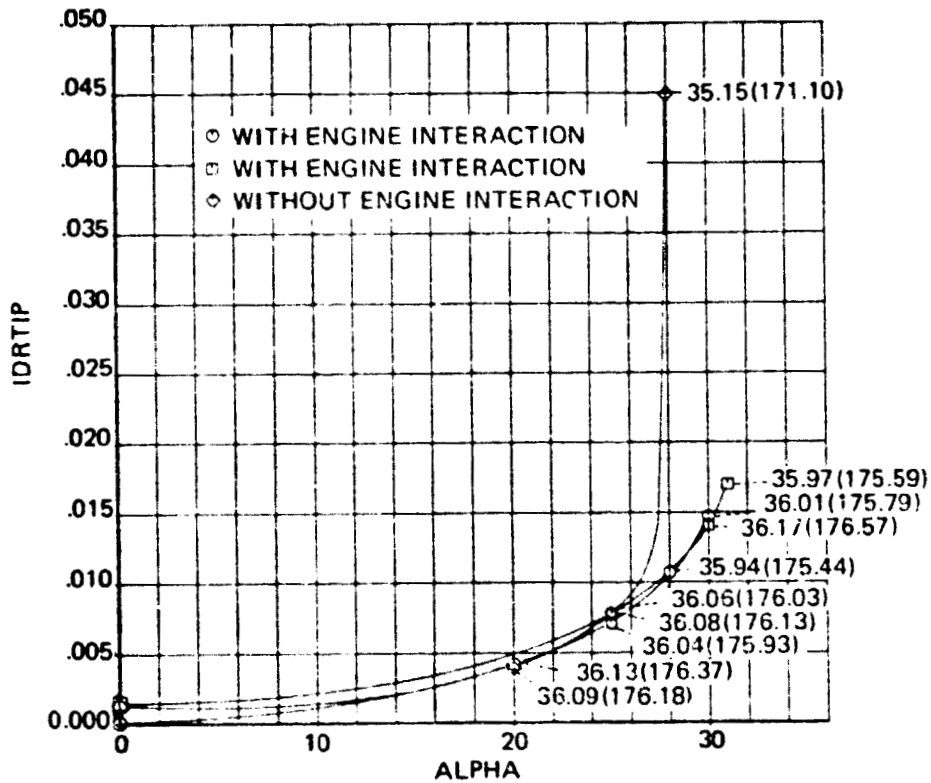
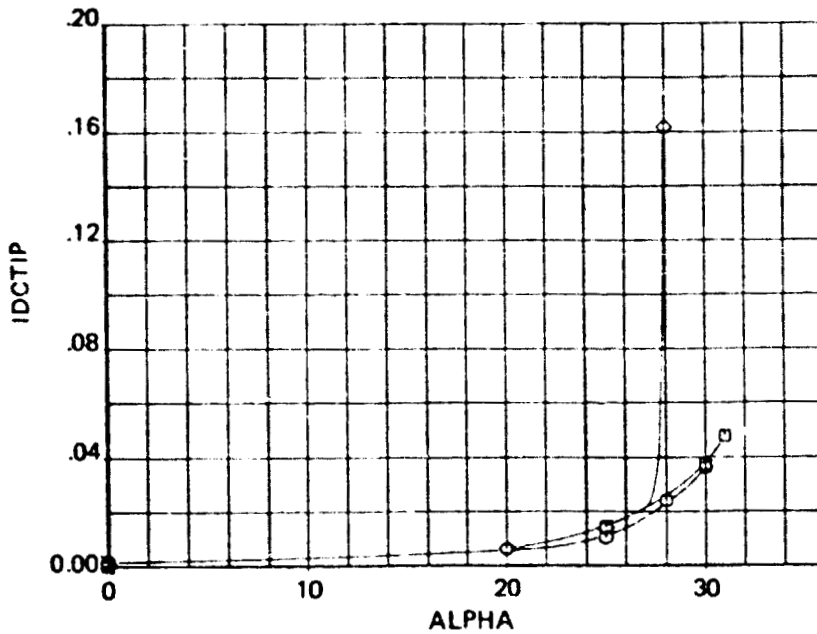


Figure 53.—Comparison of Fan Face Total Pressure Recovery Maps With and Without Engine Interaction

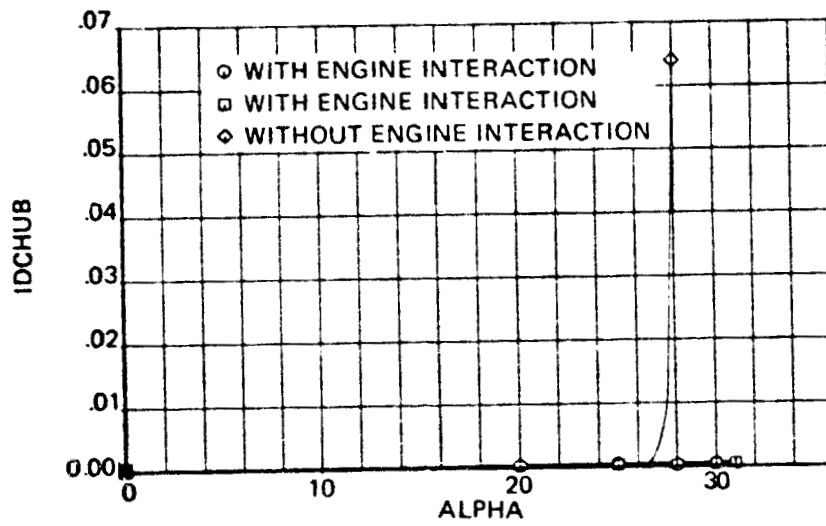


(a) INLET TIP RADIAL DISTORTION



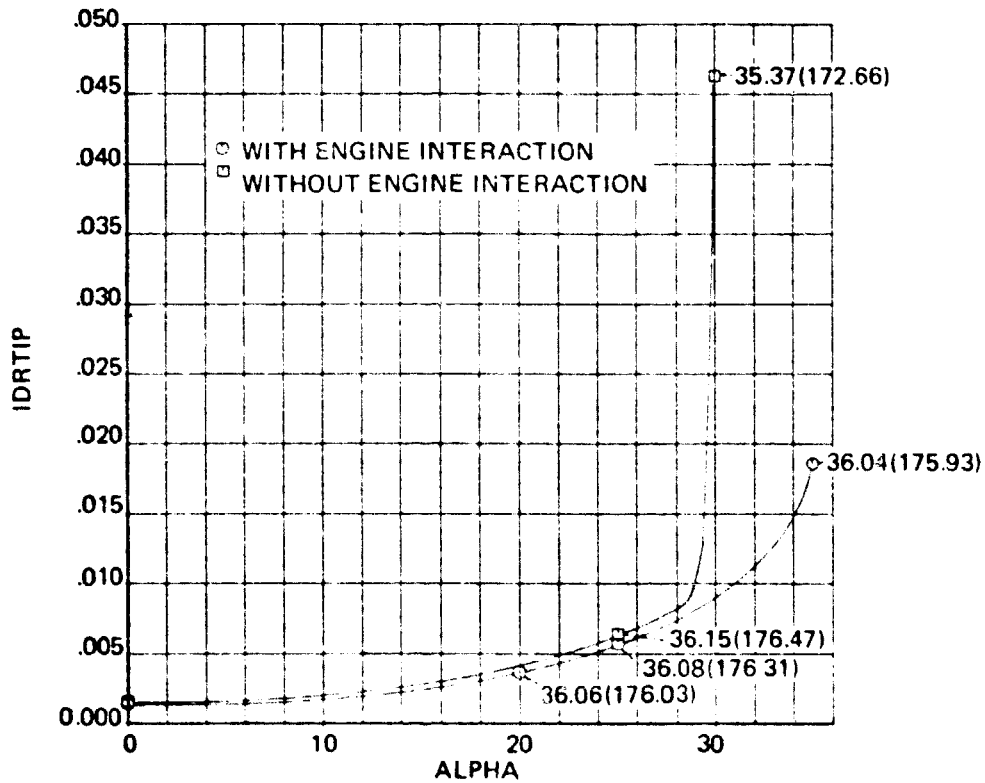
(b) INLET TIP CIRCUMFERENTIAL DISTORTION

Figure 54.—Variation of Inlet Distortion With Inlet Angle-of-Attack; With and Without Engine Interaction, $V_T = 171.6(317.8)$, $WKIA = 36.07(176.06)$

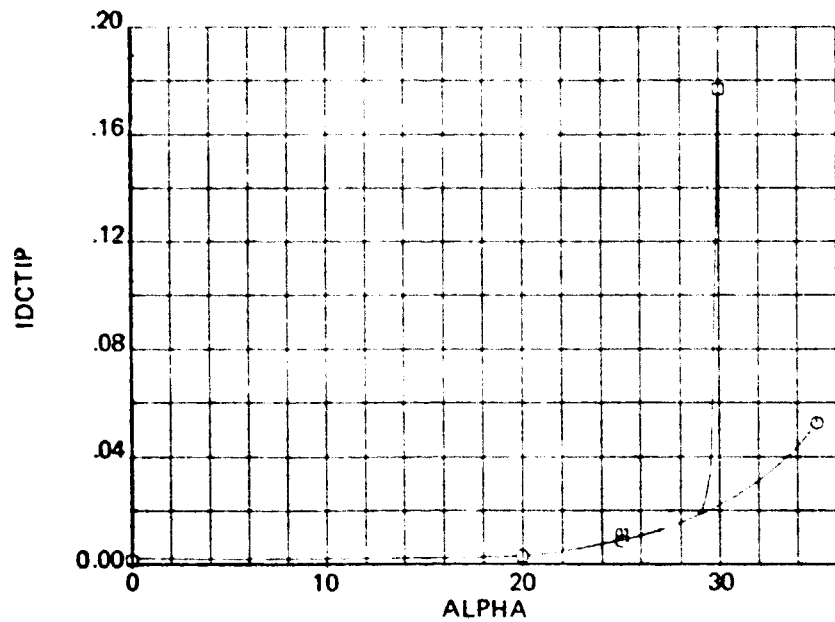


(c) INLET HUB CIRCUMFERENTIAL DISTORTION

Figure 5-1.-(Concluded)

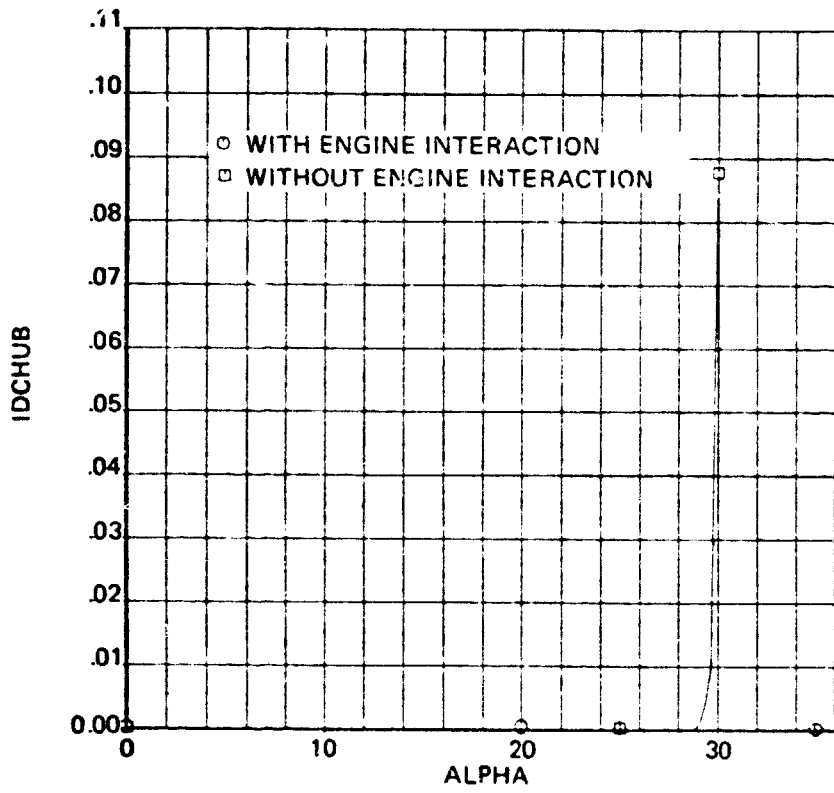


(a) INLET TIP RADIAL DISTORTION



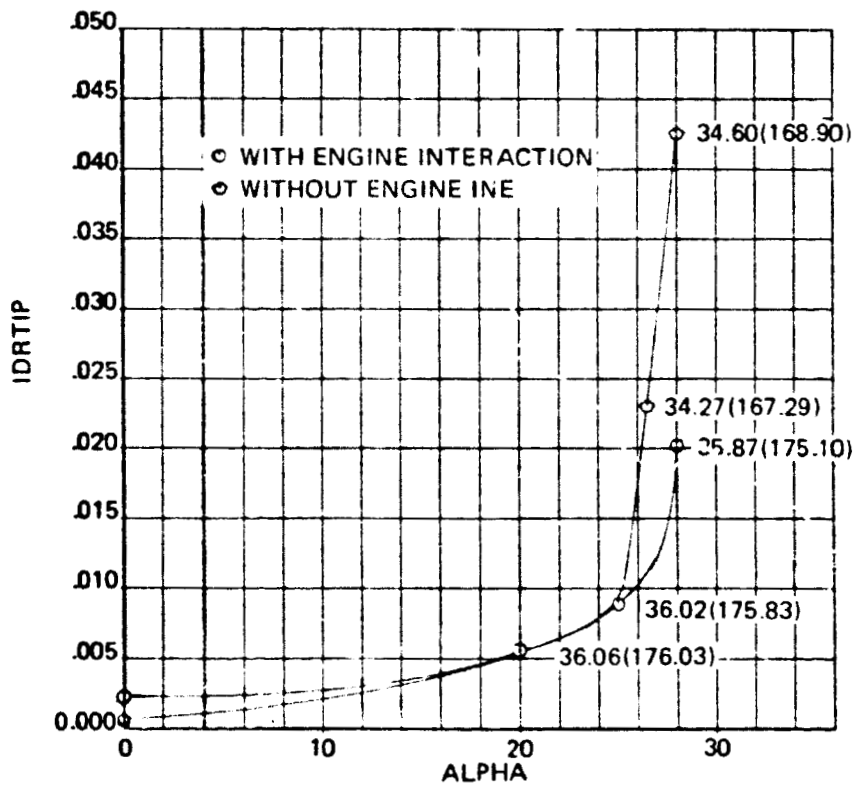
(b) INLET TIP CIRCUMFERENTIAL DISTORTION

Figure 55.—Variation of Inlet Distortion With Inlet Angle-of-Attack; With and Without Engine Interaction, $V_T = 147.6(273.4)$, $WKIA = 36.06(176.05)$

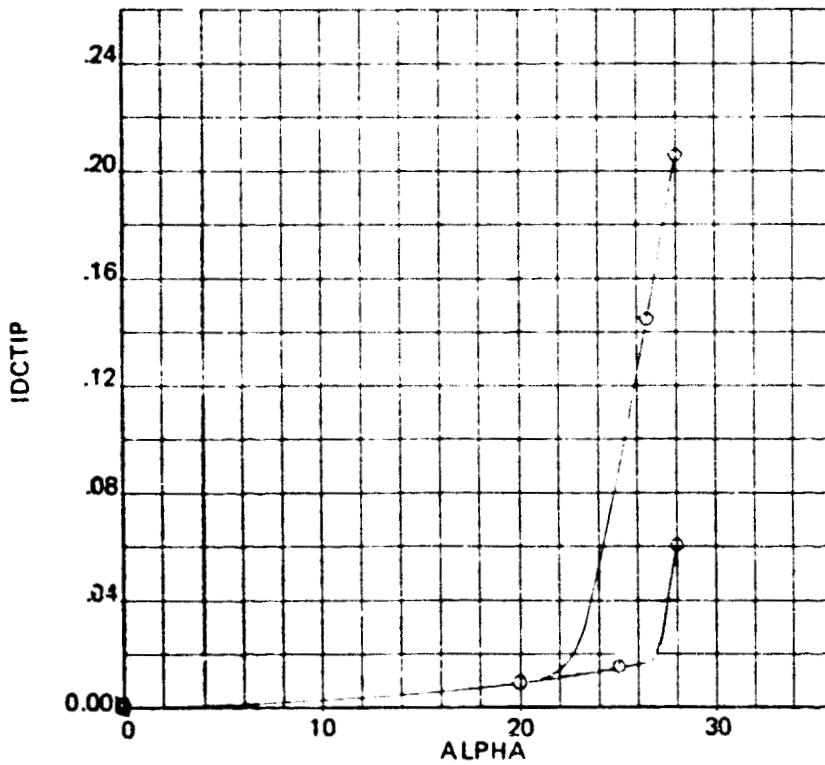


(c) INLET HUB CIRCUMFERENTIAL DISTORTION

Figure 55. --(Concluded)

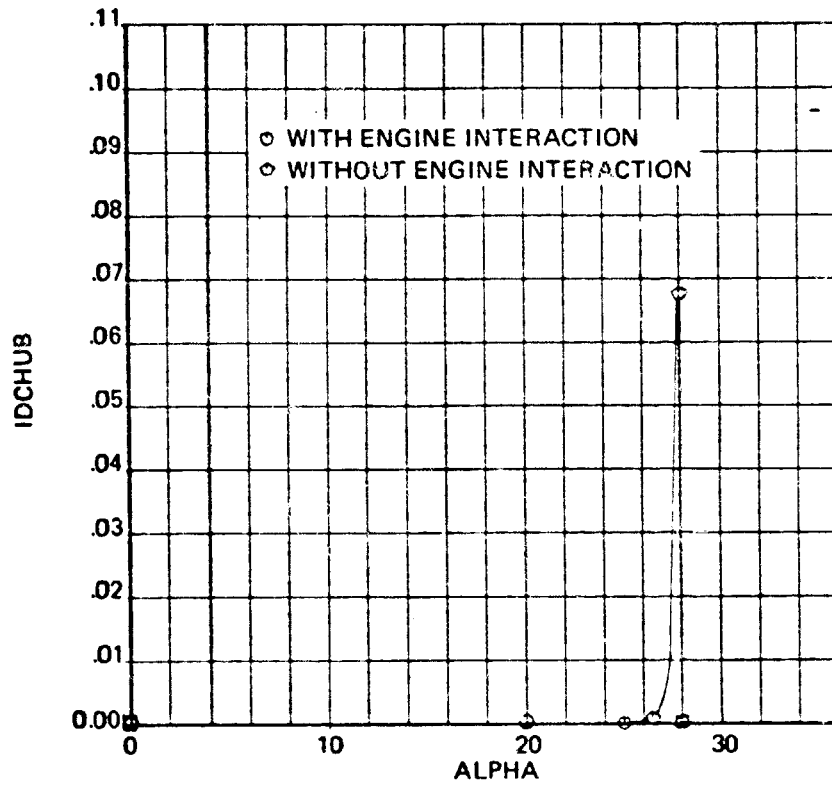


(a) INLET TIP RADIAL DISTORTION



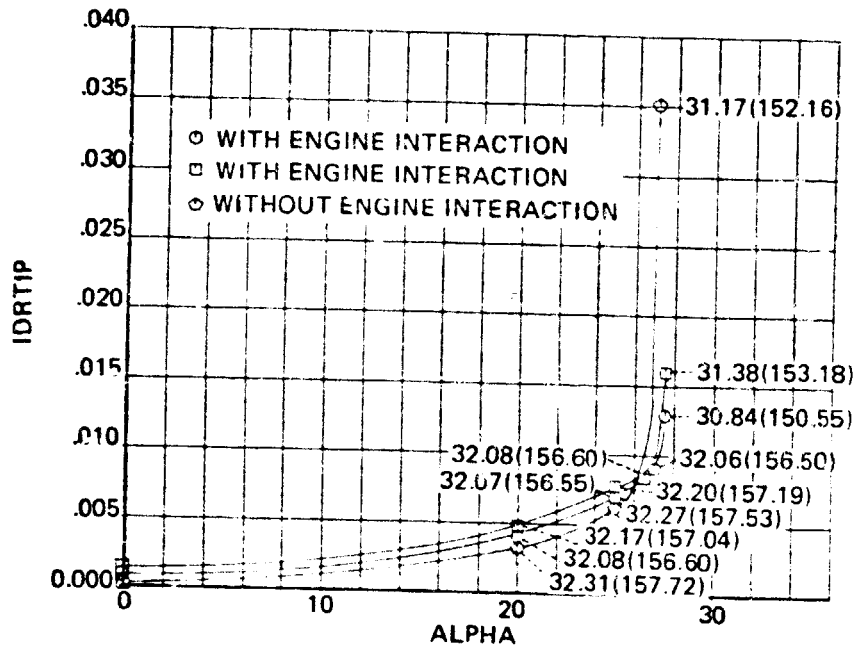
(b) INLET TIP CIRCUMFERENTIAL DISTORTION

Figure 56.—Variation of Inlet Distortion With Inlet Angle-of-Attack; With and Without Engine Interaction, $V_T = 186.8(346.0)$, $W_{KIA} = 36.04(175.93)$

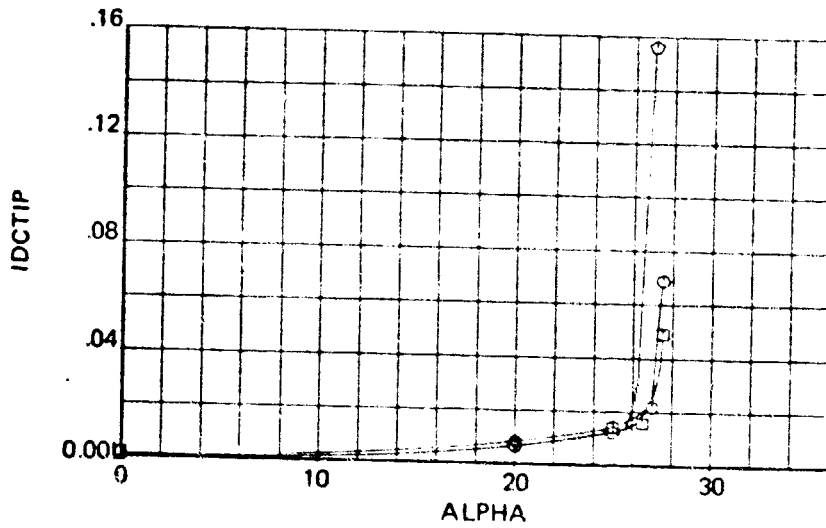


(c) INLET HUB CIRCUMFERENTIAL DISTORTION

Figure 56.—(Concluded)

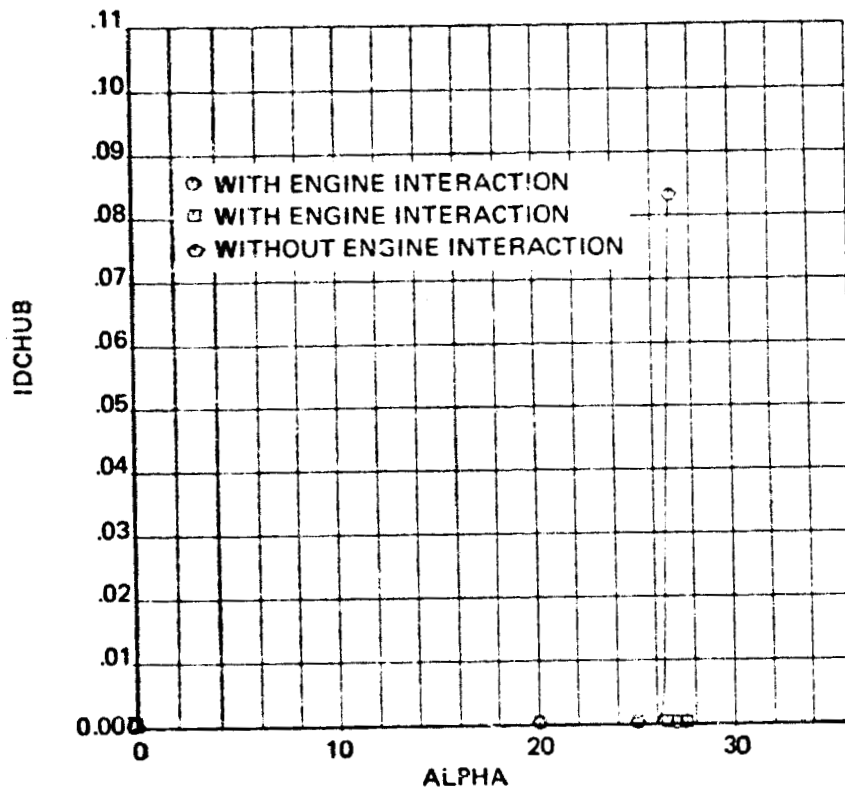


(a) INLET TIP RADIAL DISTORTION



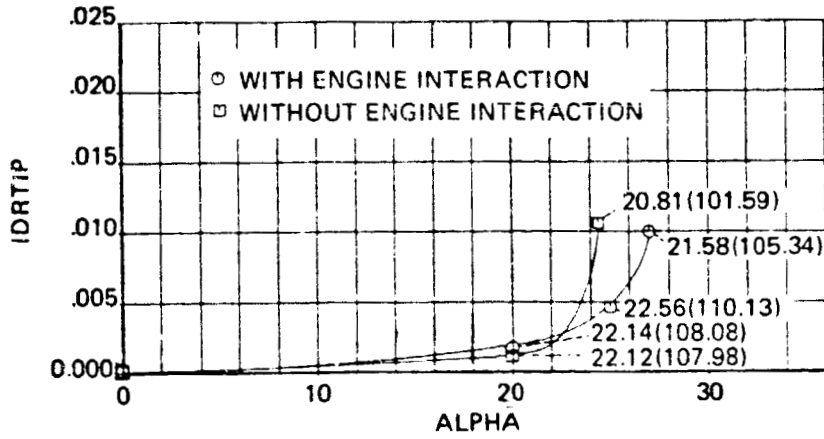
(b) INLET TIP CIRCUMFERENTIAL DISTORTION

Figure 57.—Variation of Inlet Distortion With Inlet Angle-of-Attack; With and Without Engine Interaction, $V_T = 186.2(344.9)$, $WKIA = 32.16(156.99)$

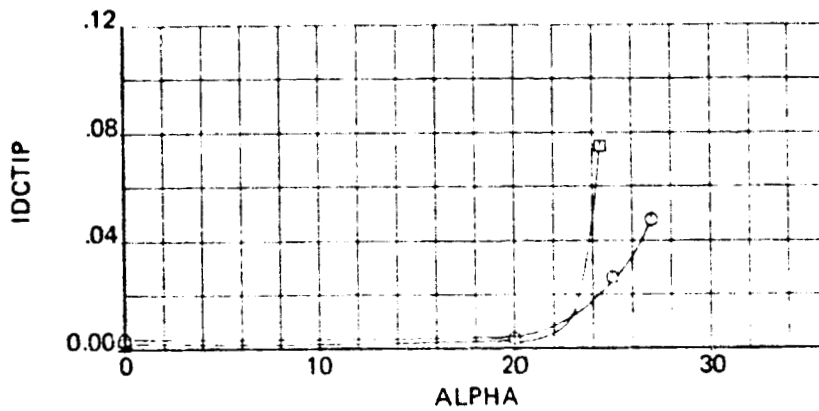


(c) INLET HUB CIRCUMFERENTIAL DISTORTION

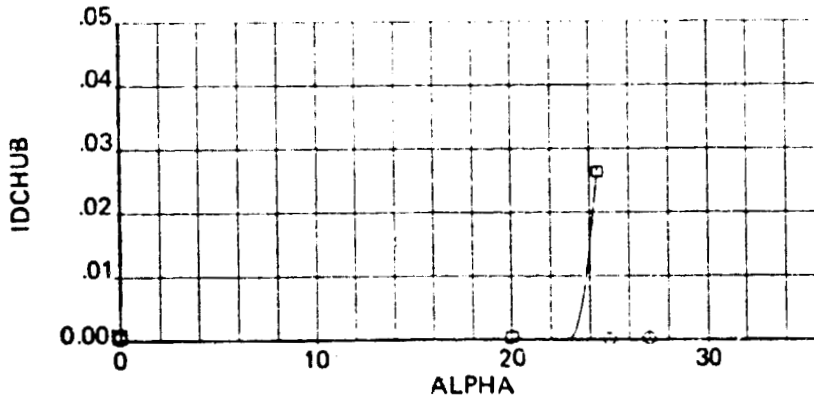
Figure 57.—(Concluded)



(a) INLET TIP RADIAL DISTORTION



(b) INLET TIP CIRCUMFERENTIAL DISTORTION



(c) INLET HUB CIRCUMFERENTIAL DISTORTION

Figure 58.—Variation of Inlet Distortion With Inlet Angle-of-Attack; With and Without Engine Interaction, $V_T = 171.5(317.6)$, $WKIA = 22.25(108.59)$